NASA CR-165332

INERT GAS THRUSTERS

Prepared for

LEWIS RESEARCH CENTER

NATIONAL AERONAUTICS AND SPACE ADMINISTRATION

GRANT NSG 3011

Annual Report

December 1980

Harold R. Kaufman and Raymond S. Robinson
Department of Mechanical Engineering
Colorado State University
Fort Collins, Colorado

1. Report No.	2. Government Accession No.	3. Recipient's Catalog No.
CR-165332		

4. Title and Subtitle	5. Report Date
INERT GAS THRUSTERS (U)	December 1980
	6. Performing Organization Code

7. Author(s)	8. Performing Organization Report No.
Harold R. Kaufman and Raymond S. Robinson	
	10. Work Unit No.

9. Performing Organization Name and Address	11. Contract or Grant No.
Department of Mechanical Engineering Colorado State University Fort Collins, Colorado 80523	NSG 3011
	13. Type of Report and Period Covered

12. Sponsoring Agency Name and Address	13. Type of Report and Period Covered
National Aeronautics and Space Administration Washington, DC 20546	Contract Report
	14. Sponsoring Agency Code

15. Supplementary Notes

Grant Manager: William R. Kerslake
NASA Lewis Research Center
Cleveland, Ohio 44135

16. Abstract

Some recent advances is component technology for inert-gas thrusters are described. The maximum electron emission of a hollow cathode with Ar can be increased 60-70% by the use of an enclosed keeper configuration. Operation with Ar, but without emissive oxide, has also been obtained. A 30-cm thruster operated with Ar at moderate discharge voltages gave double-ion measurements consistent with a double-ion correlation developed previously using 15-cm thruster data. An attempt was made to reduce discharge losses by biasing anodes positive of the discharge plasma. The reason this attempt was unsuccessful is not yet clear. The performance of a single-grid ion-optics configuration was evaluated. The ion impingement on the single-grid accelerator was found to approach the value expected from the projected blockage when the sheath thickness next to the accelerator was 2-3 times the aperture diameter.

17. Key Words (Suggested by Author(s))	18. Distribution Statement
Electric Propulsion Ion Beams Ion Sources Plasma Physics	Unclassified - Unlimited

19. Security Classif. (of this report)	20. Security Classif. (of this page)	21. No. of Pages	22. Price*
Unclassified	Unclassified		

* For sale by the National Technical Information Service, Springfield, Virginia 22161

N81-26177#

TABLE OF CONTENTS

I. INTRODUCTION

A continued research program has been directed at both component and overall performance of inert-gas thrusters.[1-5] Progress is reported herein for component research in cathodes, discharge chambers, and ion optics.

A maximum electron emission has been observed for a given combination of cathode configuration and inert-gas flow. Preliminary tests have previously shown that higher maximum emissions can be reached at the same gas flow using an enclosed keeper design. Reported herein are the results of an experimental study of different enclosed-keeper configurations, with the study directed at increasing the maximum emission.

The "conventional" hollow cathode configuration has a tungsten tip welded to a tantalum tube, together with an oxide impregnated insert. When projected to larger sizes, thermal stresses at the welded joint could easily cause reliability problems. Also, there have been various problems associated with the presence of the oxide that is provided to enhance electron emission. A research effort has therefore been directed towards new hollow-cathode concepts. Among the more promising concepts, described herein, is a carbon cathode tip held in place with spring tension. No emissive oxide is used with the carbon-tip design and heat is provided by an internal glow discharge.

Doubly charged ions are responsible for most of the erosion within a discharge chamber. To provide design information for future large thrusters, double ion data were obtained with a 30-cm multipole thruster.

Another area of discharge-chamber research concerned the possible reflection of ions at the discharge-chamber boundary. If such reflection

were possible, it could result in reduced discharge losses. To this end, an experiment was conducted with various anode biases.

The final research described herein is the study of single-grid ion optics. The usual two-grid or three-grid ion optics become increasingly limited in current capacity as specific impulse is lowered. Single-grid ion optics are limited by sputtering erosion to low ion energies, but avoid the ion-beam current limitations of multiple-grid ion optics. The operating characteristics of a single-grid ion-optics configuration were measured to facilitate evaluation of this ion-optics approach at, for electrostatic propulsion, relatively low specific impulses.

A shorter version of this report is published as an AIAA paper.* The major differences are in the appendices included herein.

---

*Harold R. Kaufman, Raymond S. Robinson, and Donald C. Trock, "Inert-Gas Thruster Technology," AIAA Paper No. 81-0721, April 1981.

II. HOLLOW CATHODES

Enclosed-Keeper Designs

There is a maximum electron emission that can be obtained with a given combination of hollow-cathode configuration and inert-gas flow rate. The limiting condition is a rapid increase in anode voltage when an attempt is made to increase the anode current. No similar limitation has been reported for mercury hollow cathodes. If such a limitation exists with mercury, it probably exists beyond normal operating ranges.

This emission maximum is an important consideration for inert-gas thruster design. For example, using tests in a small vacuum chamber as a basis for estimating performance, the reference design utilizing an open keeper described herein would require 0.6 A-equiv of argon to neutralize a 10 A ion beam with a 26% safety margin between normal operation and the emission limit. This means that a factor of about 0.95 would be introduced into the overall thruster efficiency due to just the neutral loss from the neutralizer. If a greater safety margin were used, the reduction in overall efficiency would be greater. A similar calculation for the discharge chamber shows that most of the neutral flow to the discharge chamber would have to be directed through the discharge-chamber cathode, or cathodes. Such a cathode flow could easily result in significant propellant density nonuniformities in the discharge chamber for the short length-to-diameter ratios expected in future large thrusters. Means of increasing the maximum emission for a given gas flow are therefore of interest for future inert-gas thrusters.

Preliminary tests have shown higher electron emissions are possible for the same inert-gas flow using an enclosed keeper design.[5] As a result of these preliminary tests, an extensive study has been conducted

to determine the optimum enclosed-keeper configuration. The enclosed-keeper design tested, together with the open-keeper reference design with which it was compared, is shown in Fig. 1. The reference design, shown in Fig. 1(a), had a wire keeper with an inside diameter of 4 mm, spaced 1 mm from the cathode tip. The enclosed-keeper design, Fig. 1(b), was operated with a range of keeper hole diameters from 2 to 6 mm, in 1 mm increments. The keeper spacing from the tip was varied from 1 to 9 mm, also in 1 mm increments. The hollow-cathode orifice was 0.76 mm for both cathode designs. The anode used in all tests was a perforated cylinder 5 cm in diameter and 7.6 cm long, with the cathode mounted on axis near one end. Past tests have shown that a large anode area, such as this, is necessary when using argon to avoid an increased anode voltage due to the anode sheath. Detailed results for the enclosed keeper tests are given in Appendix A.

Some sample performance curves are shown in Figs. 2 and 3, all for a 4 mm keeper hole diameter. Note that a sharp rise in anode voltage was encountered for all test configurations - if the emission current was increased to a high enough value. As described in earlier work, operation within this region of sharp voltage rise is associated with a large increase in electrical "noise" and plume luminosity.[5]

The optimum enclosed keeper position is shown in Fig. 4 for each hole diameter investigated. The points shown indicate the position of the aperture in the keeper. The optimum in this case was defined as the spacing that gave the highest ratio of electron emission to gas flow (A/A-equiv) at an anode potential of 30 V. Where more than one keeper spacing is shown for the same hole diameter, no significant difference was found for the spacings shown.

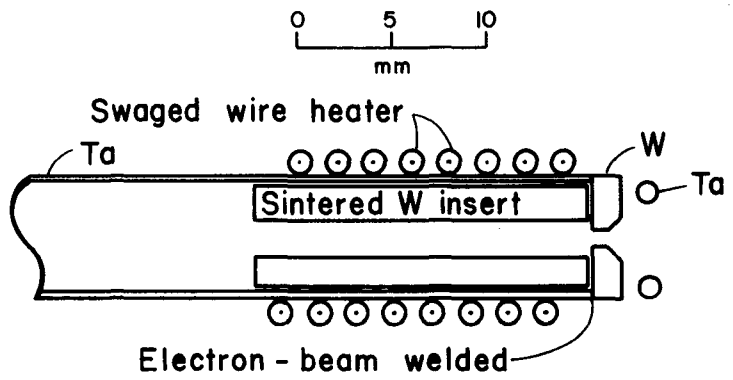

(a) Open keeper design

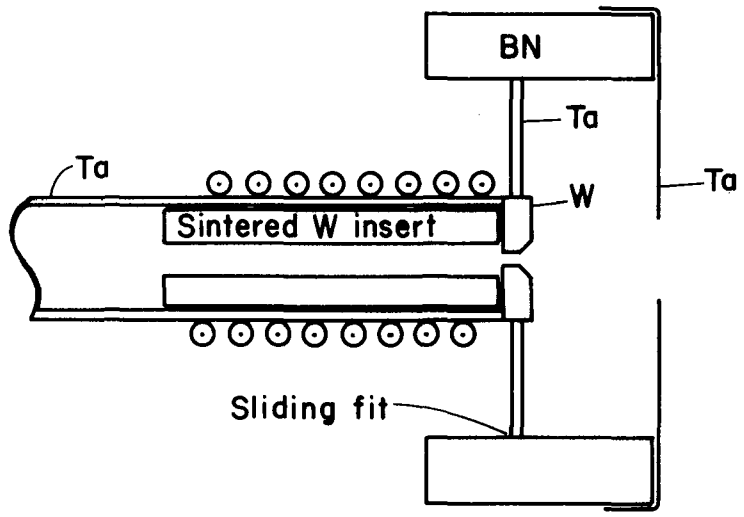

(b) Enclosed keeper design

Fig. 1. Hollow cathode configurations with oxide impregnated inserts. (Barium and strontium carbonates are used for the impregnation. Oxides are produced during heating prior to operation.)

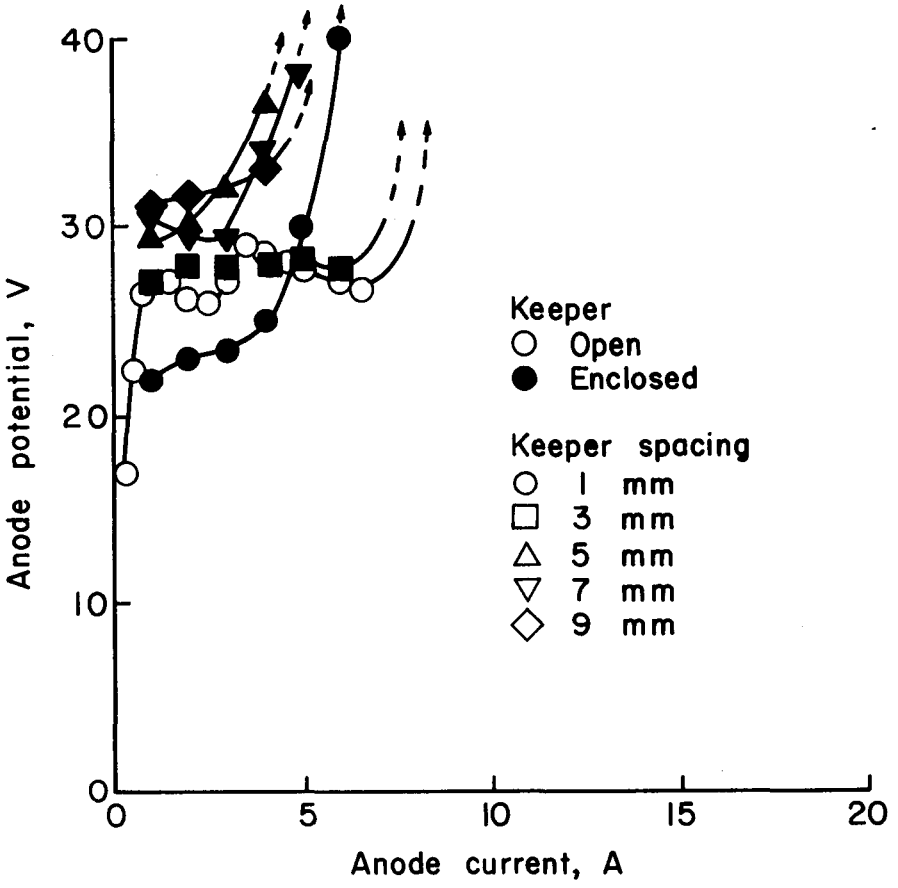

Fig. 2. Comparison of performance with open and enclosed keepers. Argon flow, 0.4 A-equiv; keeper current, 0.3 A; keeper hole diameter, 4 mm.

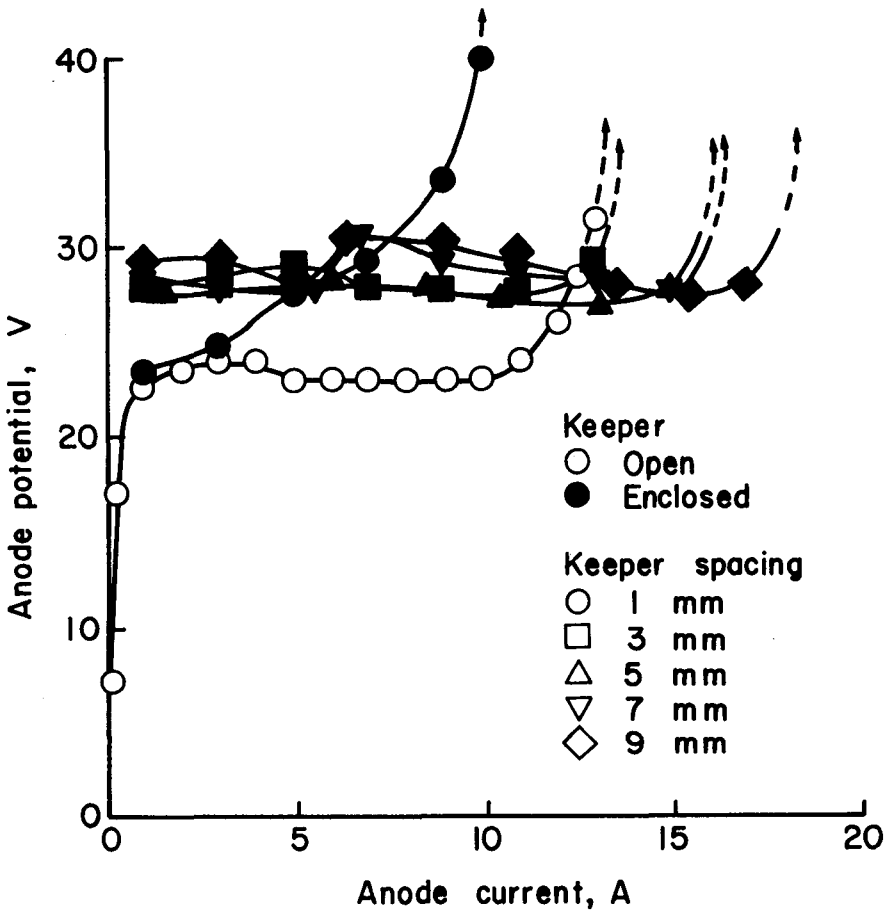

Fig. 3. Comparison of performance with open and enclosed keepers. Argon flow, 0.6 A-equiv; keeper current, 0.3 A; keeper hole diameter, 4 mm.

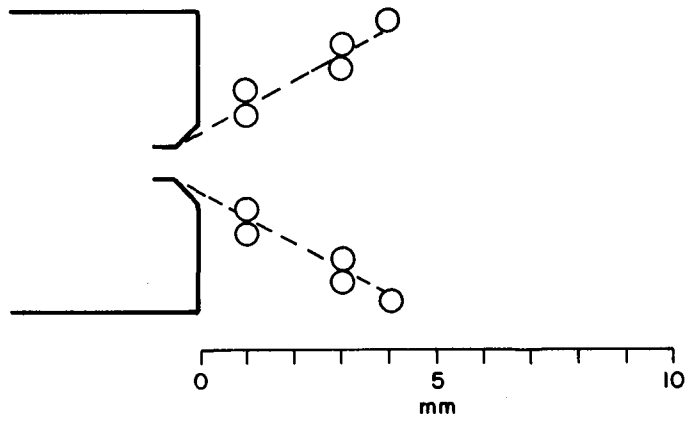

(a) Argon flow, 0.4 A-equiv

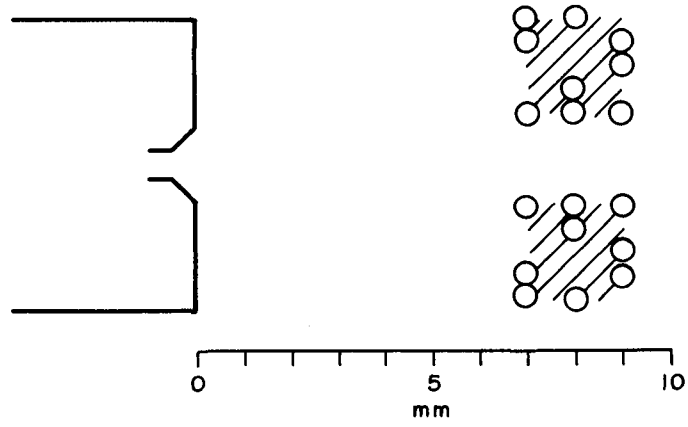

(b) Argon flow, 0.6 A-equiv

Fig. 4. Optimum enclosed keeper spacings for a range of keeper opening diameter. (Optimized for maximum emission at an anode potential of 30 V.)

The mean free path within the keeper enclosure was calculated assuming an enclosure temperature of 400°C and a neutral cross section of 26 $\mathring{A}$.[2] For the 0.4 A-equiv flow rate, the calculated mean free path was in all cases larger than the keeper spacings shown in Fig. 4(a). This calculated result is consistent with the optimum keeper locations of Fig. 4(a), which roughly define a cone with a 30° half angle. The electron current from a hollow cathode is known to roughly follow the path of the neutral efflux from the orifice. For the 0.4 A-equiv flow of Fig. 4(a), the distribution of the neutral efflux appears to be determined close to the orifice, with little effect due to the pressure within the keeper enclosure. The best keeper locations in this case resemble those found for open-keeper designs. That is, they do not intrude on the central current carrying region which occupies a large-angle conical volume.[6]

For the 0.6 A-equiv argon flow rate, the calculated mean free paths in all cases were smaller than the optimum keeper spacings of Fig. 4(b). This result is consistent with these locations forming much smaller angles relative to the beam axis and the orifice. That is, the higher enclosure pressures at the 0.6 A-equiv flow rate result in a closer approach to continuum flow, so that the efflux is actually confined to a smaller region due to the pressure within the enclosed keeper. This interpretation is qualitatively consistent with effective enclosed-keeper designs developed for mercury.[6]

At 0.4 A-equiv of argon, the reference open-keeper design had a maximum emission-to-flow ratio of 16 A/A-equiv. For the keeper locations shown in Fig. 4(a), the same ratio ranged from 15-28 A/A-equiv, with the highest ratio obtained at the highest spacing.

At 0.6 A-equiv, the reference open-keeper design had a ratio of 21 A/A-equiv. For the keeper locations shown in Fig. 4(b), the ratios were 23-33 A/A-equiv, with the lowest ratio obtained using the 2 mm hole and the highest with the 6 mm hole.

The best enclosed keeper designs thus gave 60-70% increases in emission over the reference open-keeper design at the same gas flow rate. For the orifice size used (0.76 mm), good performance should not be expected much below 0.4 A-equiv of argon. At 0.3 A-equiv, an emission-flow ratio of 17 was obtained, but there was an intermediate region of erratic operation that exceeded 30 V. Assuming a design with adequate heat rejection, satisfactory operation should be expected at higher gas flows. At 0.7 A-equiv, the emission-flow ratio was 28, or more,* with the open keeper reference design. Extrapolation of these trends would indicate that an open-keeper design may be adequate, if emissions and flow rates are high enough. If an enclosed keeper design is used at higher flow rates, the optimum designs would be expected to be more similar to Fig. 4(b) than Fig. 4(a).

Some experiments were also conducted with various shapes for the keeper enclosure, but without any significant effect on the performance. As an example of these experiments, data for a tubular keeper, 5 mm in diameter and 7 mm long, are shown in Fig. 5. Also shown in Fig. 5 are data for flat plate keepers (of the type shown in Fig. 1(b)) with a spacing of 7 mm and diameters of 3 and 4 mm. The flat plate keeper holes selected were smaller than the tubular hole to approximate the same gas-flow impedance. As can be seen, the anode characteristics were

---

*The power supply limit was reached before a sharp anode voltage rise was encountered. The exact minimum ratio is therefore not known.

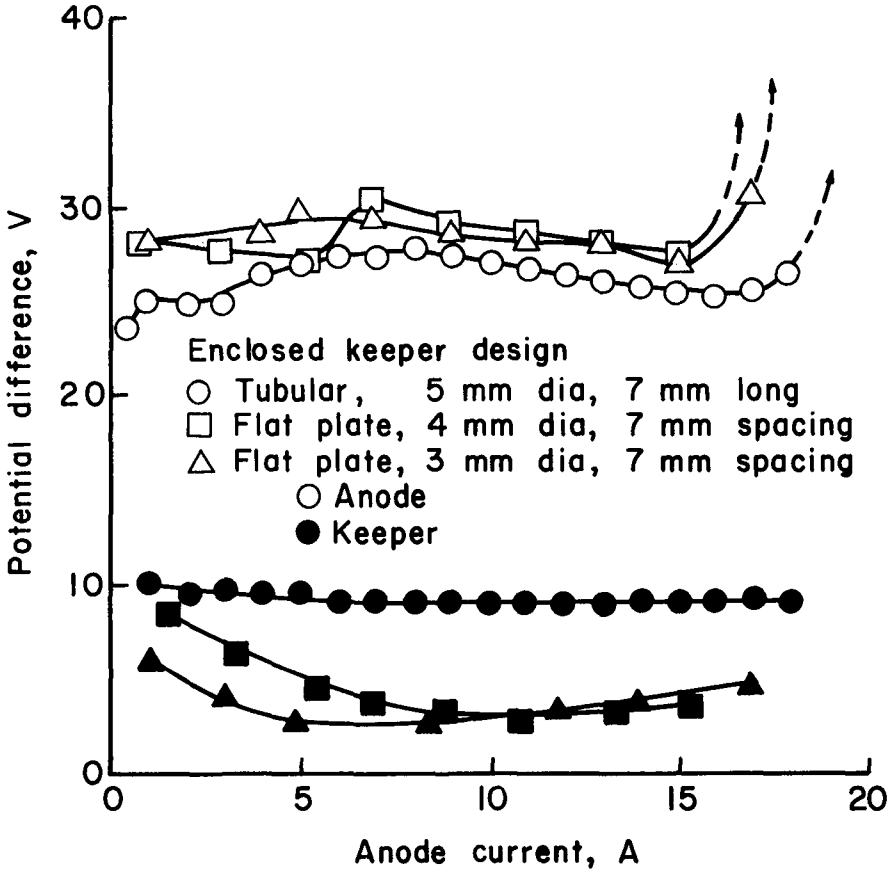

Fig. 5. Comparison of performance with different enclosed keeper designs. Argon flow, 0.6 A-equiv; keeper current, 0.3 A.

quite similar for the two keeper configurations. The keeper voltage for the tubular keeper design was slightly higher, perhaps because the larger 5 mm diameter had a higher impedance connection to the current carrying region near the axis.

Carbon-Tip Designs

There appears to be a clear need for large inert-gas thrusters in the future, which implies a similar need for large cathodes. The present hollow-cathode design, with a tungsten tip electron-beam welded to a tantalum tube, is expensive and difficult to fabricate. Also the possibility of thermal stress and fatigue problems at the welded joint would be increased with increased cathode size and power.

An alternate approach was considered as a means of avoiding most of the thermal stress problems. In this alternate approach the tip is a separate part, kept in contact with the cathode tube by spring tension. With such a design, relative expansion of the tip and tube can take place without significant stress. Also, with no welding required, the choice of tip material can be made without consideration of welding compatibility. Carbon (graphite) then becomes a good candidate, with excellent high-tenperature capability and ease of machining.

The carbon-tip design shown in Fig. 6(a) was first tested with an oxide impregnated insert. Five hours of operation resulted in noticeable material removal from the upstream edge of the orifice, apparently by some flaking process rather than sputter erosion. The glow discharge heating concept also shown in Fig. 6(a) was first tested with a conventional tungsten tip, which reached temperatures in excess of 2000°C during operation. The high temperature encountered without oxide made the combination with a carbon tip appear attractive. The two concepts

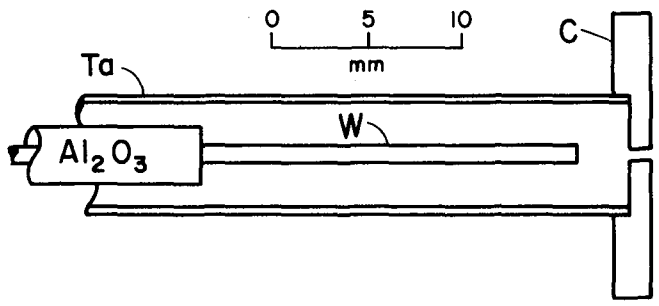

(a) With large tip

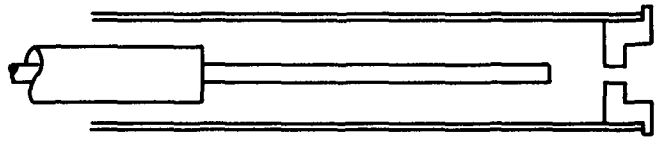

(b) With small tip

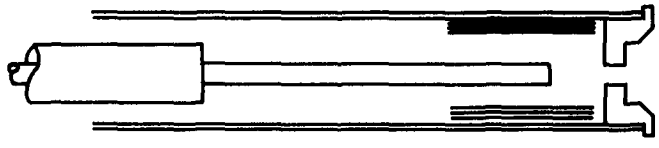

(c) With small tip and Ta foil insert

Fig. 6. Carbon-tip hollow-cathode configurations investigated. Keeper (not shown) was 4 mm inside diameter wire ring 1 mm from tip. Orifice diameter, 0.71 mm.

were combined, as indicated in Fig. 6(a), which resulted in a configuration that never achieved coupling to the anode. Although the tantalum tube was heated to a yellow-white heat by the glow discharge within, no significant electron current was ever established to the anode.

To reduce the cooling influence of the large carbon tip, it was reduced in size, as indicated in Fig. 6(b). After about 15 seconds with a 1.2 A heating discharge between the central tungsten electrode and the tantalum tube, with 0.8 A-equiv of argon flowing, the tip reached 1500°C and a discharge was established to the anode. Up to this point the keeper had been at 500 V to assist coupling through the orifice. The heater and keeper power supplies were then both turned off, and the heating was provided by the cathode-anode current. The operating characteristics for this configuration are shown in Fig. 7. The 4 A point represents the lowest anode current for which the cathode was self-heating. The tip temperatures ranged from about 1500°C at 4 A to 1700°C at 15 A. Disassembly after several hours of running revealed some surface texturing, but no significant dimensional changes.

A working hypothesis was made at this point. Assuming the required emission temperature* is achievable, the potential difference between the cathode and the plasma within it varies to maintain a surface at emitting temperature. For an oxide coated or impregnated insert, the heating power can be quite low. Without oxide, a much higher power must be supplied to reach emission temperature. Comparing the performance of a conventional hollow cathode that uses oxide[5] with the configuration

---

*The actual emission within a hollow cathode is believed to be by a combination of thermionic and high-field processes. In this discussion we are concerned primarily with the effects of temperature.

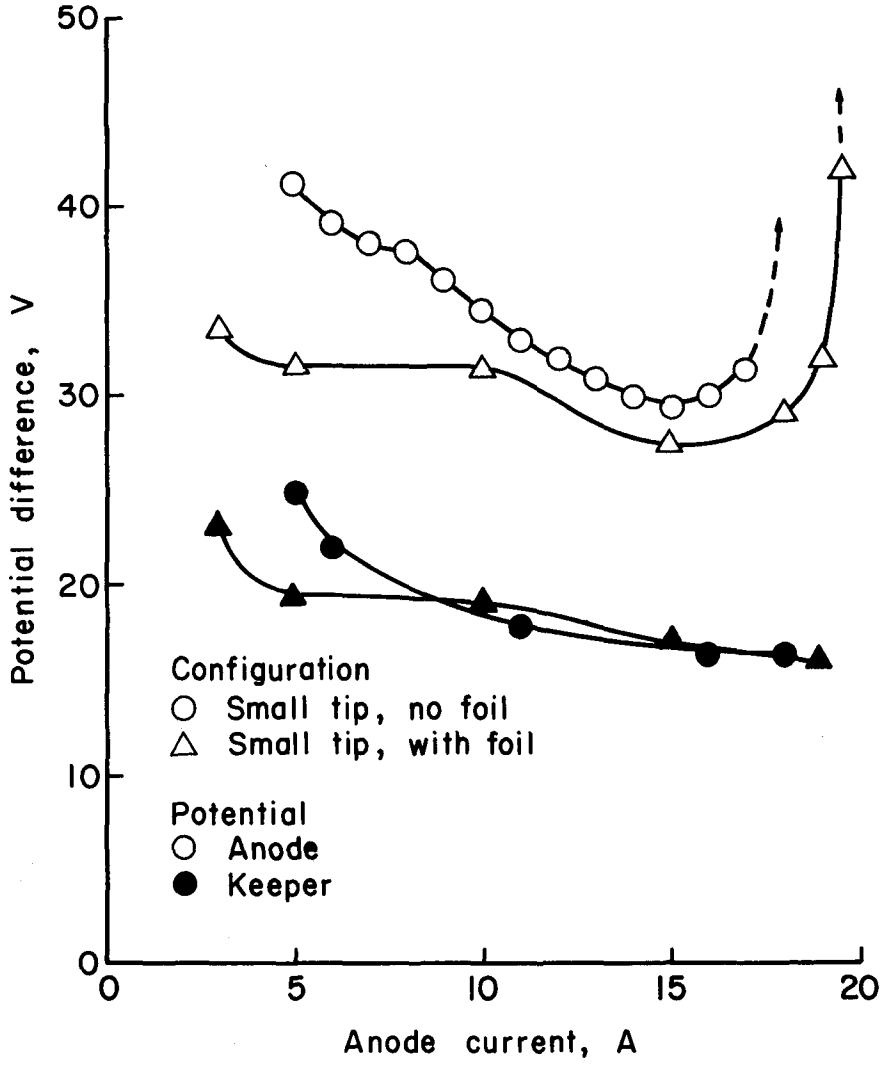

Fig. 7. Hollow-cathode performance with carbon (graphite) tip configurations. Argon flow, 0.8 A-equiv; keeper current, 0.3 A.

shown in Fig. 6(b), the difference in anode voltage at similar currents indicates an additional 100-120 W of heating power is required in the absence of oxide.

From the above reasoning, an attempt was made to reduce the anode voltage required by providing better thermal isolation between the emitting surface and the outside of the cathode. The emitting surface and the thermal isolation consisted of three layers of tantalum foil inside the tantalum tube. This configuration was first tested without the tip bevel also included in Fig. 6(c). The major effect of the tip bevel (compare tips for Figs. 6(b) and (c)) was to increase the maximum anode current by about 2 A. Data for the configuration as shown in Fig. 6(c) are also shown in Fig. 7. Comparing the data for the two configurations in Fig. 7, the addition of the tantalum foil reduced the heating power requirements by 30-50 W.

An even more impressive result of the tantalum foil addition was the ease of starting. Starting at room temperature with a 1.1 A-equiv argon flow and 65 V on the anode (no keeper), the 1.2 A internal discharge would heat the cathode to emission temperature and permit coupling to the anode within five seconds. The heater power could then be turned off, the flow reduced to 0.7 A-equiv, and normal operation maintained over a 3-20 A emission range. The tip temperature for this configuration ranged from a little over 1200°C at 3 A to over 1800°C at 19 A. Disassembly after several hours of operation revealed no measurable erosion.

The results presented for carbon-tip hollow cathodes, without oxide enhanced emissive surfaces, are believed to be significant. These results suggest that the present electron-beam welded construction can be replaced with a more economical assembled construction. Also, it is

possible that oxides with their attendant problems of conditioning, poisoning, and depletion might be eliminated. Some additional heating power (and hence coupling voltage) will probably be required in the absence of oxide, but with proper thermal design this increase should be small. Note that the glow-discharge heater is inherently simpler than the swaged-wire heater that it replaces, indicating the possibility of increased heater reliability.

III. DOUBLY IONIZED PROPELLANT

The erosion within the discharge chamber of a thruster is due mostly to doubly charged ions. This erosion has become more serious as thrusters have become larger, and two-step double ionization from primary electrons has become the dominant process at normal operating conditions.* With even larger thrusters planned for the future, the prediction and control of doubly ionized propellant has become an important research area.

A theory for the production of doubly charged ions has existed for some time,[7-8] but the utility of this theory has been limited by the prior need for detailed plasma probe data. A more recent approach assumes that the two-step process from primary electrons is the dominant one for generating doubly charged ions.[9] With this assumption, parameters were derived to use in the correlation of experimental double ion data, without any requirement for detailed plasma properties. The correlation of experimental data obtained was also in qualitative agreement with a straight theoretical derivation using the same two-step assumption.

The experimental data used in the correlation described above was obtained with a 15-cm multipole thruster. With much larger thrusters planned for the future, it is of interest how well the data from larger thrusters would agree with the correlation. Double ion data were therefore obtained from a 30-cm multipole thruster. These 30-cm data are plotted in Fig. 8, together with the previously obtained 15-cm data.

---

*A one-step process is involved when a neutral becomes a doubly charged ion with a single electron collision. A two-step process requires two electron collisions for a doubly charged ion to be generated from a neutral, with a singly charged ion the usual intermediate step.

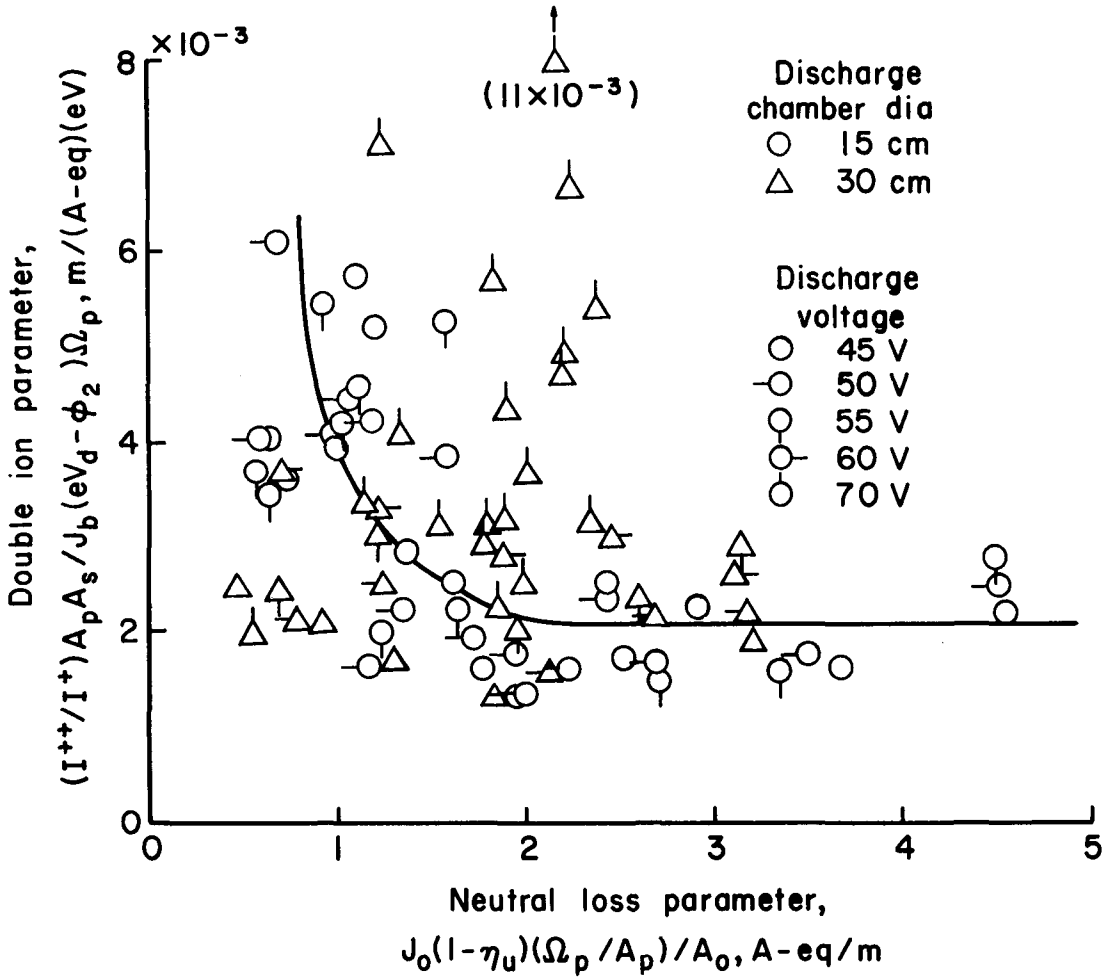

Fig. 8. Double ion correlation for argon. Double ion parameter based only on two-step double ionization from primary electrons.

The curve in Fig. 8 is the one used previously to fit just the 15-cm data. In the neutral-loss parameter, J_o is the total neutral flow rate to the discharge chamber in A-equiv, η_u is the fraction of this total flow that is ionized when it leaves the discharge chamber, Ω_p and A_p are the volume and outside area of the primary electron region in m^3 and m^2, and A_o is the effective sharp-edged orifice area for the escape of neutrals through the ion optics. In the double-ion parameter, in addition to some of the above quantities, I^{++}/I^{+} is the ratio of doubly to single ionized ion currents, A_s is the open screen area for extracting ions in m^2, J_b is the ion beam current in A, eV_d is the primary electron energy in eV (electronic charge times discharge voltage), and ϕ_2 is the second ionization potential in eV.

At first glance, the 30-cm data departs substantially from the previously obtained correlation with 15-cm data, mostly in the direction of an increased double ion fraction. A more detailed examination, though, shows that the 30-cm data farthest above the 15-cm data were all obtained at high discharge voltages. But high discharge voltages are consistent with a large production rate for doubly charged ions produced by a one-step process.

To check the effect of the one-step process on the 30-cm data, the derivation of the double-ion parameter was repeated, except that both the one-step and two-step production of doubly charged ions from primary electrons were included.* This modified double-ion parameter resulted in a much improved correlation of data, especially the data obtained at

---

*Doubly charged ions can also be produced by the background Maxwellian electrons. The Maxwellian electron temperature, however, tends to decrease with increasing thruster size, so that this process becomes relatively unimportant for large thrusters.

high discharge voltages. Unfortunately, the modified parameter is also much more complicated, in that it must include cross sections for both one-step and two-step processes at primary electron energy. Also, most thruster applications are limited to small double-ion fractions, where the one-step process is, indeed, small.

A derivation of the modified parameters, including one-step double ionization from primary electrons, is presented in Appendix B.

For thruster applications, then, the correlation indicated by the 15-cm data, or the 30-cm data at moderate voltages, is recommended for design-stage predictions. The agreement between 15-cm and 30-cm data (at moderate discharge voltages) indicates that extrapolation to even larger thruster sizes may be reasonable. A careful comparison of the more complicated correlation described above with the correlation indicated in Fig. 8 indicates that the average contribution of one-step double ionization may be as much as 40% of the total double ionization measured. The double-ion correlation of Fig. 8 thus represents a dominant two-step process, but with still a significant contribution from the one-step process.

IV. ION REFLECTION EXPERIMENT

Electric propulsion applications would, in general, benefit from lower discharge losses. This is particularly true for lower specific impulses, where the effect of discharge loss on overall efficiency is greater. One of the approaches to reducing discharge losses that has been studied in the past is ion reflection at the boundaries of the discharge chamber.

To the first approximation, ions produced in a discharge chamber tend to propagate equally in all directions. The discharge losses per extracted ion are therefore roughly proportional to the total area around the production region divided by the extraction area. The production region is, of course, approximated as the primary electron region - where primary electrons cannot be intercepted by the anode without first undergoing a collision. The approach of interest here is the possible reflection of ions at a non-extraction boundary, thus reducing the effective loss area for ions.

The first clear description of this ion reflection concept in the electric propulsion field was by Moore[10] and Ramsey.[11] It was referred to as magneto-electrostatic containment, or MESC. In MESC the anodes were biased positive of the discharge plasma, so that ions approaching the anodes would be reflected, saving them for extraction into the ion beam. Using this approach, Ramsey reported Hg discharge losses of 155-160 eV/ion at 90% utilization. This loss was approximately two-thirds of what would be expected from the extraction area and the area surrounding the production region. It therefore appears clear that some degree of reflection was actually taking place.

The experiment to be described next was not successful, in the sense that ion reflection was not achieved. It should be of interest, however, for any program directed at reducing discharge losses.

The anodes of a rectangular-beam multipole ion source[12] were biased as indicated in Fig. 9. The relative bias between the two sets of anodes was small compared to the total discharge voltage, so both sets were still positive relative to the electron emitting cathode. An anode was not installed where the cathode supports are indicated. Otherwise, all the anodes opposite the ion optics were biased positive relative to the other anodes. The discharge power was assumed to be the total of the powers through the two sets of anodes.

It was hoped that the positively biased anodes would become positive relative to the discharge plasma. Such a bias was, indeed, verified in separate tests with Langmuir probes. It was also hoped that the bias would, at some point, result in ion reflection and reduced discharge losses. As indicated in Fig. 10, such a reduction did not take place. To the first approximation, no change in discharge loss occurred. A more careful examination indicates that the discharge losses increased slightly with increasing anode bias.

As indicated earlier, this test was not successful in that it did not achieve the hoped for reduction in discharge losses. Inasmuch as the anodes could be biased positive of the discharge plasma, the lack of ion reflection still remains to be explained. At this point the best explanations appear to involve magnetic field strength and transient behavior.

The diffusion of electrons across the magnetic field to the anodes has been shown to be in the "anomalous" or "turbulent" diffusion regime.[9]

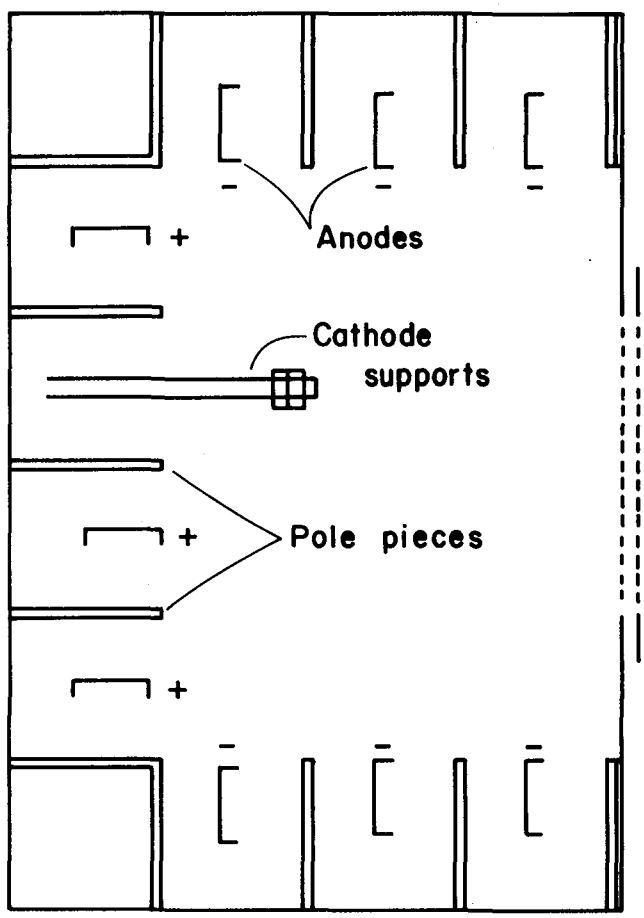

Fig. 9. Anode bias configuration used in rectangular-beam thruster.

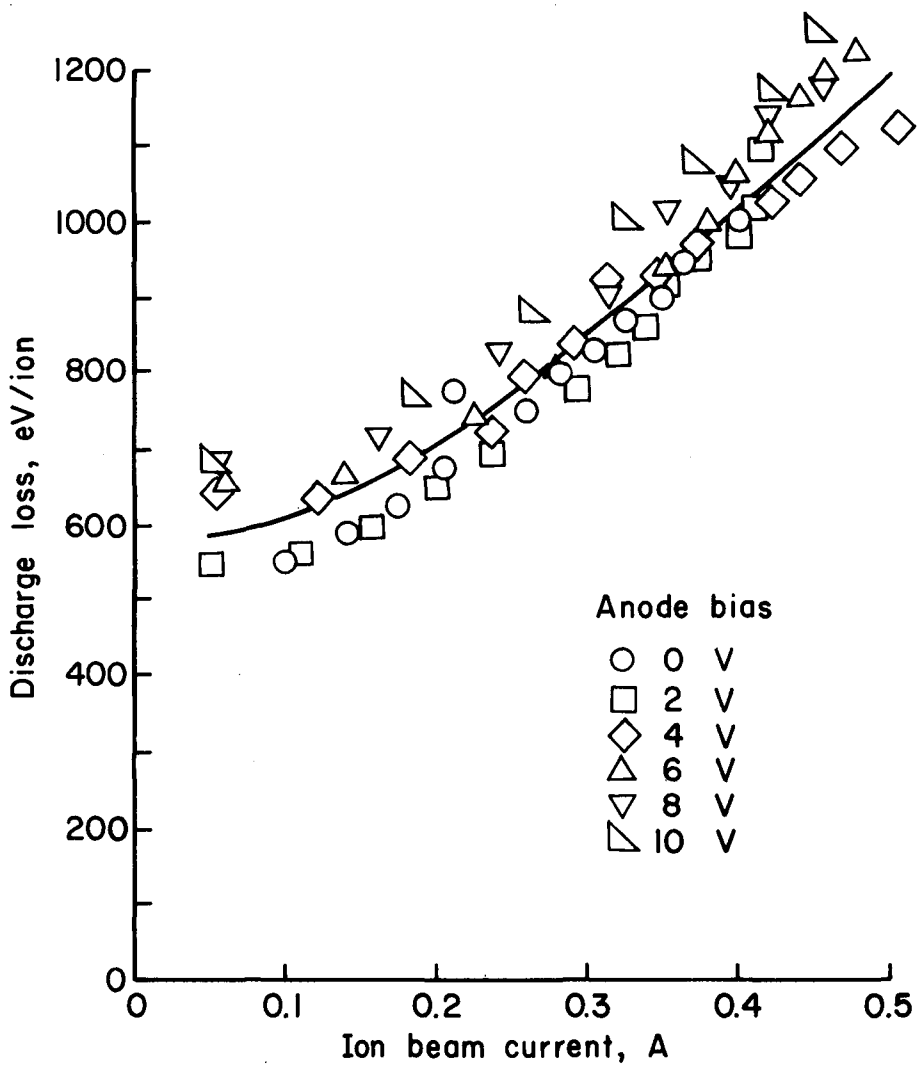

Fig. 10. Effect of anode bias on discharge-chamber performance of rectangular-beam thruster.

That is, the electron diffusion across the magnetic field is not a steady-state process. Instead, it is accompanied by fluctuations in density and potential. Thus, despite a time-averaged potential that would tend to reflect ions, the fluctuations could still permit ions to reach the vicinity of the anodes.

The magnetic field integral ($\int B \times dx$) between the bulk of the discharge chamber and an anode was, for the rectangular-beam ion source, just sufficient to deflect primary electrons back into the discharge chamber. For the discharge chamber used by Ramsey, the magnetic integral was several times higher. So high, in fact, that a separate "plasma anode", unprotected by magnetic field, was required for the completion of the discharge circuit. This difference in magnetic field integral may have been sufficient to permit some ion reflection despite the fluctuations expected in the diffusion process. At this point, however, the information is not sufficient to draw a clearcut conclusion.

V. SINGLE-GRID ION OPTICS

Electric propulsion offers substantial payload advantages over chemical rockets for geocentric orbit-raising missions. Trip time, however, is often a serious concern for such missions. To minimize the increased trip time normally associated with electric-propulsion orbit-raising missions, relatively low specific impulses are of interest.

With both two-grid[13] and three-grid[14] ion optics, the space charge between the grids serves to limit the possible ion-beam current density at low specific impulses. Decreasing the spacing between grids will increase the ion current density, but there are practical limits involved in this reduction of grid spacing.[15]

Single grid optics have been used to generate very low energy ion beams,[16,17] but have not previously been proposed for electrostatic thrusters. As discharge chambers become more efficient, the permissible minimum specific impulse from an efficiency viewpoint drops. If the ion energy is permitted to be low enough, it will approach the sputtering threshold and adequate lifetime will be assured. For example, a 30 eV argon ion (near the sputtering threshold) still has a velocity corresponding to about 1200 seconds.

The major performance considerations for single-grid ion optics, besides durability, are the fraction of ions transmitted and the divergence characteristics of the transmitted ion beam. If, as indicated in Fig. 11(a), the ion sheath, ℓ_s, is large compared to the accelerator hole diameter, d_a, the accelerated ions will "see" a nearly uniform potential at the accelerator grid. The fraction of ions escaping into the ion beam will then approximate the open-area fraction of the accelerator. If, on the other hand, as indicated in Fig. 11(b), the sheath

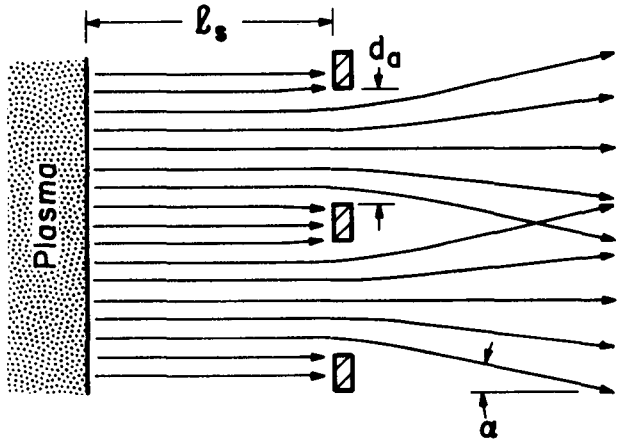

(a) Large relative sheath thickness

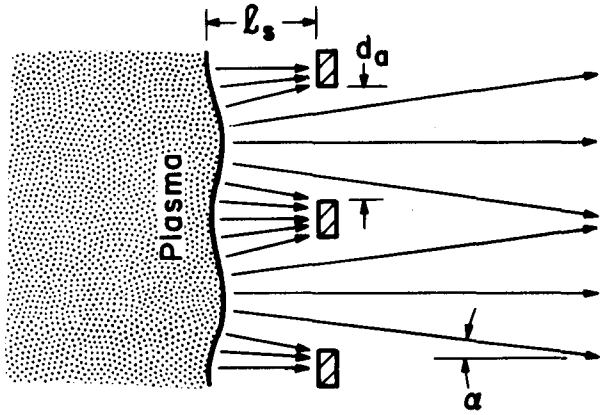

(b) Small relative sheath thickness

Fig. 11. Single-grid operation at different relative sheath thicknesses (ℓ_s/d_a).

thickness approaches the accelerator hole diameter, a larger fraction of the ions will be directed toward the accelerator grid.

The sheath thickness is, of course, determined by the ion current density arriving at the sheath, the potential difference between the plasma and the accelerator grid, and the charge-to-mass ratio of the ion being accelerated. For the sheath thicknesses presented herein, Child's law was used. That is, a simple one-dimensional planar distribution of potential was assumed, with no correction for the apertures in the accelerator grid. The central portion of a large multipole thruster was used to assure uniformity over the ∿1 cm beam diameter used. The open area fraction of the accelerator used was 43%. A much higher open-area fraction would be required for an actual propulsion application.

The extraction ratio is the ion current extracted divided by the product of ion-current density at the sheath and the accelerator open area, $J_b/j_s A_{ex}$. This extraction ratio is presented in Fig. 12 as a function of relative sheath thickness, ℓ_s/d_a. It is clear from the distribution data that, for the same value of ℓ_s/d_a, the extraction ratio increases monotonically with R, the net-to-total voltage ratio.

The variation in extraction with R might be expected from the aperture effect at the accelerator grid. As R is decreased, the potential distribution within the apertures will change so as to deflect more ions into the accelerator grid. This increased impingement due to a decreased R, can, of course, be offset by an increase in sheath thickness, so that the ions acquire a greater fraction of their total energy before reaching the vicinity of the accelerator aperture. Inversely, one might expect to correct the performance to a higher value of R by subtracting some fraction of the sheath thickness. Experimentally, this correction of ℓ_s/d_a due to R was found to be about

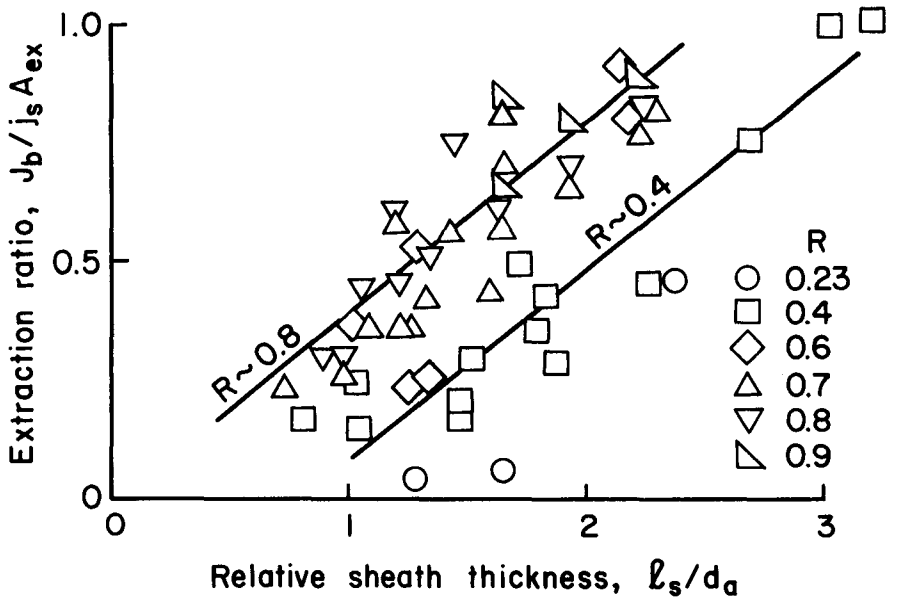

Fig. 12. Single-grid performance for a range of net-to-total voltage range, R.

$$\Delta \ell_s/d_a \sim -2\ (0.8 - R)\ , \tag{1}$$

with 0.8 used as the reference value of R.

The preceding equation was used to correct all values of ℓ_s/d_a to what would be expected for R = 0.8. The corrected data were then plotted as shown in Fig. 13. The lack of any clear ordering for different values of R in Fig. 13 indicates that the correction for different values of R was at least approximately correct.

The mean line shown in Fig. 13 can be described by an equation.

$$J_b/j_s A_{ex} \sim 0.4\ (\ell_s/d_a) - 0.8\ (0.8 - R) \tag{2}$$

If the extraction ratio, $J_b/j_s A_{ex}$, from this equation, exceeds 1.0, a value of 1.0 should be used instead. This is because there is no physical reason to expect ions to be deflected away from the accelerator grid for R values less than 1.0. And R values less than 1.0 are required to prevent electron backstreaming.

Several means of correlating the ion beam divergence angle were tried, with Fig. 14 showing the clearest correlation. The angle α shown in Fig. 14 is the half-angle that encloses 95% of the total ion beam. The half-angle at which the ion current density was half the peak value was typically about half the value of α given in Fig. 14.

The results shown in Fig. 13 indicate that high extraction ratios can be achieved at sheath thicknesses several times the accelerator hole diameter. If a high open-area fraction is used for the accelerator grid, the fraction of ions extracted should also be high. The beam divergence can be quite large, as indicated by Fig. 14. The beam divergence can be expected to decrease if ℓ_s/d_a is increased beyond the

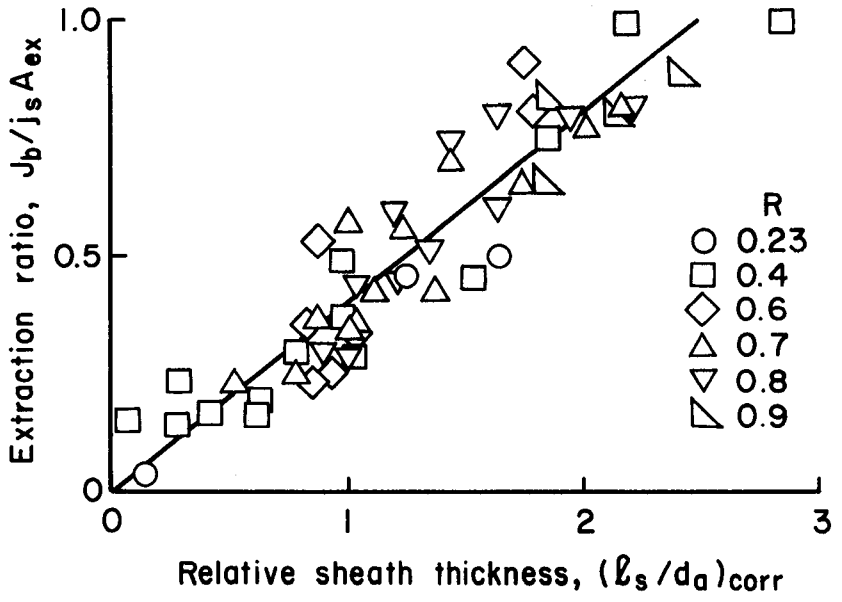

Fig. 13. Single-grid performance with ℓ_s/d_a corrected to a net-to-total voltage ratio of 0.8.

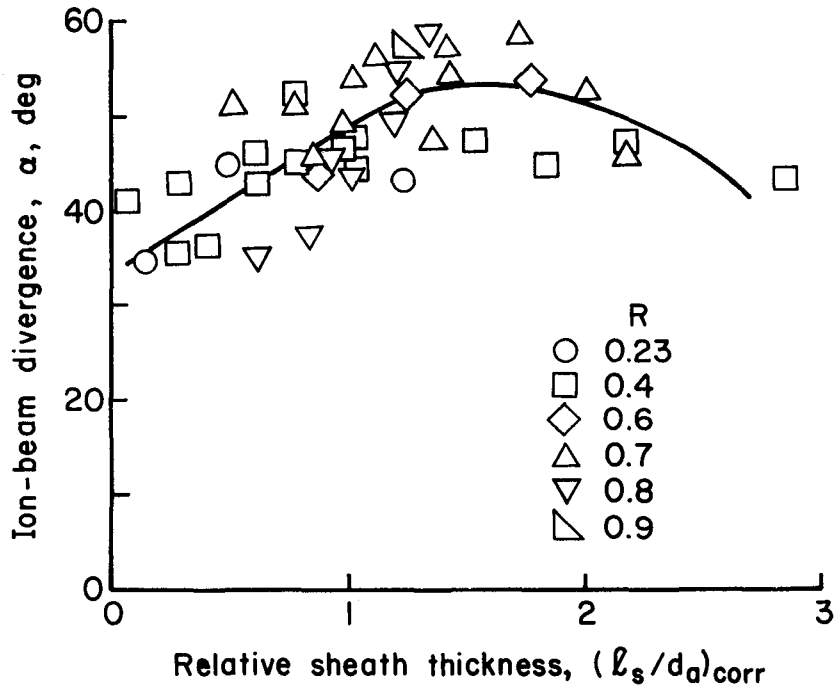

Fig. 14. Ion-beam divergence as a function of ℓ_s/d_a, with the latter corrected to a net-to-total voltage ratio of 0.8.

range shown in Fig. 14. The results shown in Figs. 13 and 14 are limited in that only one accelerator-grid configuration was used. These results should, however, still be useful for performance estimates.

VI. CONCLUDING REMARKS

Compared to previous tests with an open keeper, an enclosed keeper hollow cathode gave 60-70% higher electron emissions. At an argon flow of 0.4-0.6 A-equiv, the enclosed keeper design gave emission-to-flow ratios of 28-33 A/A-equiv. In comparison the open keeper design only reached 16-23 A/A-equiv.

A hollow cathode with a carbon tip and a glow-discharge heater was also operated. Unlike the conventional hollow-cathode design, no emissive oxide was used. Comparison with the performance of a conventional hollow cathode indicated that an additional anode-cathode voltage was required which provided the extra heating power for operation without oxide. The carbon tip design appears promising for larger hollow cathodes, where use of the conventional design could result in serious thermal stresses at the tip weld.

Double-ion data from a 30-cm thruster operated at moderate voltages indicated agreement with a double-ion correlation obtained previously with data from a 15-cm thruster. This agreement indicates that extrapolation to even larger thruster sizes may be reasonable. Operation at moderate discharge voltages is important if the assumed two-step double-ionization process is to dominate. This assumption, however, should be easily met with designs intended to have long lifetimes.

An ion reflection experiment was conducted with some of the anodes biased relative to the rest. It was hoped that ion reflection would take place when the positively biased anodes became more positive than the discharge plasma, resulting in reduced discharge losses. Although some anodes became more positive than the discharge plasma, no reduction in discharge losses was observed. The most likely explanations for the

absence of ion reflection appear to involve the magnetic field strength used and the fluctuations known to exist near the anodes.

A single-grid ion-optics configuration was evaluated for possible use at, for electrostatic thrusters, low specific impulses. The transmitted ion current increased with the ratio of sheath thickness to accelerator hole diameter up to a ratio of 2-3. At this ratio the transmitted ion current corresponded to about the projected open area of the accelerator. The half-angle of beam divergence was quite large, ranging from about 30-60° (for 95% of the beam within this angle). A reduction in this half angle would be expected for larger sheath thicknesses - more than 2-3 times the accelerator hole diameter. The maximum useful specific impulse for single-grid optics is limited due to the sputtering from direct ion impingement. Within this limit, though, the single-grid approach offers a means of avoiding the usual span-to-gap limits of multiple-grid ion optics.

REFERENCES

1. H. R. Kaufman, "Experimental Investigations of Argon and Xenon Ion Sources," NASA Contr. Rep. CR-134845, June 1975.

2. H. R. Kaufman, "Inert Gas Thrusters," NASA Contr. Rep. CR-135100, July 1976.

3. H. R. Kaufman, "Inert Gas Thrusters," NASA Contr. Rep. CR-135226, July 1977.

4. H. R. Kaufman, "Inert Gas Thrusters," NASA Contr. Rep. CR-15927, Nov. 1978.

5. H. R. Kaufman and R. S. Robinson, "Inert Gas Thrusters," NASA Contr. Rep. CR-159813, Nov. 1979.

6. H. R. Kaufman, "Technology of Electron-Bombardment Ion Thrusters," in Advances in Electronics and Electron Physics, Vol. 36, pp. 265-373, 1974, Academic Press, New York.

7. R. R. Peters, "Double Ion Production in Mercury Thrusters," NASA Contr. Rep. CR-135019, Apr. 1976.

8. P. J. Wilbur, "Argon-Xenon Discharge Chamber Model for the Production of Doubly Charged Ions," pp. 46-64, in Ref. 3.

9. H. R. Kaufman and R. S. Robinson, "Plasma Processes in Inert Gas Thrusters," AIAA Paper No. 79-2055, Oct./Nov. 1979.

10. R. D. Moore, "Magneto-Electrostatically Contained Plasma Ion Thruster," AIAA Paper No. 69-260, Mar. 1969.

11. W. D. Ramsey, "12-cm Magneto-Electrostatic Containment Mercury Ion Thruster Development," J. Space. Rockets, Vol. 9, pp. 318-321, May 1972.

12. R. S. Robinson, H. R. Kaufman, and C. M. Haynes, "A 5 × 40 cm Rectangular-Beam Multipole Ion Source," AIAA Paper No. 81-0667, Apr. 1981.

13. G. Aston, H. R. Kaufman, and P. J. Wilbur, "Ion Beam Divergence Characteristics of Two-Grid Accelerator Systems," AIAA J., Vol. 16, pp. 516-524, May 1978.

14. G. Aston and H. R. Kaufman, "Ion Beam Divergence Characteristics of Three-Grid Accelerator Systems, AIAA J., Vol. 17, pp. 64-70, Jan. 1979.

15. H. R. Kaufman and R. S. Robinson, "Ion Source Design for Industrial Applications," AIAA Paper No. 81-0668, Apr. 1981.

16. P. LeVaguerèse and Pigache, "Édude d'une source d'ions de basse énergie et à forte densité de courant," Revue de Physique Appliquée, Vol. 6, pp. 325-327, Sept. 1971.

17. J. M. E. Harper, J. J. Cuomo, P. A. Leary, G. M. Summa, H. R. Kaufman, and F. J. Bresnock, "Low Energy Ion Beam Etching," Proc. Symp. Electron and Ion Beam Science and Tech., Proc. Vol. 80-6, Electrochem. Soc., Pennington, N.J., 1980.

APPENDIX A

HOLLOW CATHODE/ENCLOSED KEEPER/INERT GAS (Ar) PERFORMANCE DATA

by Donald C. Trock

Several configurations of enclosed-keeper hollow cathodes were operated for a range of keeper aperture diameters, keeper spacings, and argon flow rates. The detailed results are presented in the following figures:

Figure A-1 shows the first hollow cathode with enclosed keeper configuration used, while Fig. A-2 shows representative baseline data for the same hollow cathode, but with a standard Ta wire ring keeper. Since the tests were conducted over a wide range of Ar flow, and attendant variations in background pressure, Fig. A-3 quantifies the effects of background pressure for the system used in these tests.

Figures A-4 through A-7 present the data collected from the configuration of Fig. A-1. These tests were of limited usefullness because of high temperatures created by the boron nitride gas seal. It proved to be impractical to exceed 10 A anode current, so this series of tests were discontinued.

Prior to completely reconstructing the test cathode, some alternate keeper configurations were briefly tested. Figure A-8 shows the three geometries tried. Figure A-8(a) geometry proved to be inoperable, while the geometry of Fig. A-8(b) provided only a limited range of operation as shown in Fig. A-9. The geometry of Fig. A-8(c) was quite functional and provided the data shown in Fig. A-10.

Figure A-11 shows the next test configuration constructed which effectively solved the high temperature problem. A lengthy series of

tests were then performed varying the keeper exit aperture diameter from 1 mm to 6.35 mm, varying the keeper aperture position between 1 mm and 9 mm from the cathode orifice plate, and varying Ar flow rates from as low as 200 mA-eq to as high as 1200 mA-eq. Figures A-12 through A-34 present the data from these tests.

Figures A-35 through A-39 cross-plot some of the collected data for easier analysis.

Figure A-40 shows one final cathode-keeper configuration tested. This geometry replaces the open keeper aperture with a Ta foil tube of the same diameter, which extends to a close proximity with the cathode orifice. The data for several diameters and lengths are presented in Fig. A-41 through A-44.

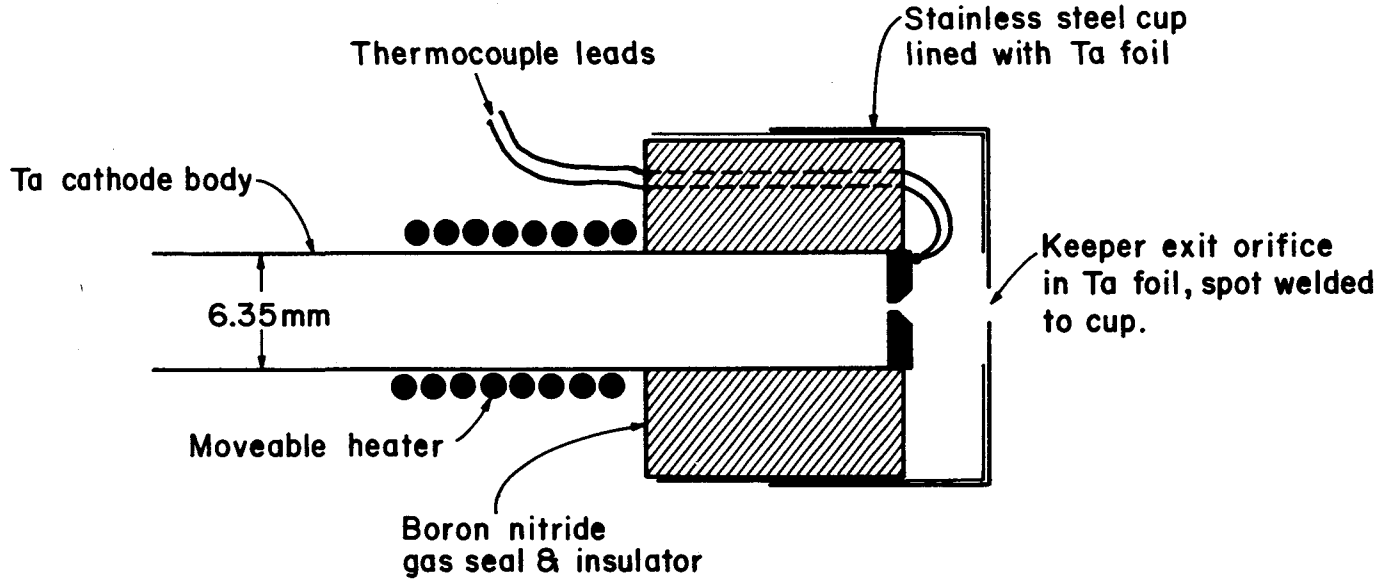

Fig. A-1. Hollow cathode with enclosed keeper. This is the first configuration tested. The stainless steel cup is moveable with respect to the boron nitride insulator, permitting variations in separation between the hollow cathode orifice and the keeper exit aperture. High cathode tip temperatures prohibited emission currents above 10 A. Cathode insert: porous tungsten with R-500 added. Cathode orifice: 0.635 mm. Keeper current: 300 mA for all tests.

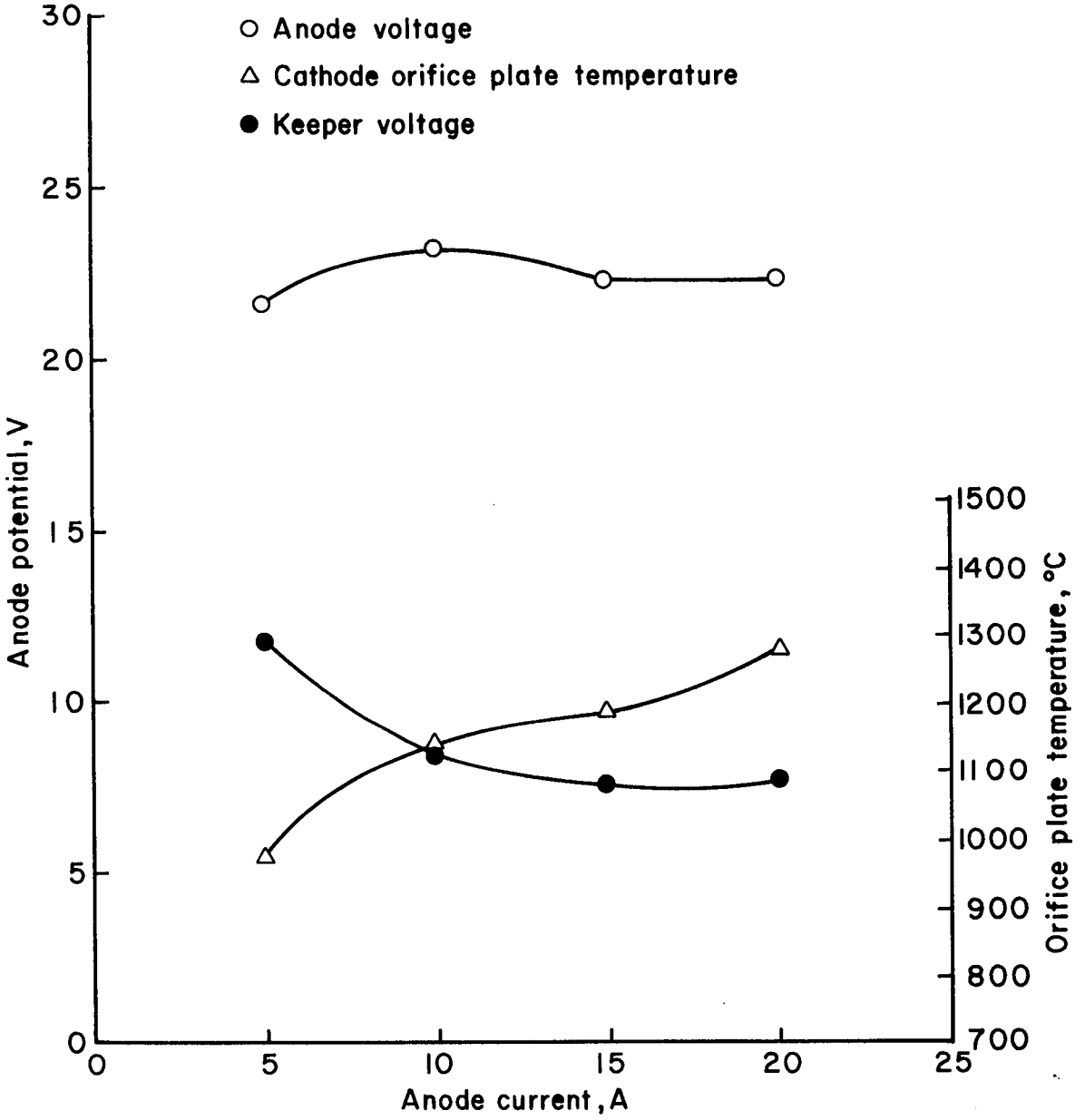

Fig. A-2. Hollow cathode baseline data. Hollow cathode from Fig. A-1 but with Ta wire ring keeper installed in place of enclosed keeper. Keeper aperture: 4 mm. Keeper position: 1 mm from orifice plate.

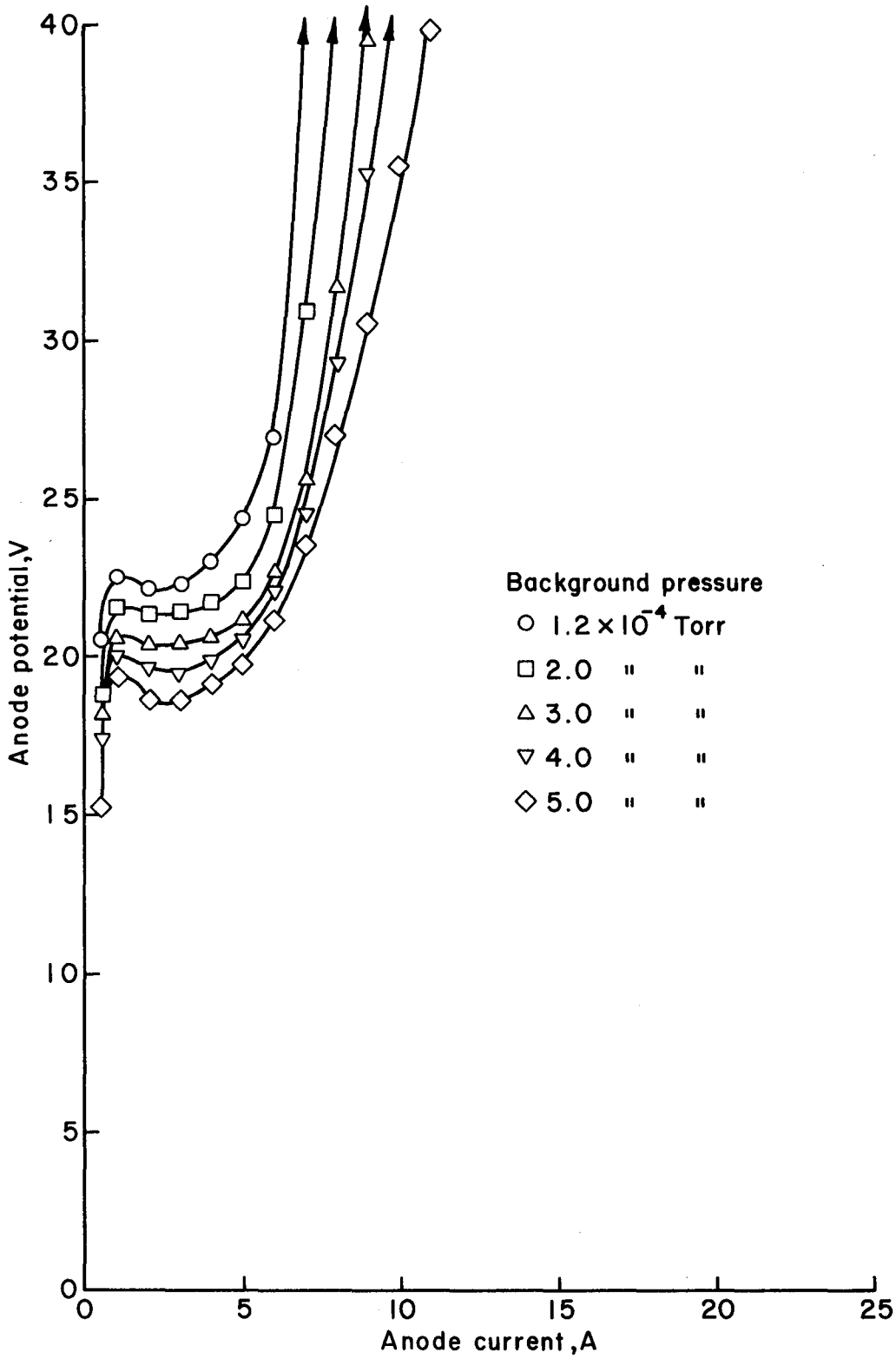

Fig. A-3. System background pressure effect. Cathode: 6.35 mm diameter, 0.76 mm orifice, with heat fin. Keeper: Ta wire ring, 4 mm aperture, 1 mm position from orifice plate. Ar flow: 400 mA. Background pressure varied by regulating diffusion pump gate valve.

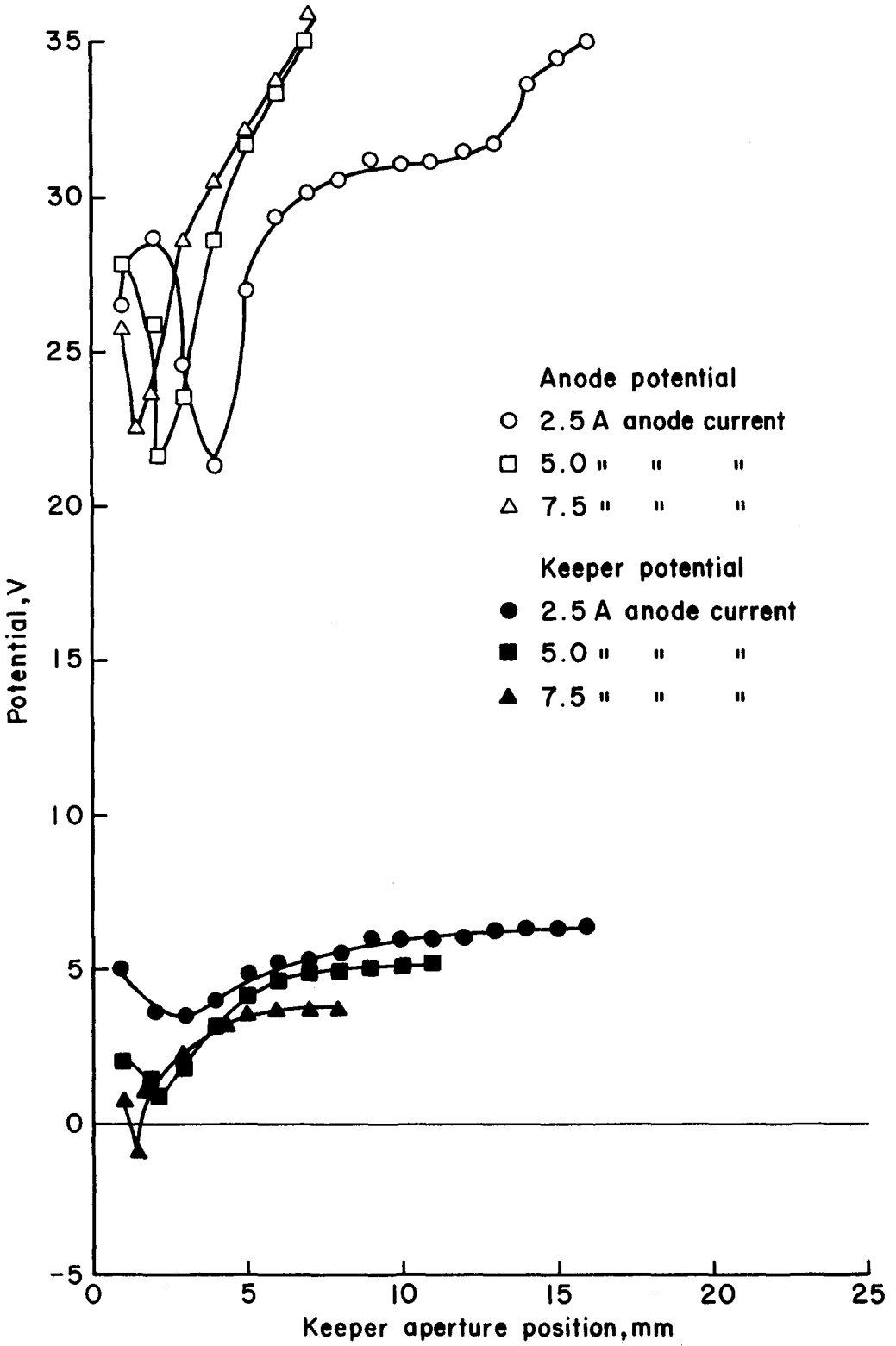

Fig. A-4. Hollow cathode/enclosed keeper performance as keeper position was varied with constant anode current. Test configuration: Fig. A-1. Keeper aperture: 1.5 mm. Ar flow: 800 mA. Cathode tip temperature rose to 1260°C at 7.5 A anode current.

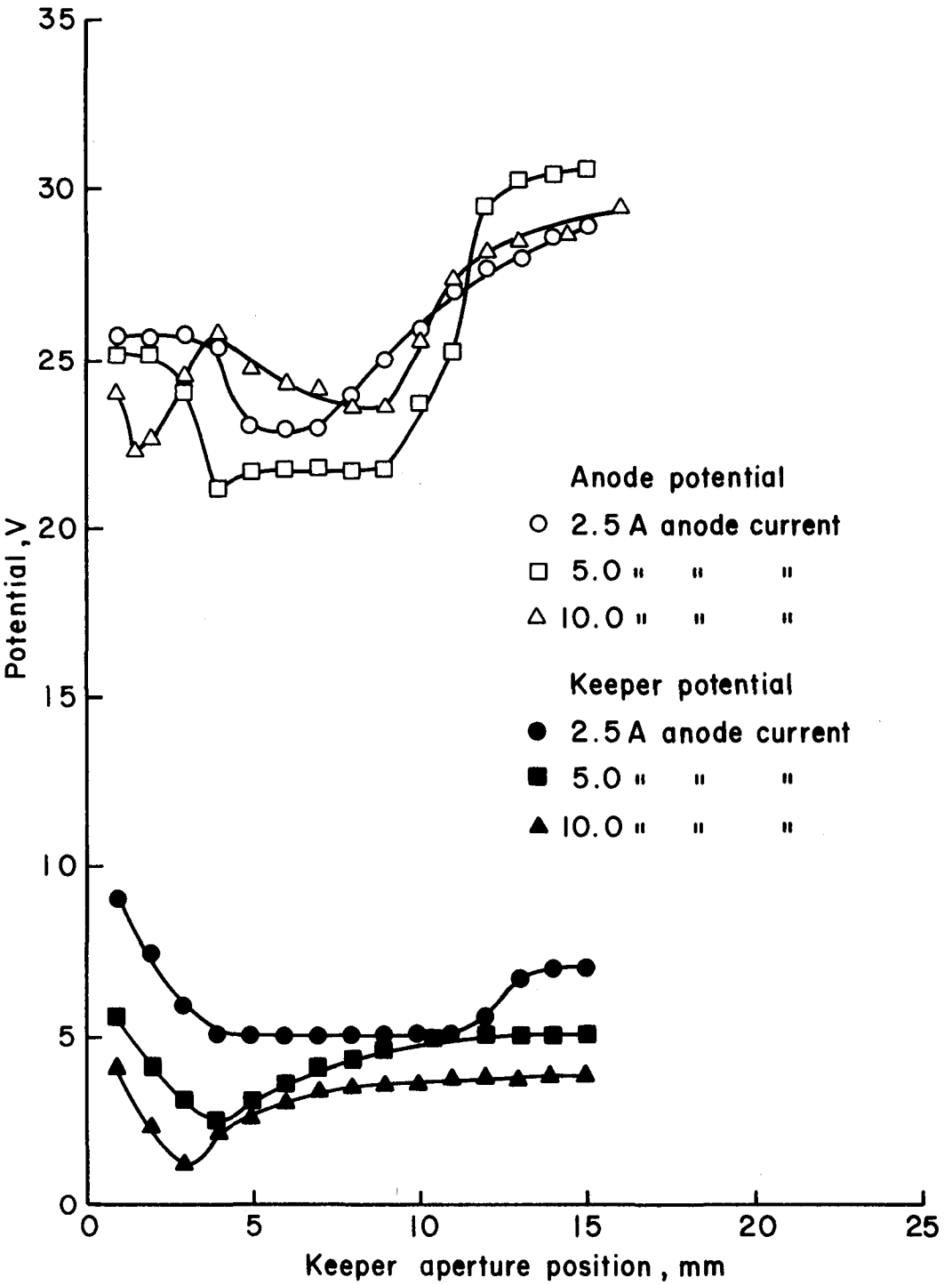

Fig. A-5. Hollow cathode/enclosed keeper performance as keeper position was varied with constant anode current. Test configuration: Fig. A-1. Keeper aperture: 2.5 mm. Ar flow: 800 mA. Cathode tip temperature rose to 1325°C at 10 A anode current.

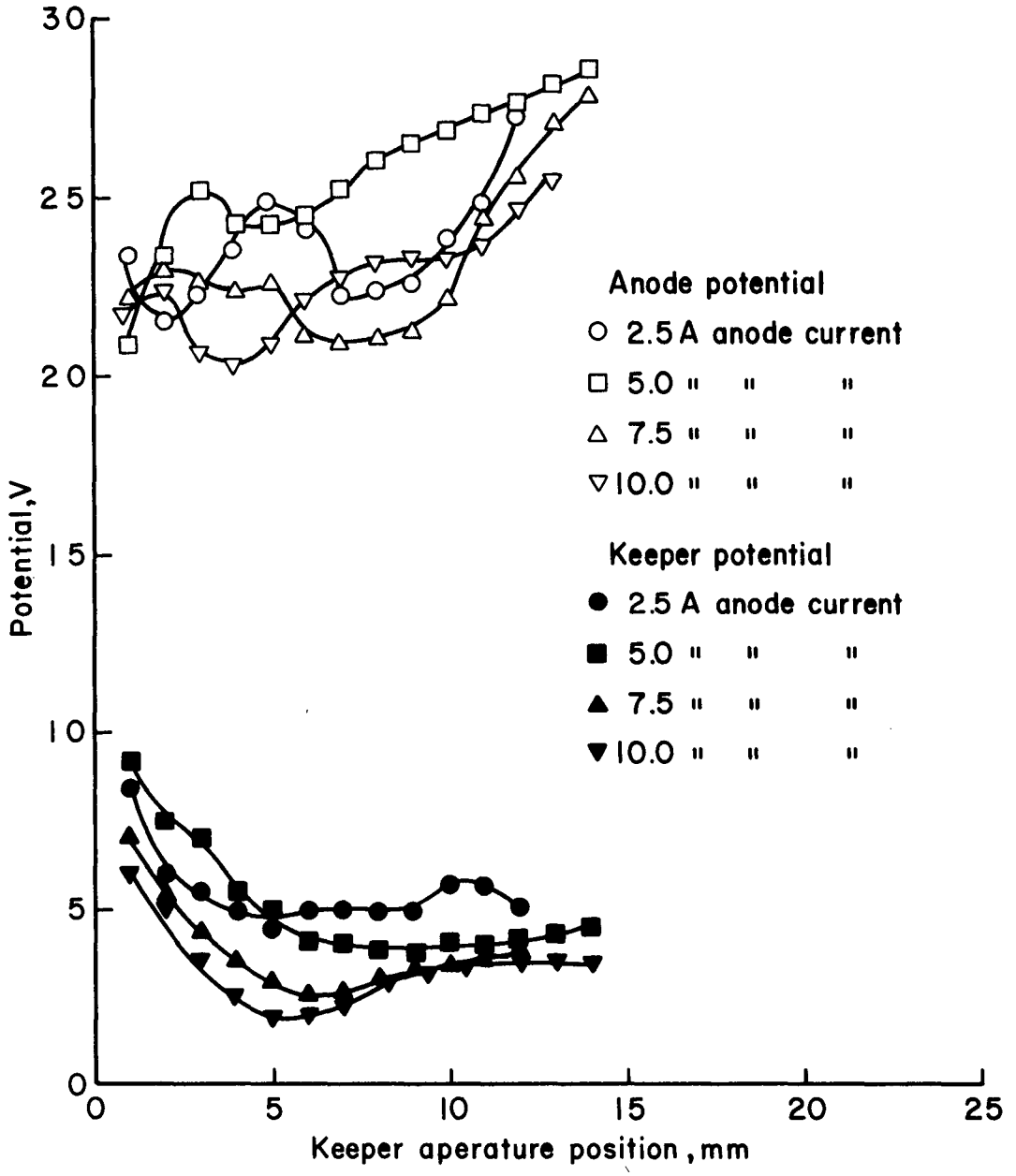

Fig. A-6. Hollow cathode/enclosed keeper performance as keeper position was varied with constant anode current. Test configuration: Fig. A-1. Keeper aperture: 4 mm. Ar flow: 800 mA. Cathode tip temperature rose to 1200°C at 10 A anode current.

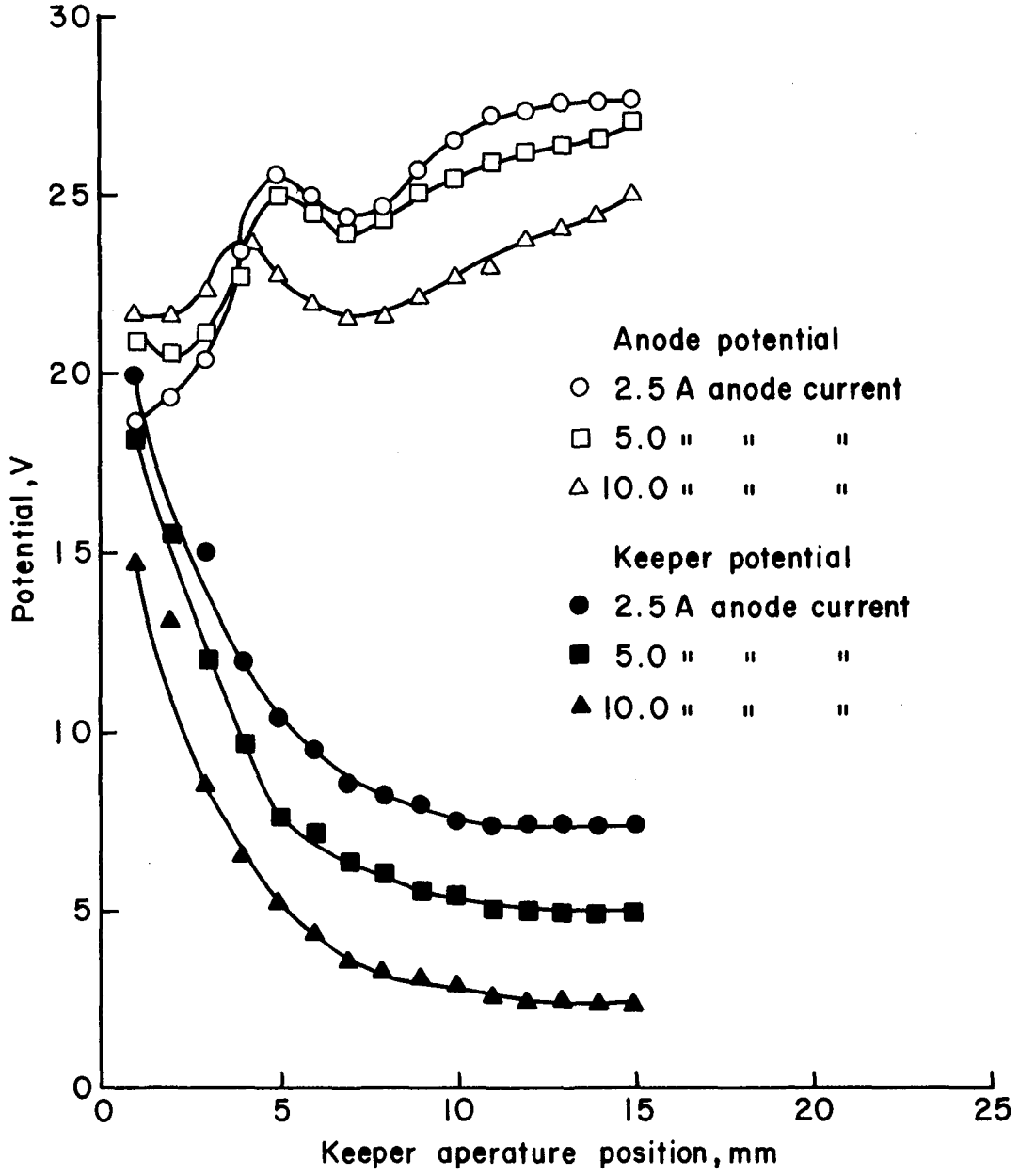

Fig. A-7. Hollow cathode/enclosed keeper performance as keeper position was varied with constant anode current. Test configuration: Fig. A-1. Keeper aperture: 6.35 mm. Ar flow: 800 mA. Cathode tip temperature rose to 1190°C at 10 A anode current.

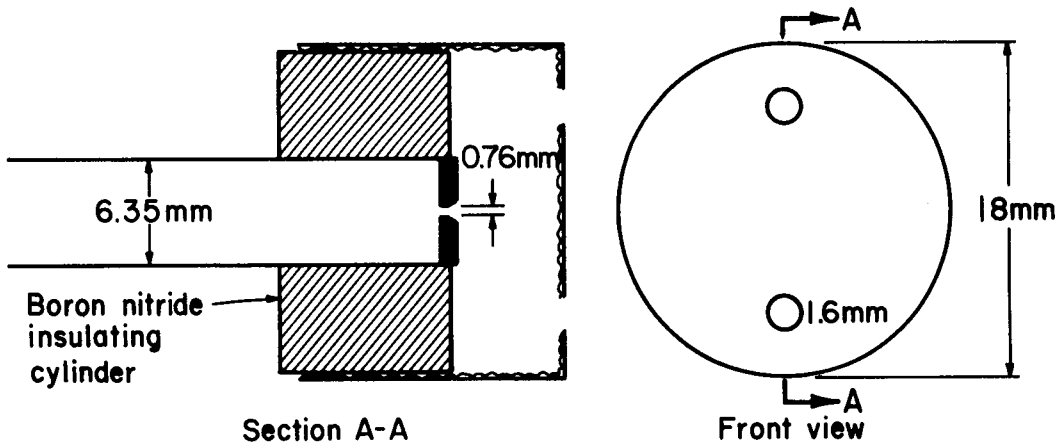

(a) Enclosed keeper with non-concentric apertures.

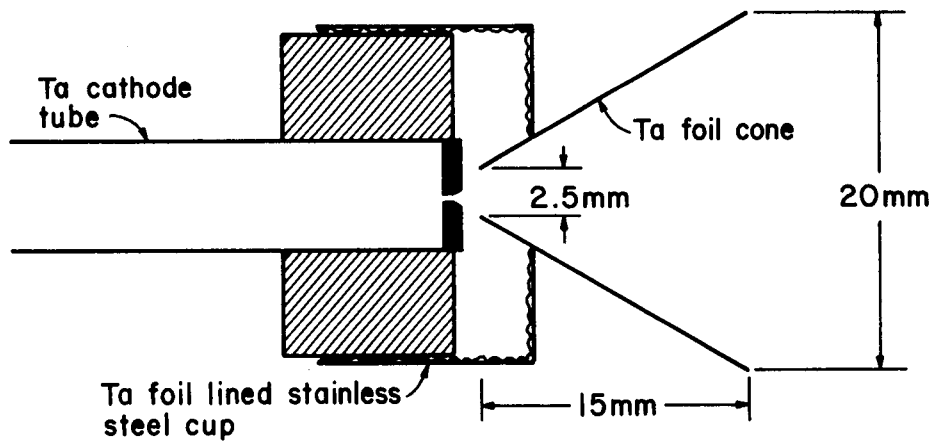

(b) Enclosed keeper with cone aperture.

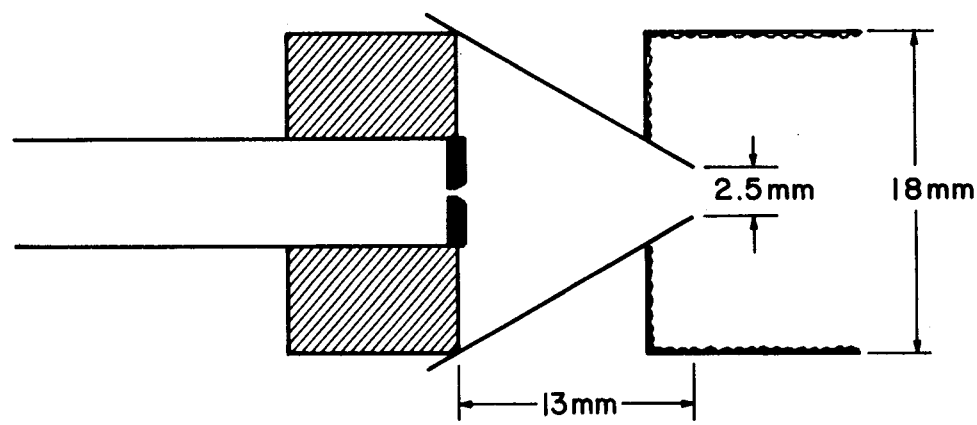

(c) Enclosed keeper with reversed cone

Fig. A-8. Three alternate enclosed keeper configurations which were briefly tested. Configuration (a) proved to be non-functional in that current could not be coupled to the anode. Performances of configurations (b) and (c) are shown on the following pages.

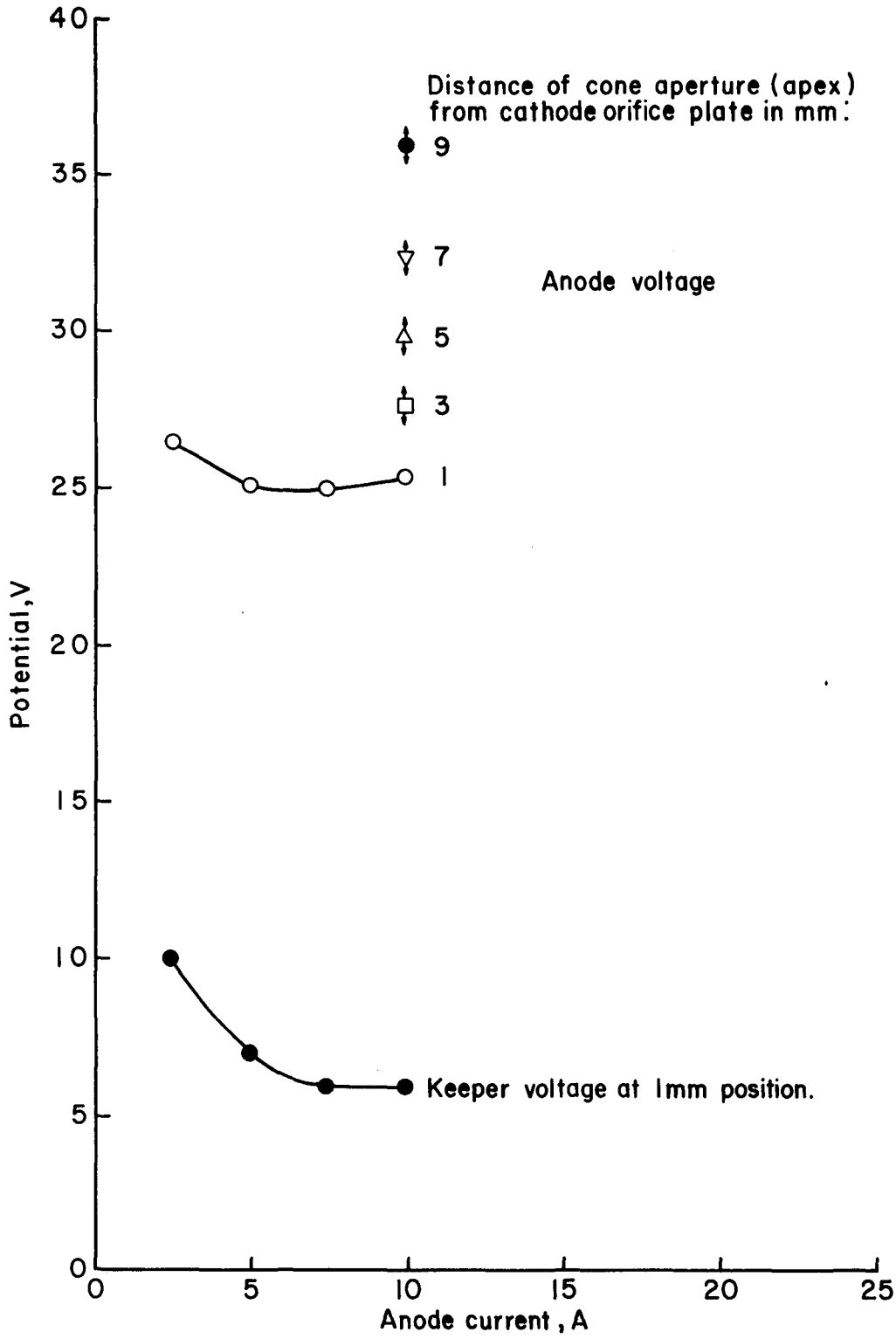

Fig. A-9. Enclosed keeper with cone aperture, (see Fig. A-8(b)), produced steady emission only when apex of cone was within 1 mm of cathode orifice. At 2 mm and greater separation, pulsing eratic emission resulted. Arrows on data points indicate estimated averages.

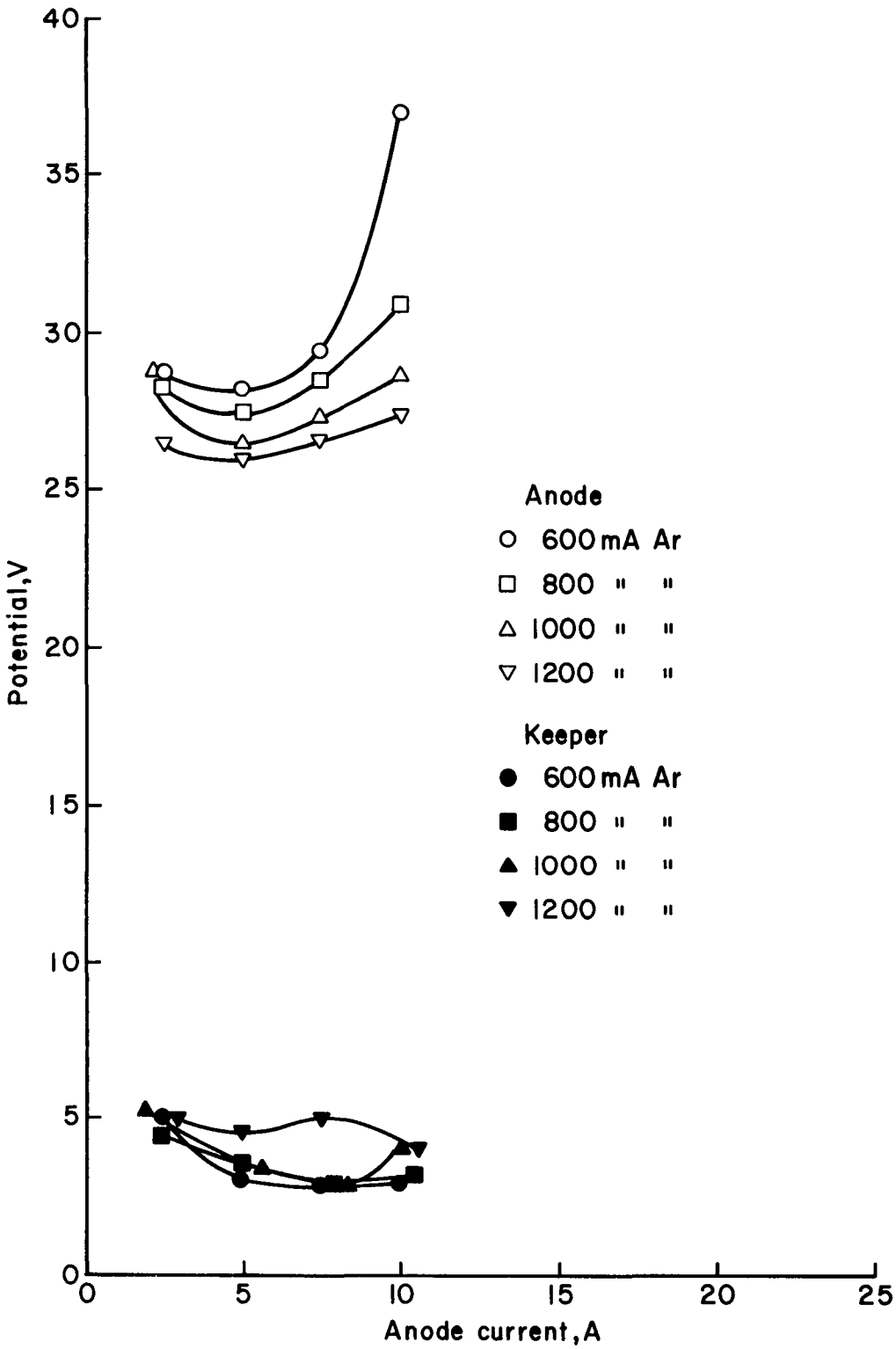

Fig. A-10. Enclosed keeper with reversed cone aperture, (see Fig. A-8(c)), produced a steady, quiet appearing plasma over a wide range of flows and anode currents.

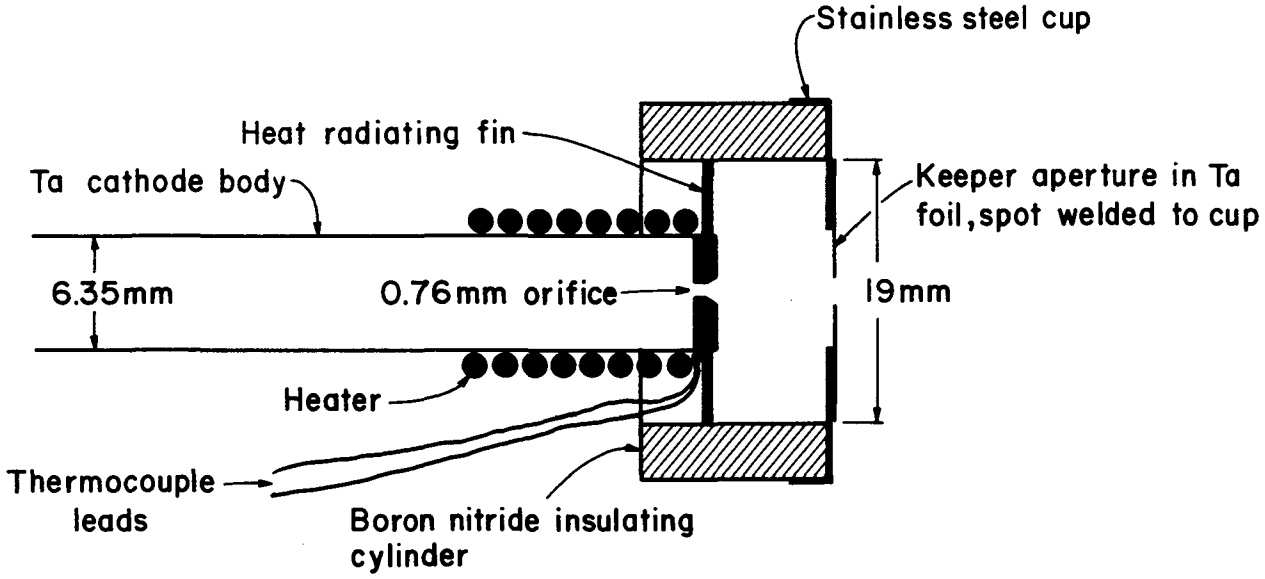

Fig. A-11. Hollow cathode with heat dissipating fin and enclosed keeper. This arrangement effectively dissipates heat and permits operation beyond the current limitations of the anode power supply of 20 A+. The enclosed keeper assembly moves with relation to the cathode and heat fin and permits adjustment of keeper aperture 0 - 9 mm from cathode orifice plate. Keeper operated at 300 mA for all tests.

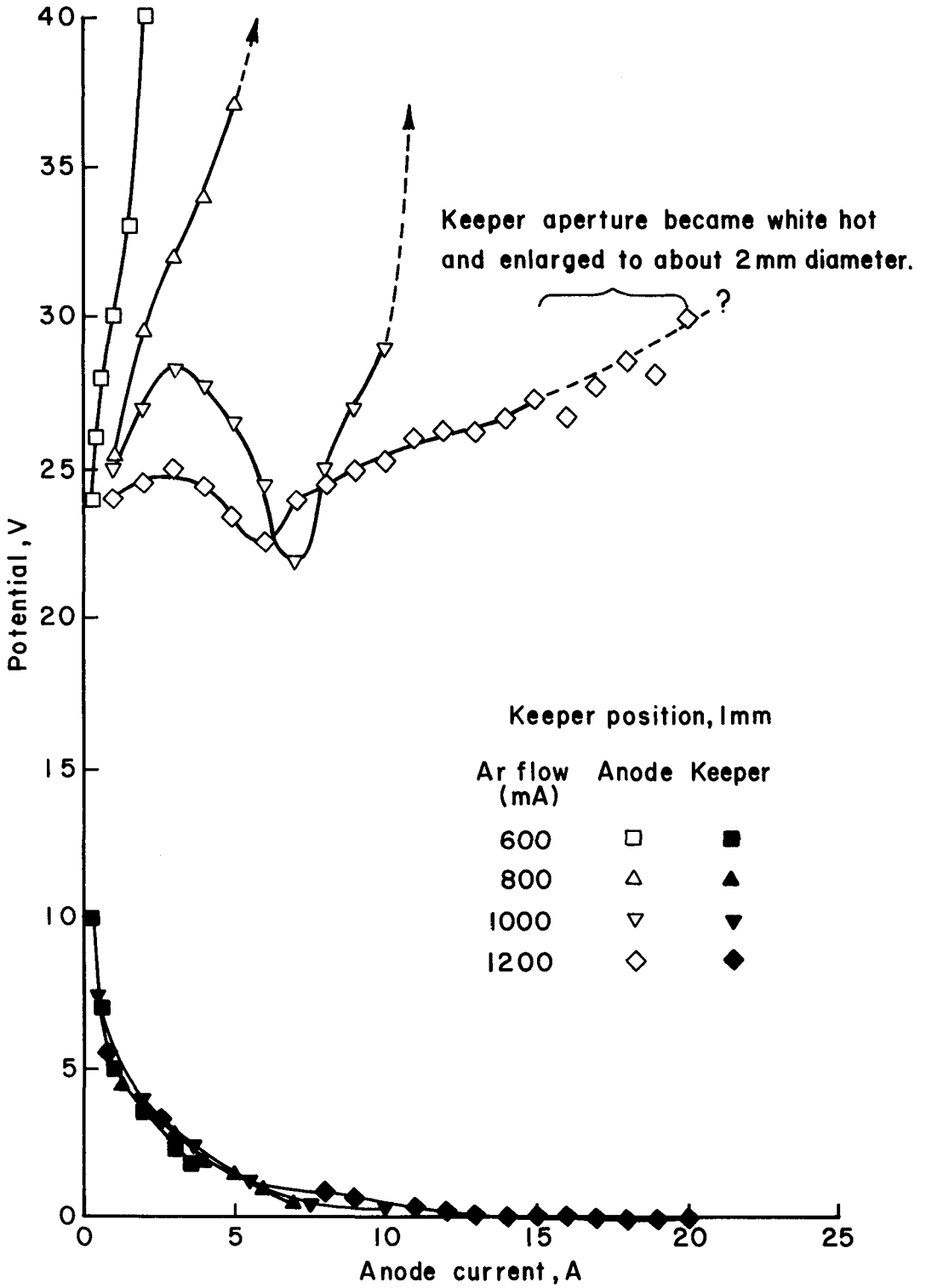

Fig. A-12. Hollow cathode/enclosed keeper performance. At this keeper aperture size, emission could be sustained only at the 1 mm keeper position, therefore several Ar flow rates are presented on this graph. Cathode temperature: 980°C at 1 A, to 1170°C at 20 A. Configuration: see Fig. A-11. Keeper aperture: 1 mm. Ar flow: as indicated by symbols.

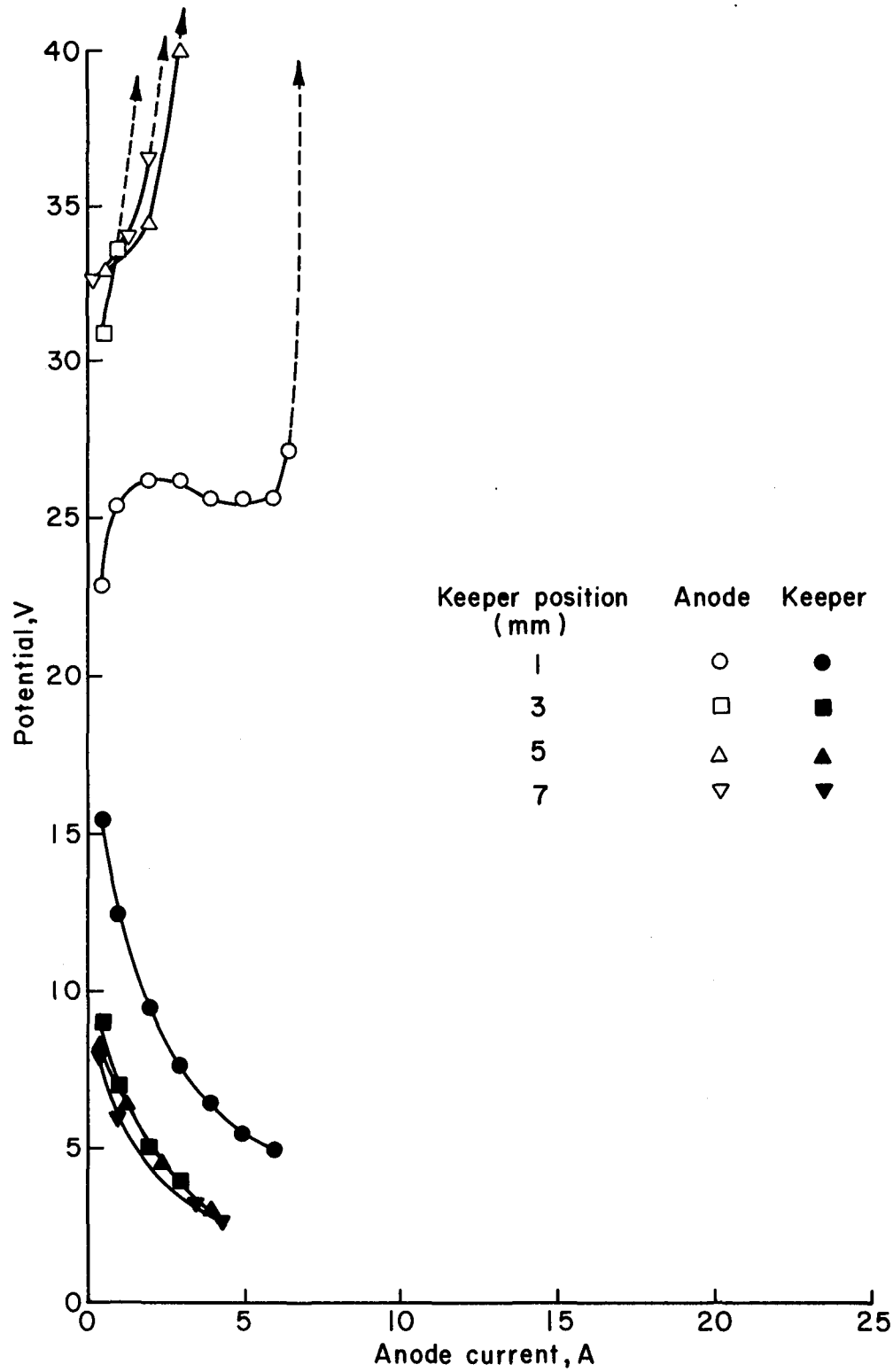

Fig. A-13. Hollow cathode/enclosed keeper performance. Configuration: see Fig. A-11. Keeper aperture: 2 mm. Ar flow: 400 mA. Cathode temperature: 975°C at 1 A, to 1075°C at 6 A.

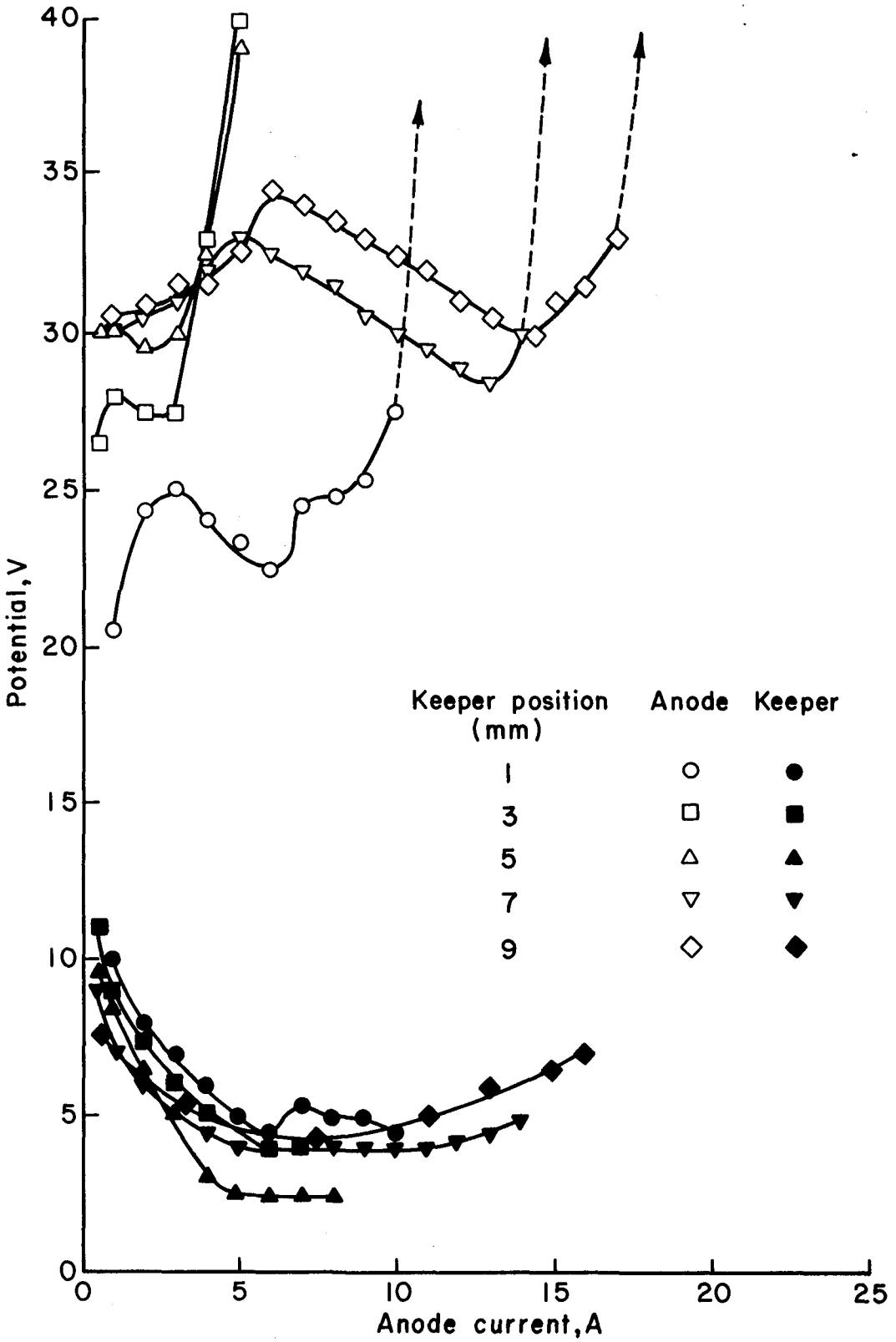

Fig. A-14. Hollow cathode/enclosed keeper performance. Configuration: see Fig. A-11. Keeper aperture: 2 mm. Ar flow: 600 mA. Cathode temperature: 935°C at 1 A, to 1165°C at 14 A.

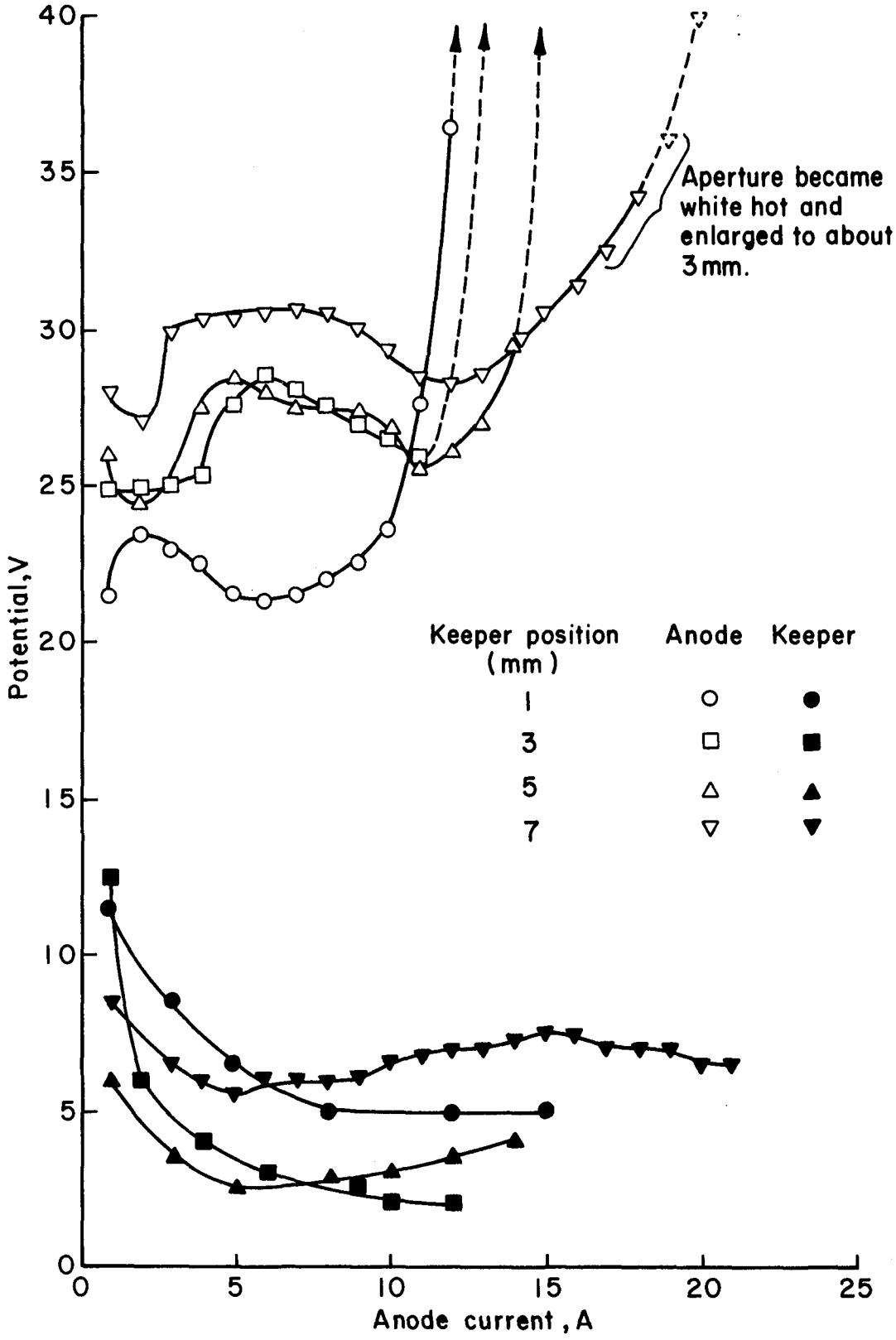

Fig. A-15. Hollow cathode/enclosed keeper performance. Configuration: see Fig. A-11. Keeper aperture: 2 mm. Ar flow: 800 mA. Cathode temperature: 935°C at 1 A, to 1325°C at 21 A.

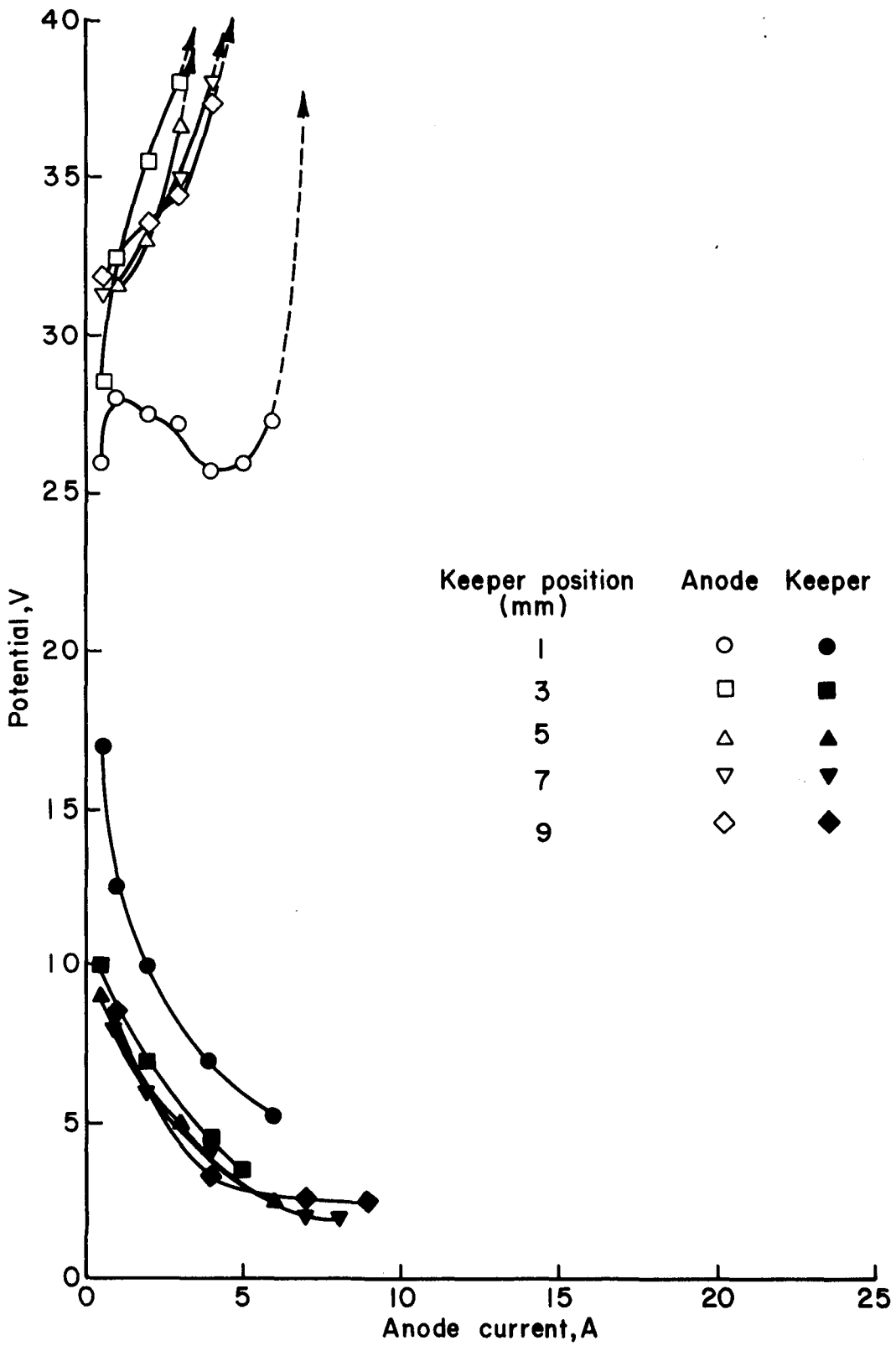

Fig. A-16. Hollow cathode/enclosed keeper performance. Configuration: see Fig. A-11. Keeper aperture: 3 mm. Ar flow: 400 mA. Cathode temperature: 915°C at 1 A, to 1100°C at 10 A.

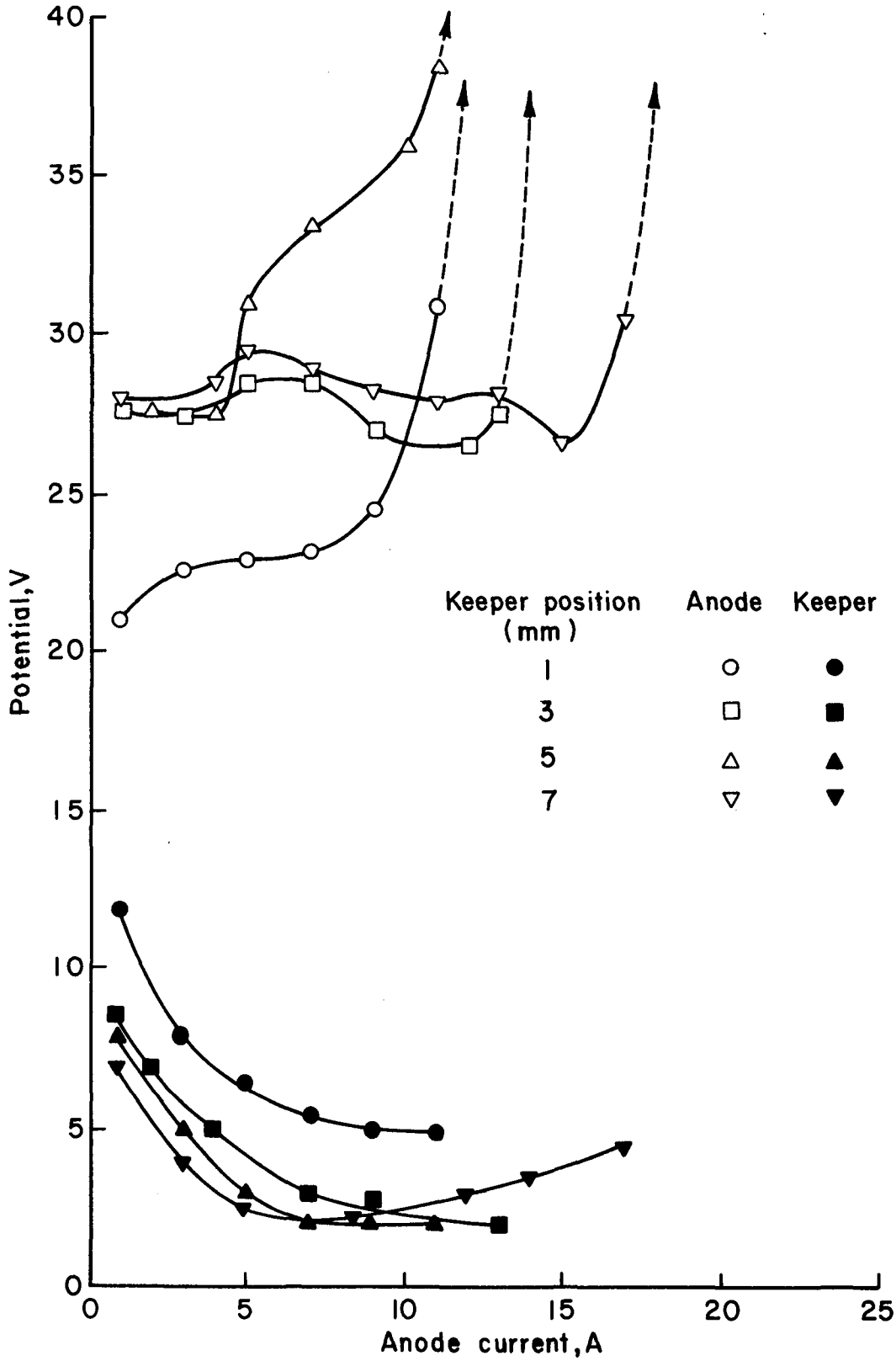

Fig. A-17. Hollow cathode/enclosed keeper performance. Configuration: see Fig. A-11. Keeper aperture: 3 mm. Ar flow: 600 mA. Cathode temperature: 925°C at 1 A, to 1150°C at 17 A.

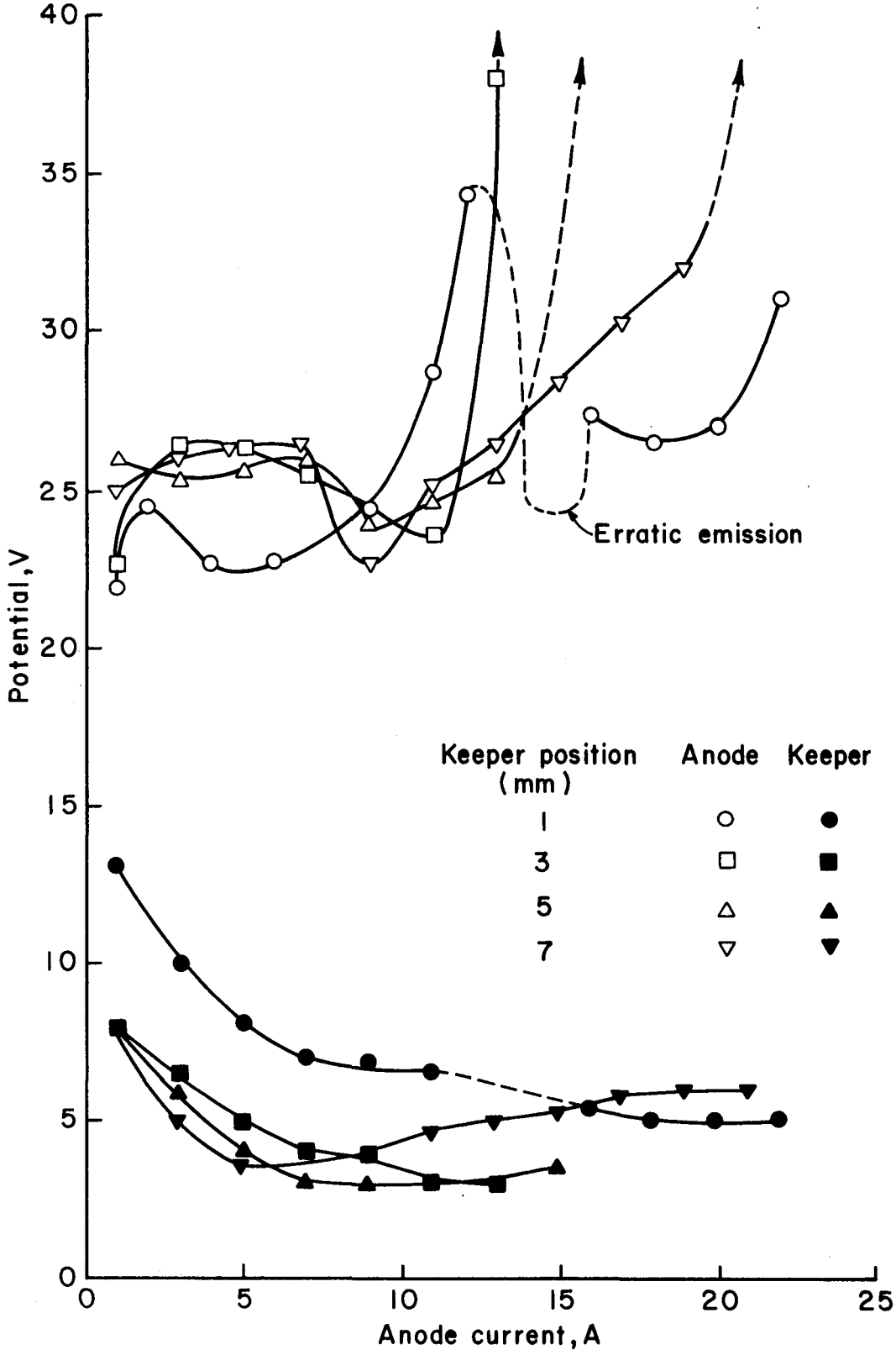

Fig. A-18. Hollow cathode/enclosed keeper performance. Configuration: see Fig. A-11. Keeper aperture: 3 mm. Ar flow: 800 mA. Cathode temperature: 950°C at 1 A, to 1220°C at 19 A.

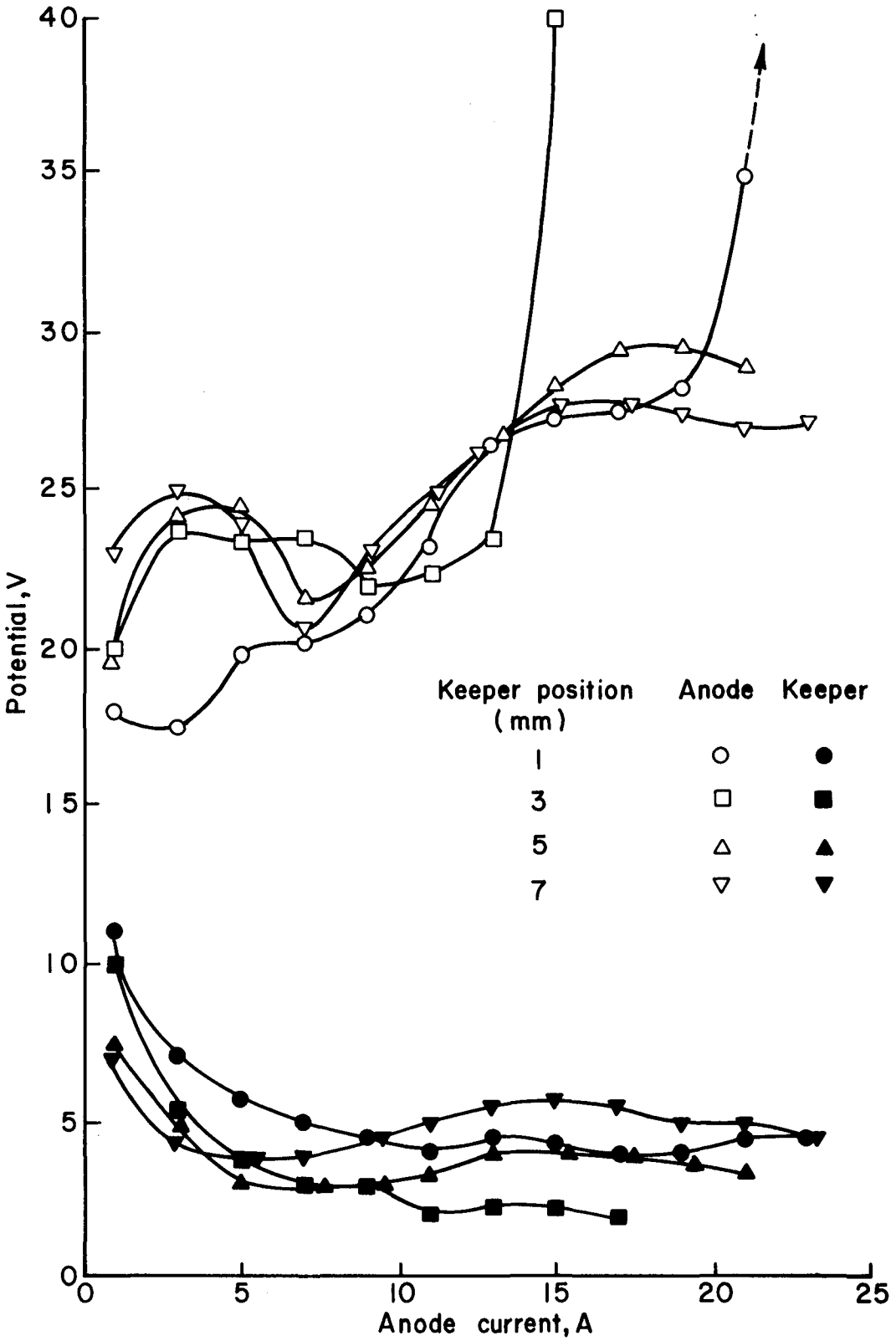

Fig. A-19. Hollow cathode/enclosed keeper performance. Configuration: see Fig. A-11. Keeper aperture: 3 mm. Ar flow: 1000 mA. Cathode temperature: 940°C at 1 A, to 1260°C at 23 A.

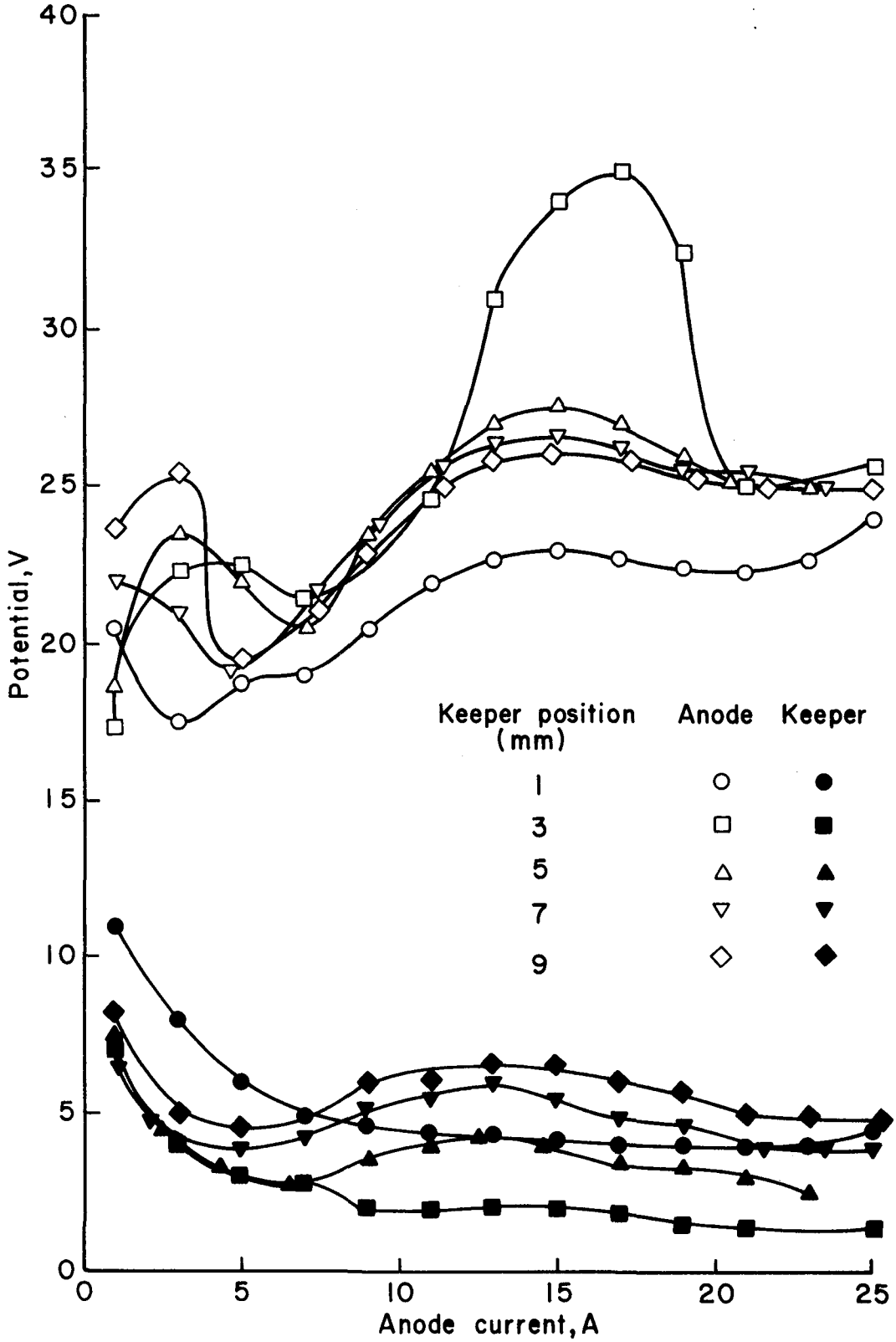

Fig. A-20. Hollow cathode/enclosed keeper performance. Configuration: see Fig. A-11. Keeper aperture: 3 mm. Ar flow: 1200 mA. Cathode temperature: 925°C at 1 A, to 1235°C at 25 A.

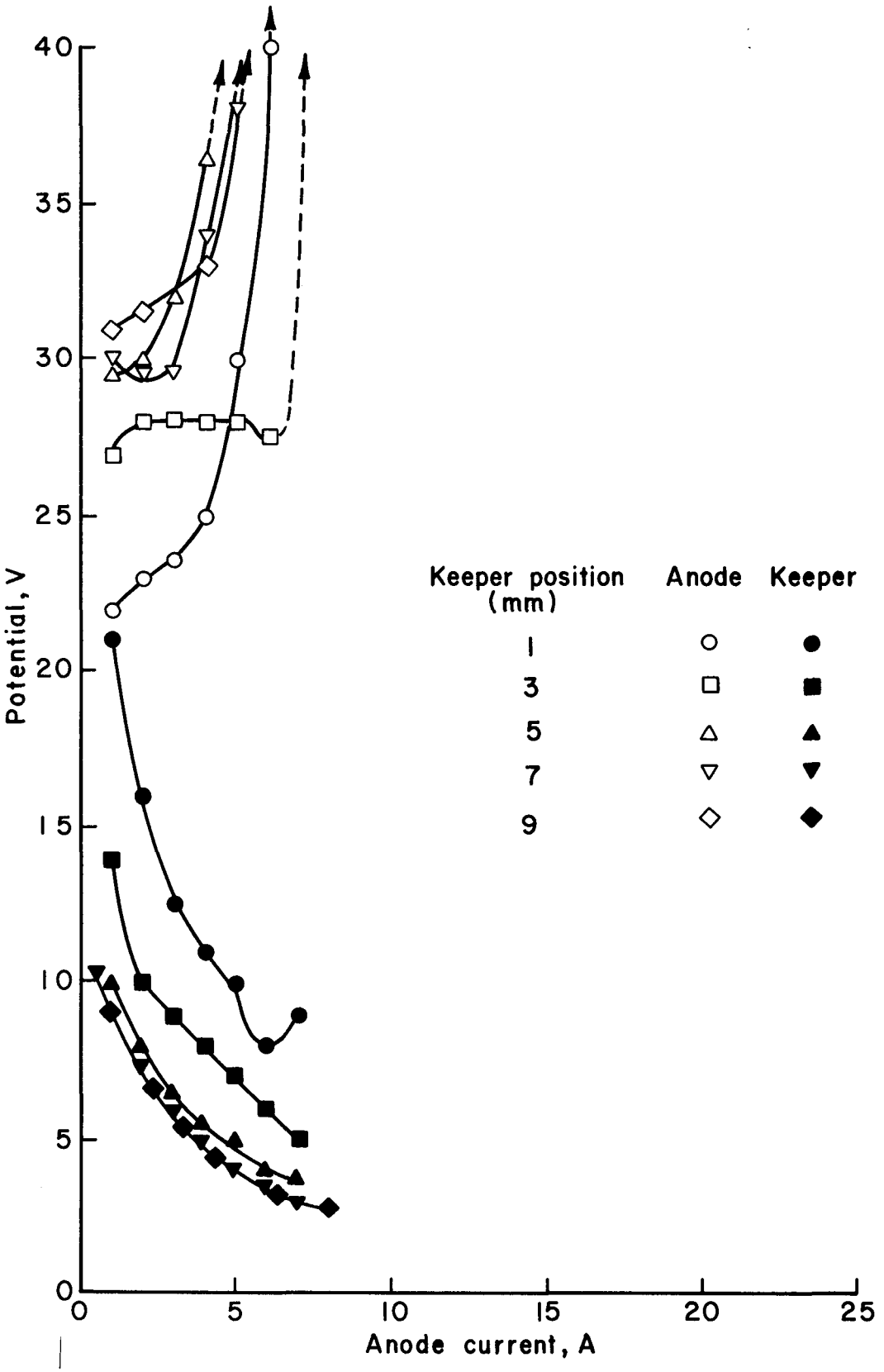

Fig. A-21. Hollow cathode/enclosed keeper performance. Configuration: see Fig. A-11. Keeper aperture: 4 mm. Ar flow: 400 mA. Cathode temperature: 930°C at 1 A, to 1025°C at 8 A.

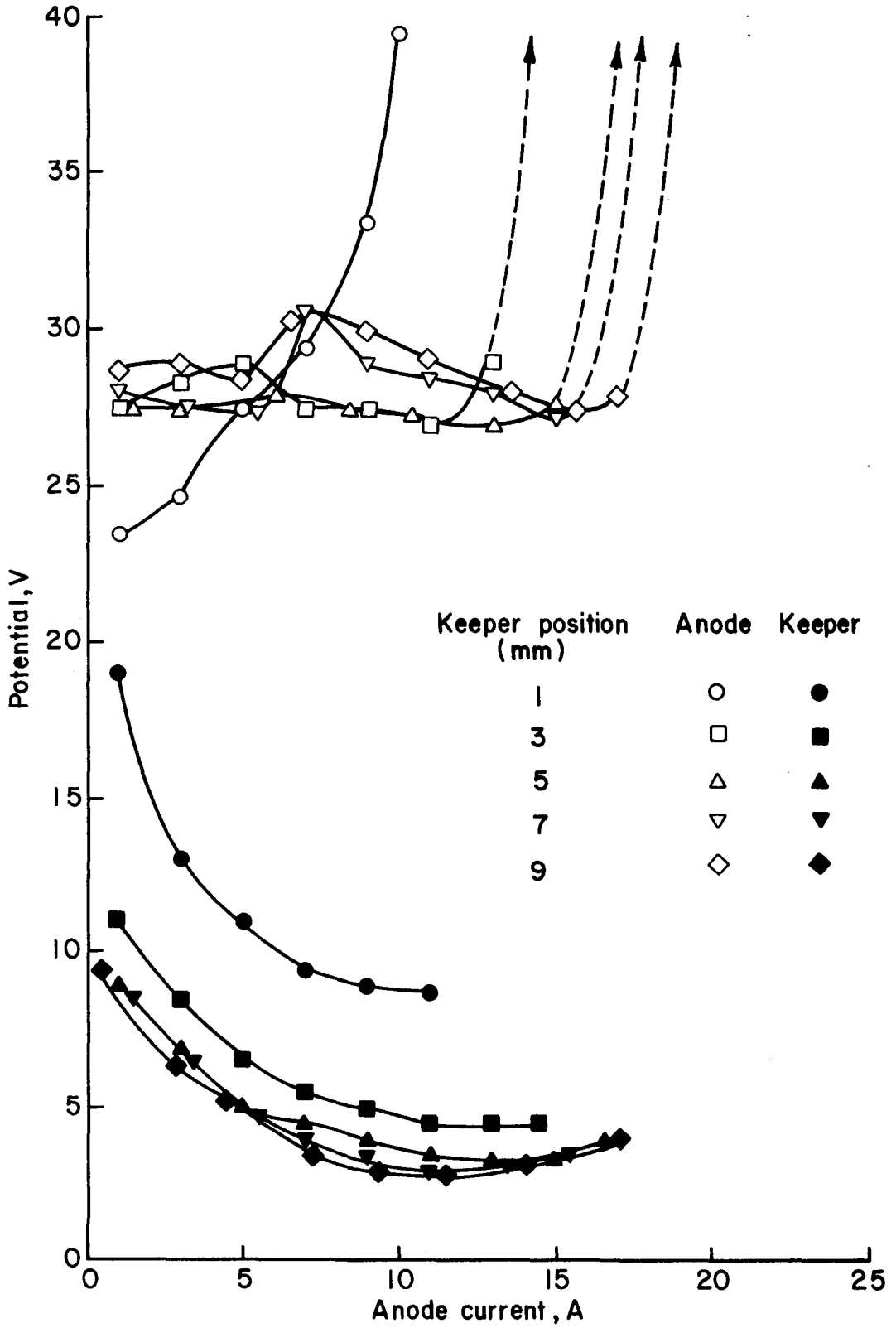

Fig. A-22. Hollow cathode/enclosed keeper performance. Configuration: see Fig. A-11. Keeper aperture: 4 mm. Ar flow: 600 mA. Cathode temperature: 950°C at 1 A, to 1190°C at 17 A.

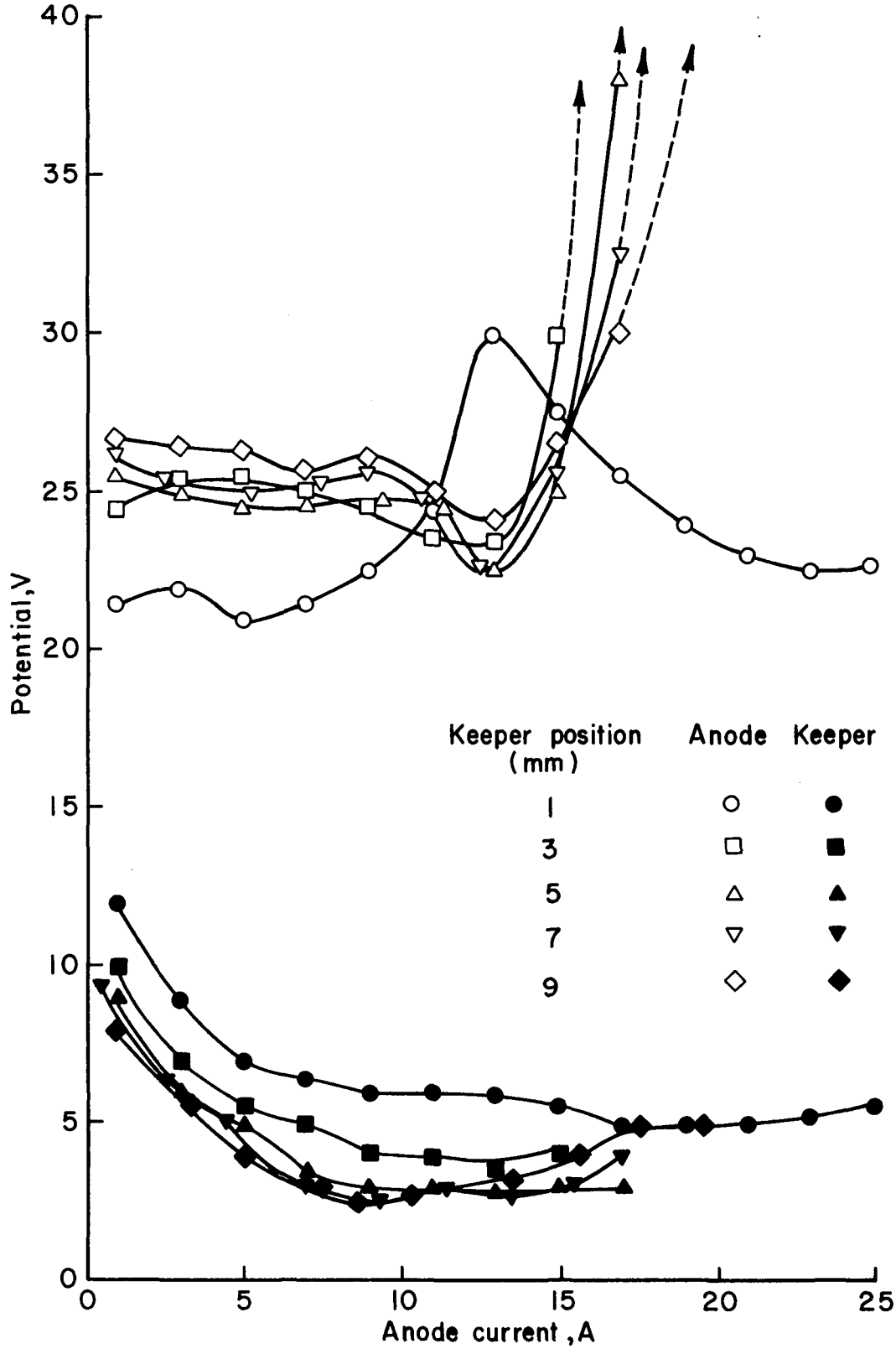

Fig. A-23. Hollow cathode/enclosed keeper performance. Configuration: see Fig. A-11. Keeper aperture: 4 mm. Ar flow: 800 mA. Cathode temperature: 920°C at 1 A, to 1170°C at 25 A.

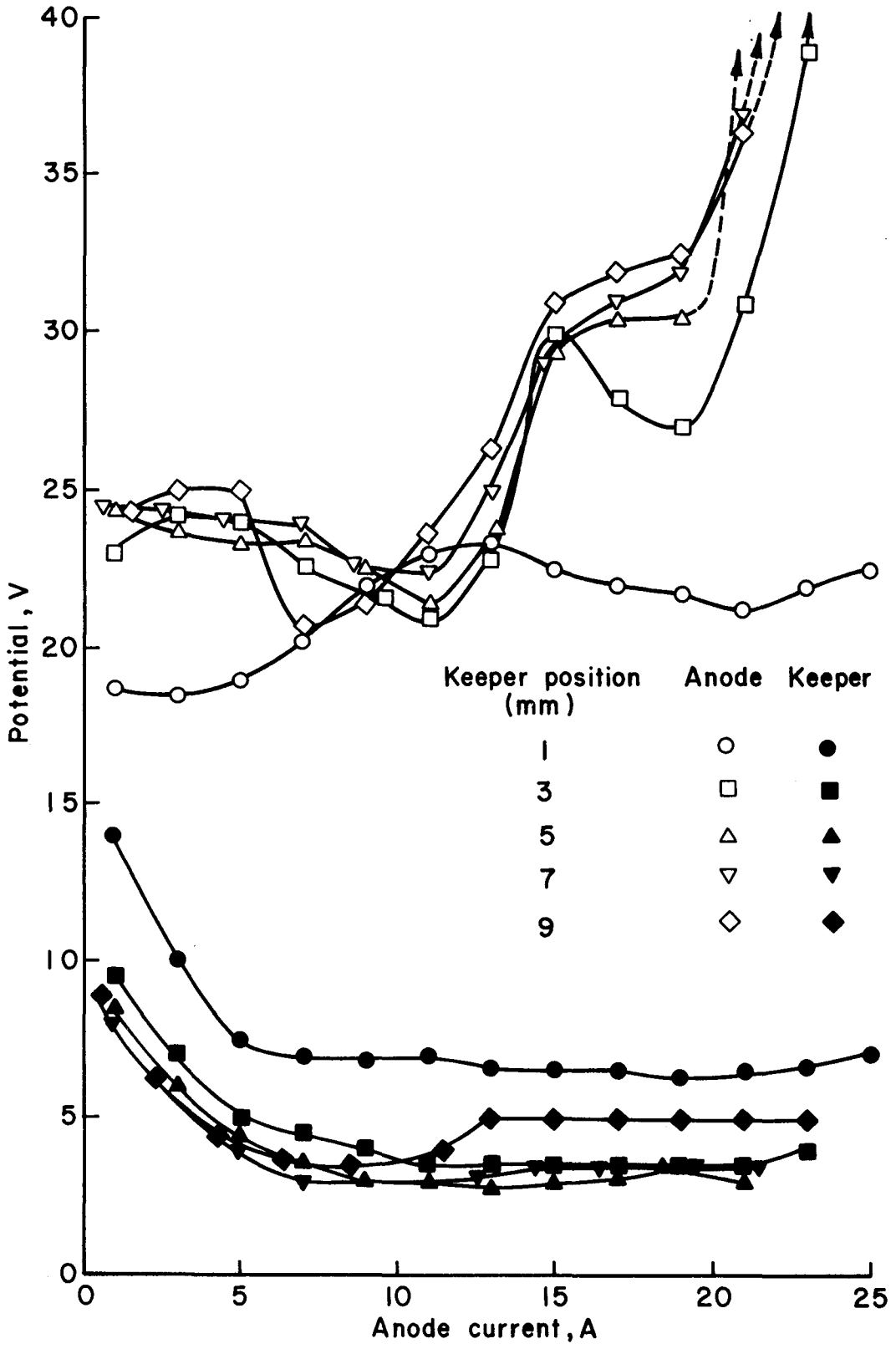

Fig. A-24. Hollow cathode/enclosed keeper performance. Configuration: see Fig. A-11. Keeper aperture: 4 mm. Ar flow: 1000 mA. Cathode temperature: 950°C at 1 A, to 1140°C at 25 A.

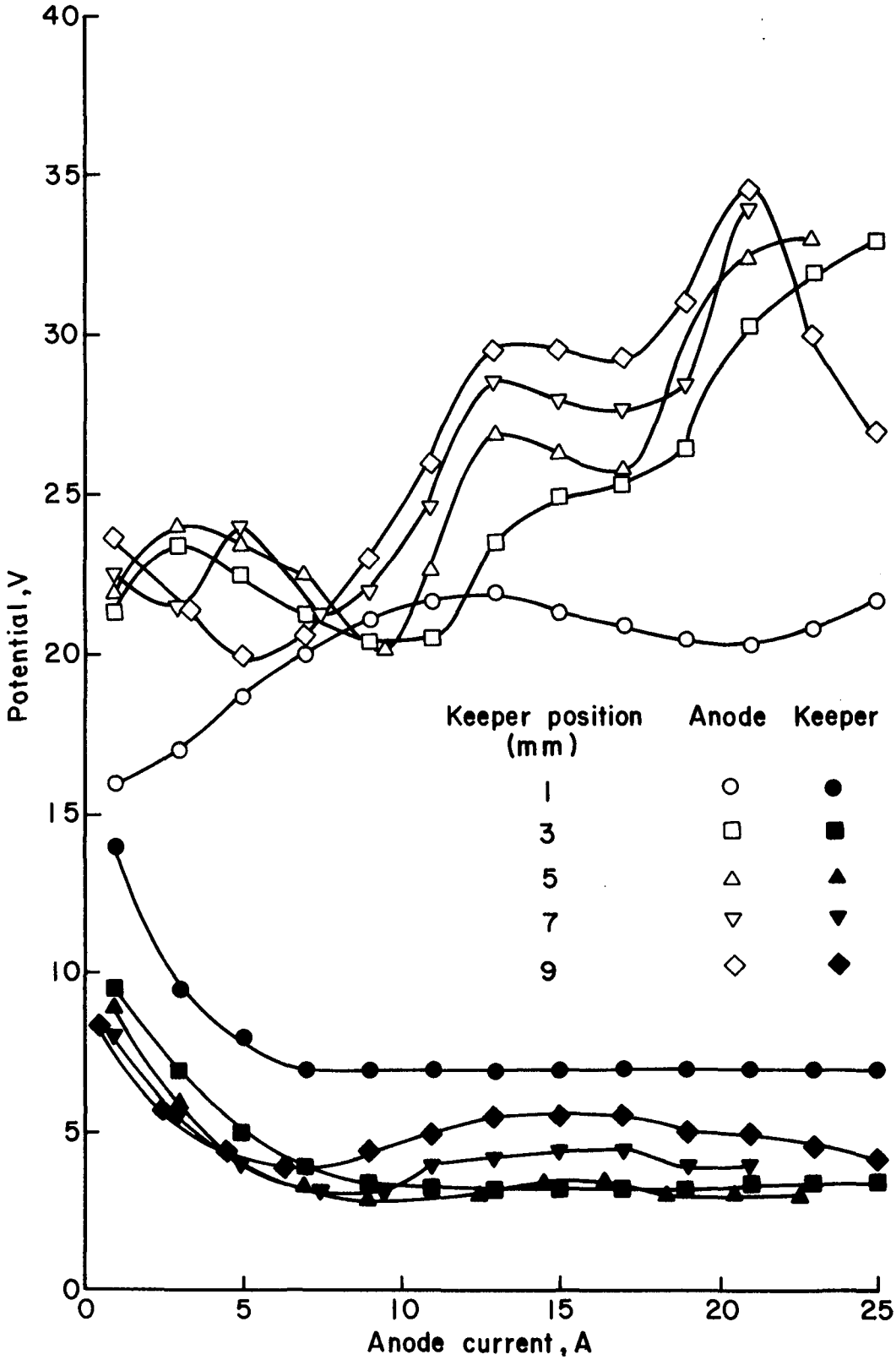

Fig. A-25. Hollow cathode/enclosed keeper performance. Configuration: see Fig. A-11. Keeper aperture: 4 mm. Ar flow: 1200 mA. Cathode temperature: 925°C at 1 A, to 1205°C at 25 A.

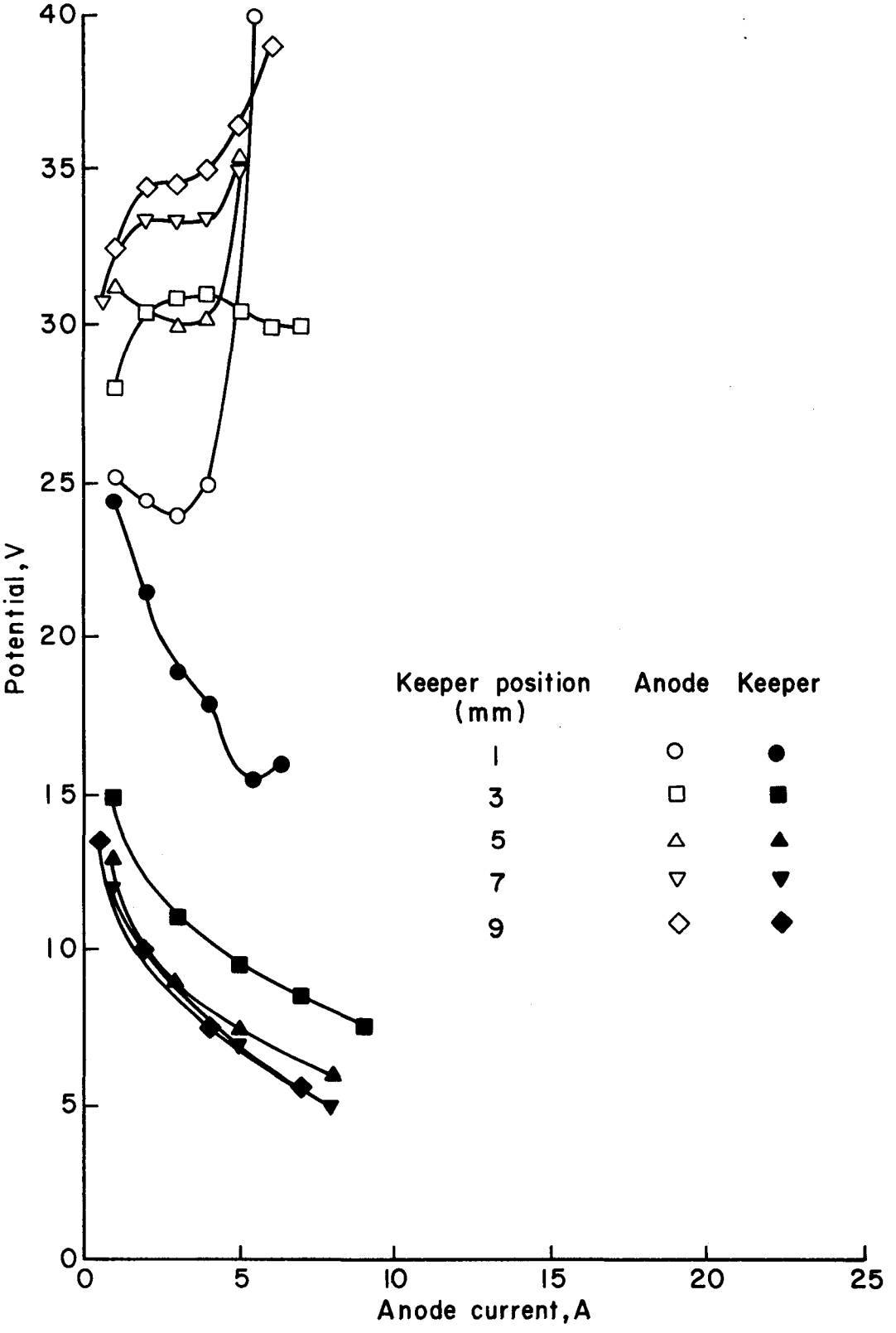

Fig. A-26. Hollow cathode/enclosed keeper performance. Configuration: see Fig. A-11. Keeper aperture: 5 mm. Ar flow: 400 mA. Cathode temperature: 925°C at 1 A, to 1025°C at 10 A.

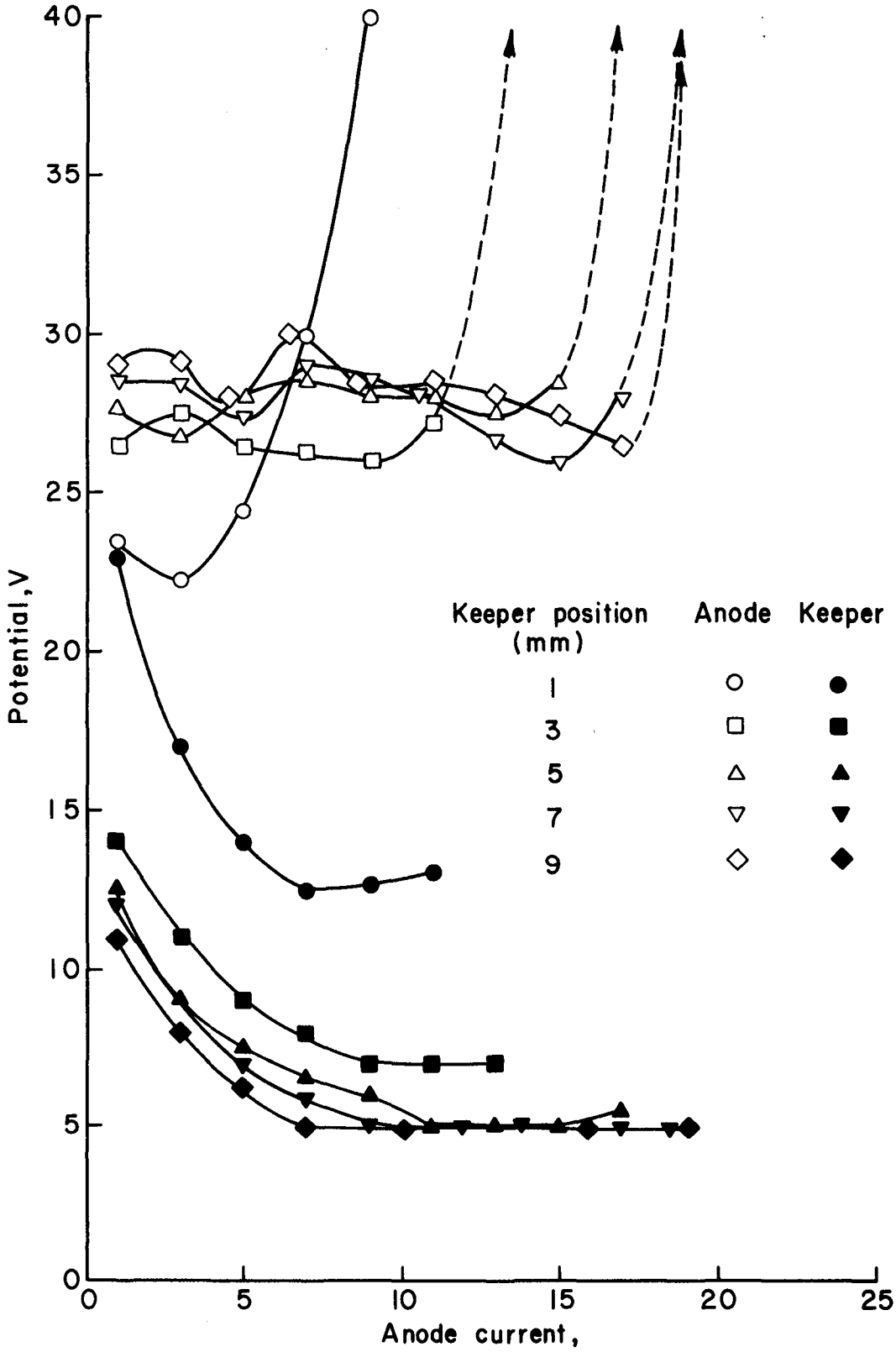

Fig. A-27. Hollow cathode/encolsed keeper performance. Configuration: see Fig. A-11. Keeper aperture: 5 mm. Ar flow: 600 mA. Cathode temperature: 920°C at 1 A, to 1075°C at 17 A.

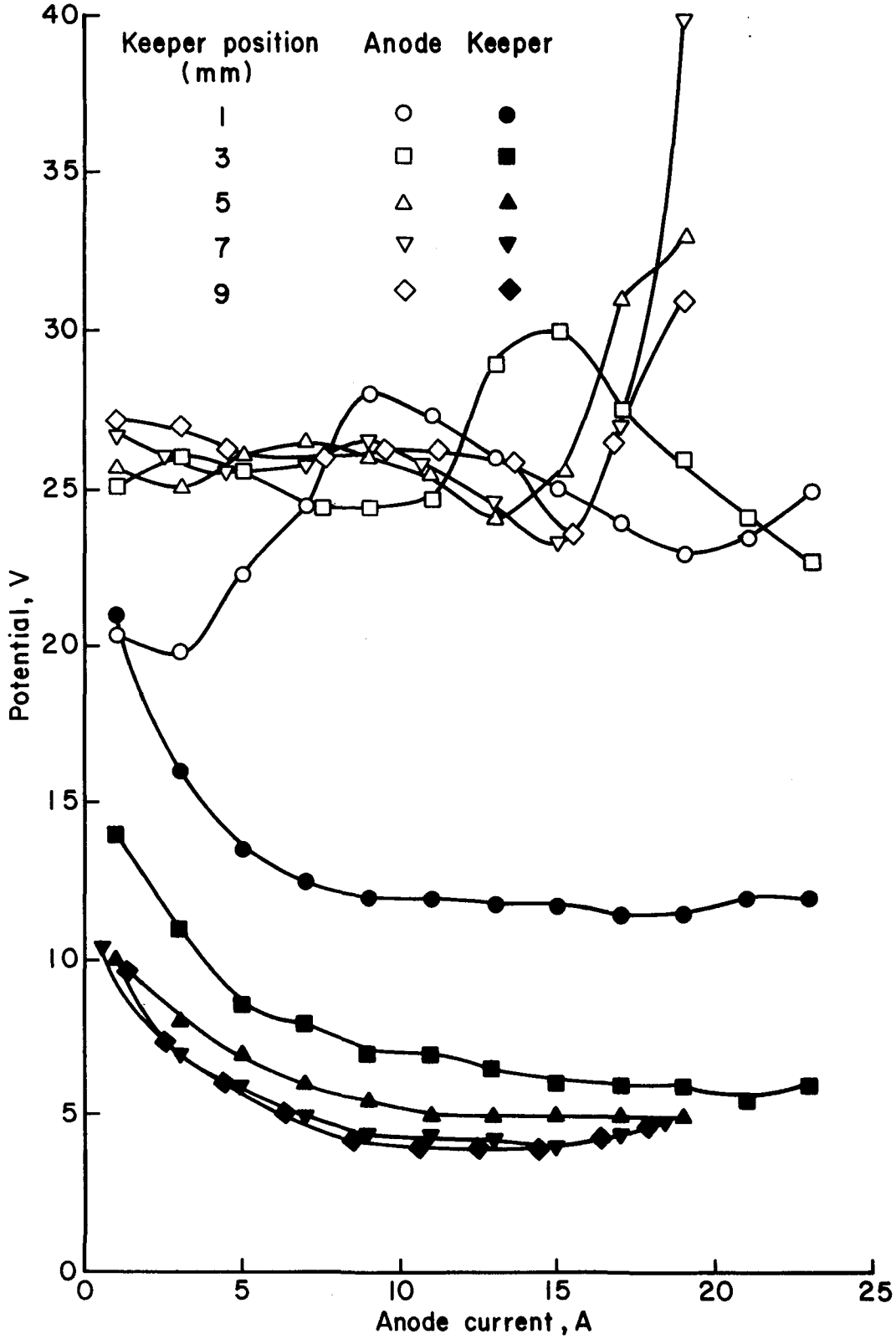

Fig. A-28. Hollow cathode/enclosed keeper performance. Configuration: see Fig. A-11. Keeper aperture: 5 mm. Ar flow: 800 mA. Cathode temperature: 930°C at 1 A, to 1200°C at 23 A.

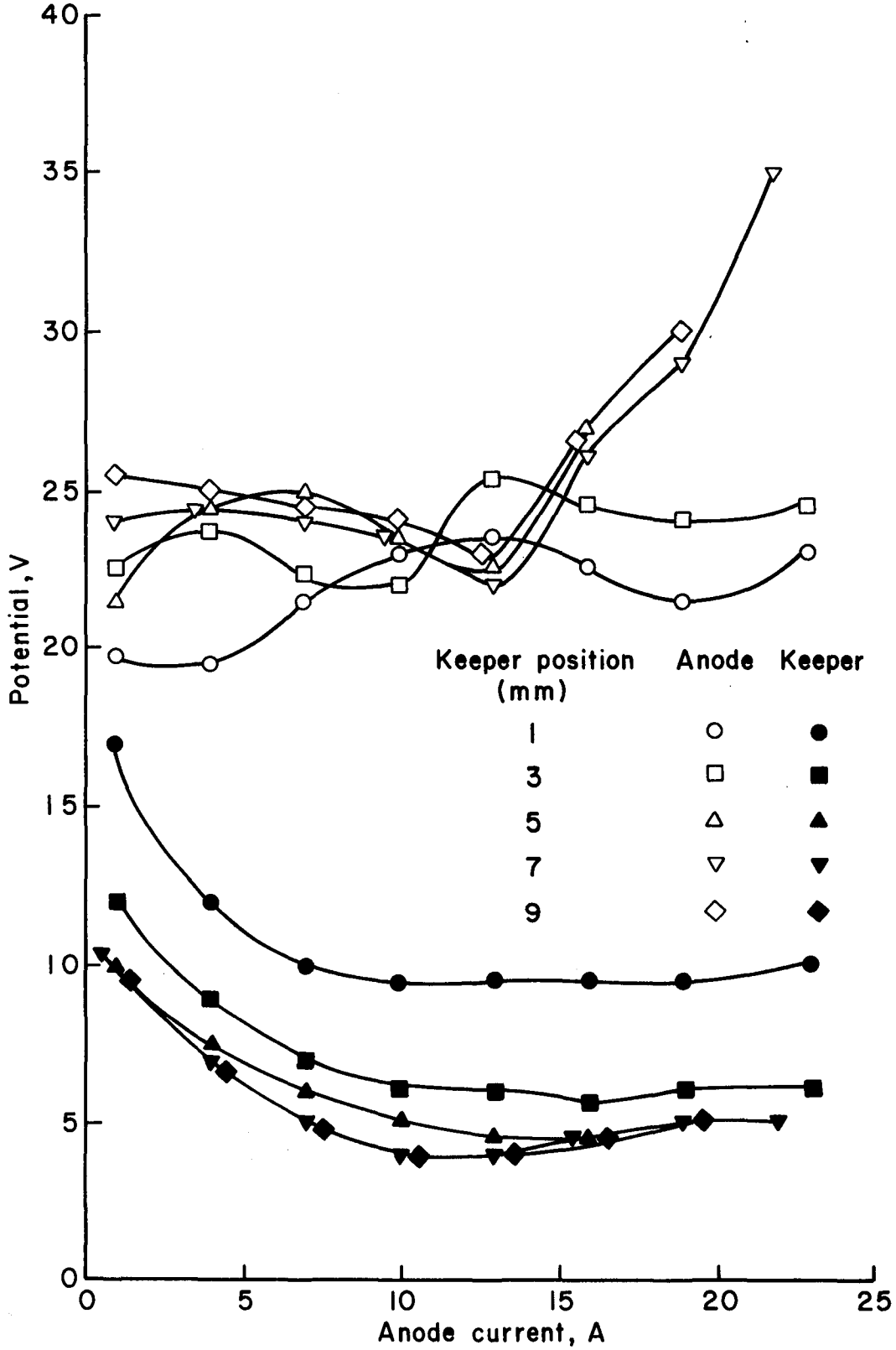

Fig. A-29. Hollow cathode/enclosed keeper performance. Configuration: see Fig. A-11. Keeper aperture: 5 mm. Ar flow: 1000 mA. Cathode temperature: 950°C at 1 A, to 1175°C at 23 A.

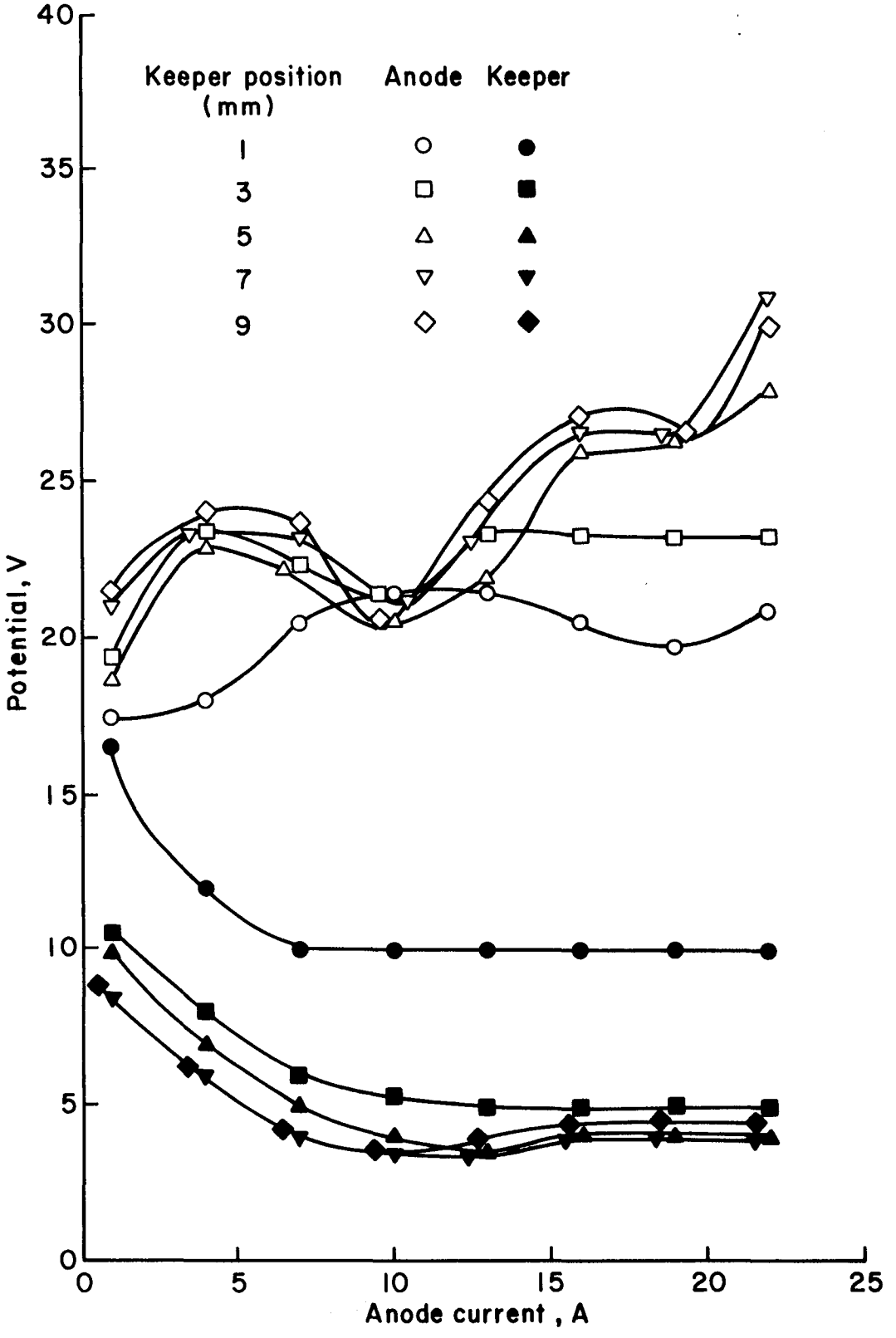

Fig. A-30. Hollow cathode/enclosed keeper performance. Configuration: see Fig. A-11. Keeper aperture: 5 mm. Ar flow: 1200 mA. Cathode temperature: 920°C at 1 A, to 1110°C at 22 A.

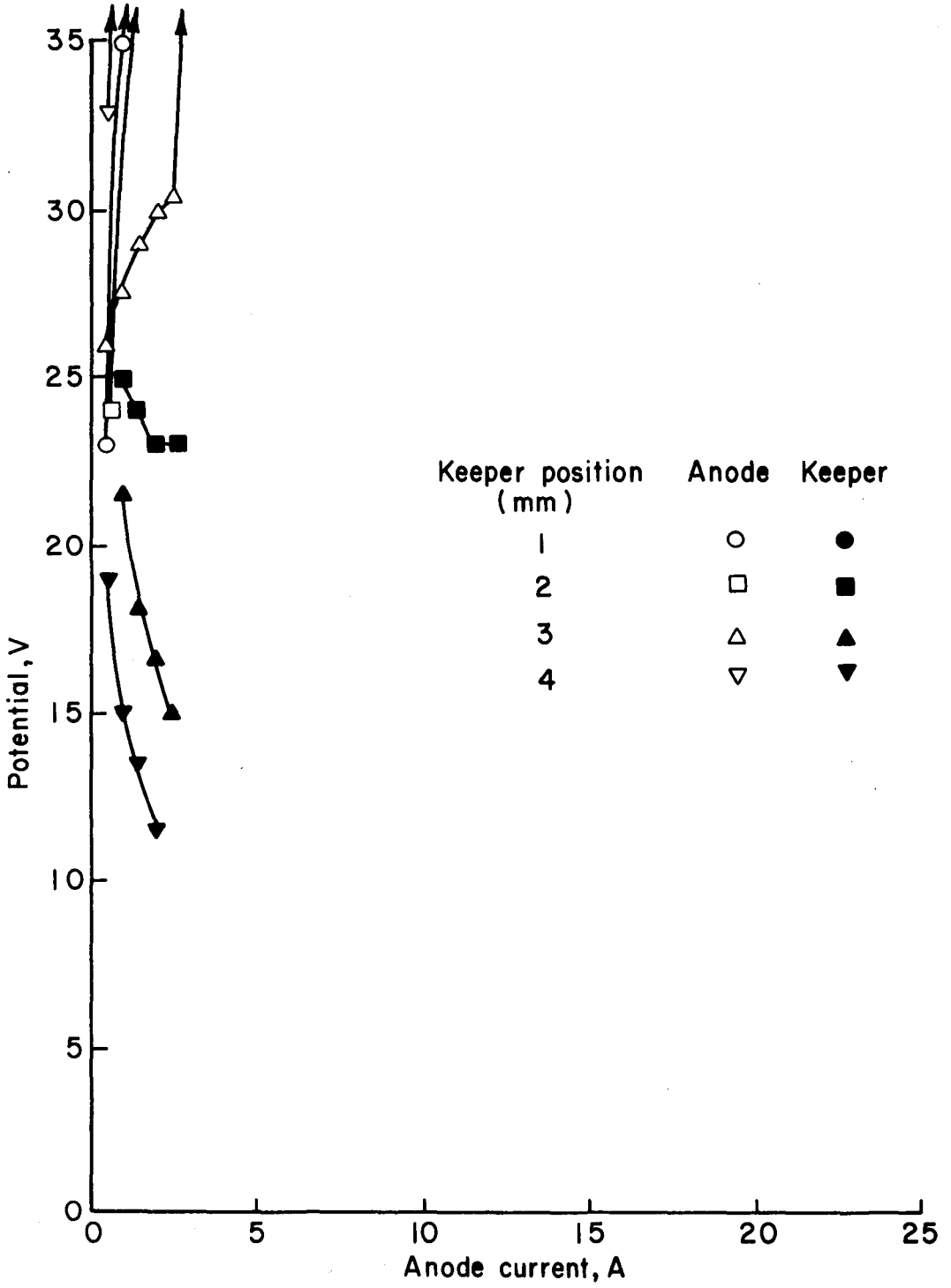

Fig. A-31. Hollow cathode/enclosed keeper performance. Configuration: see Fig. A-11. Keeper aperture: 6.35 mm. Ar flow: 200 mA. Cathode temperature: 1000°C at 1 A, to 1015°C at 2.5 A.

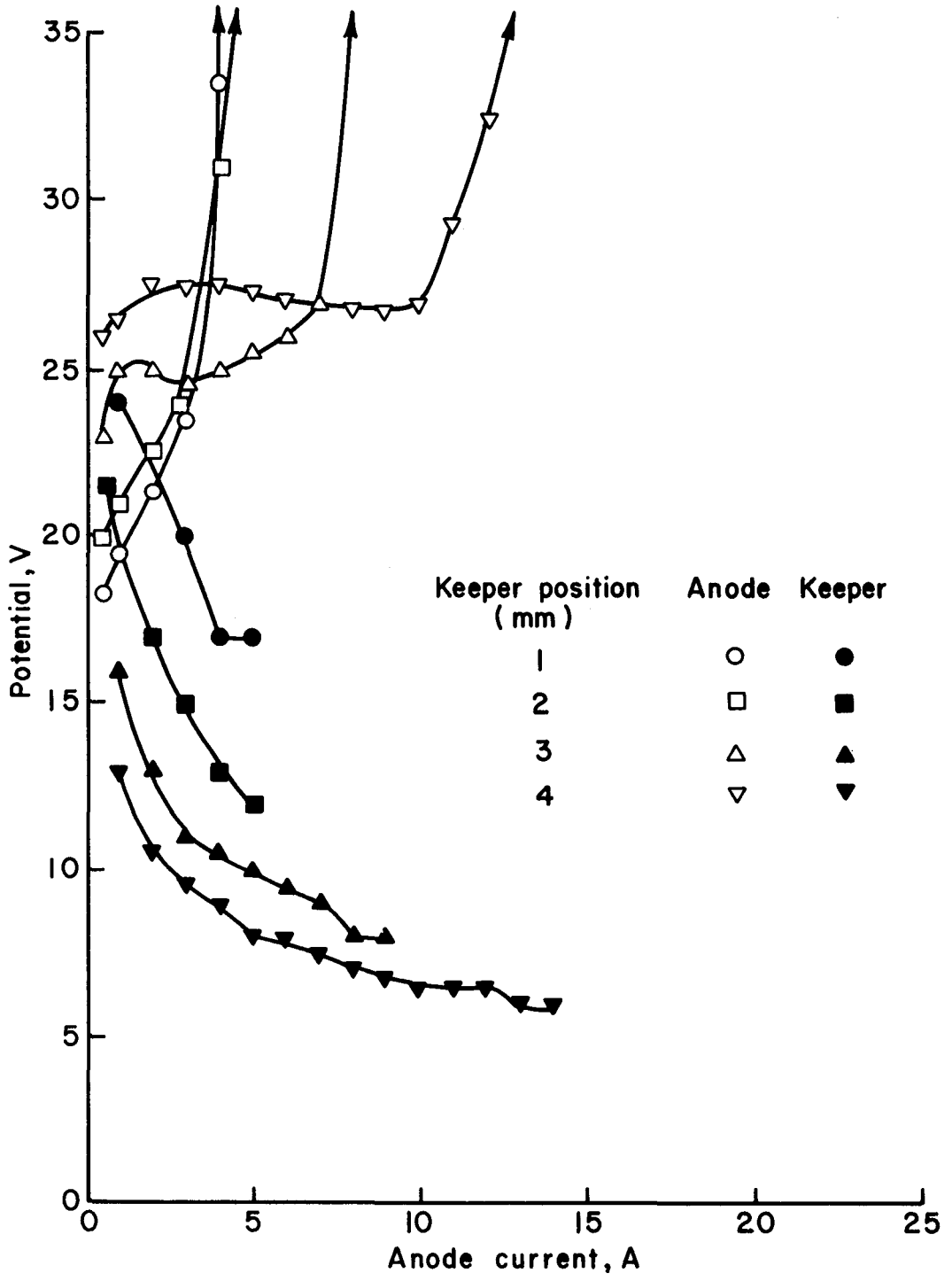

Fig. A-32. Hollow cathode/enclosed keeper performance. Configuration: see Fig. A-11. Keeper aperture: 6.35 mm. Ar flow: 400 mA. Cathode temperature: 990°C at 1 A, to 1150°C at 13 A.

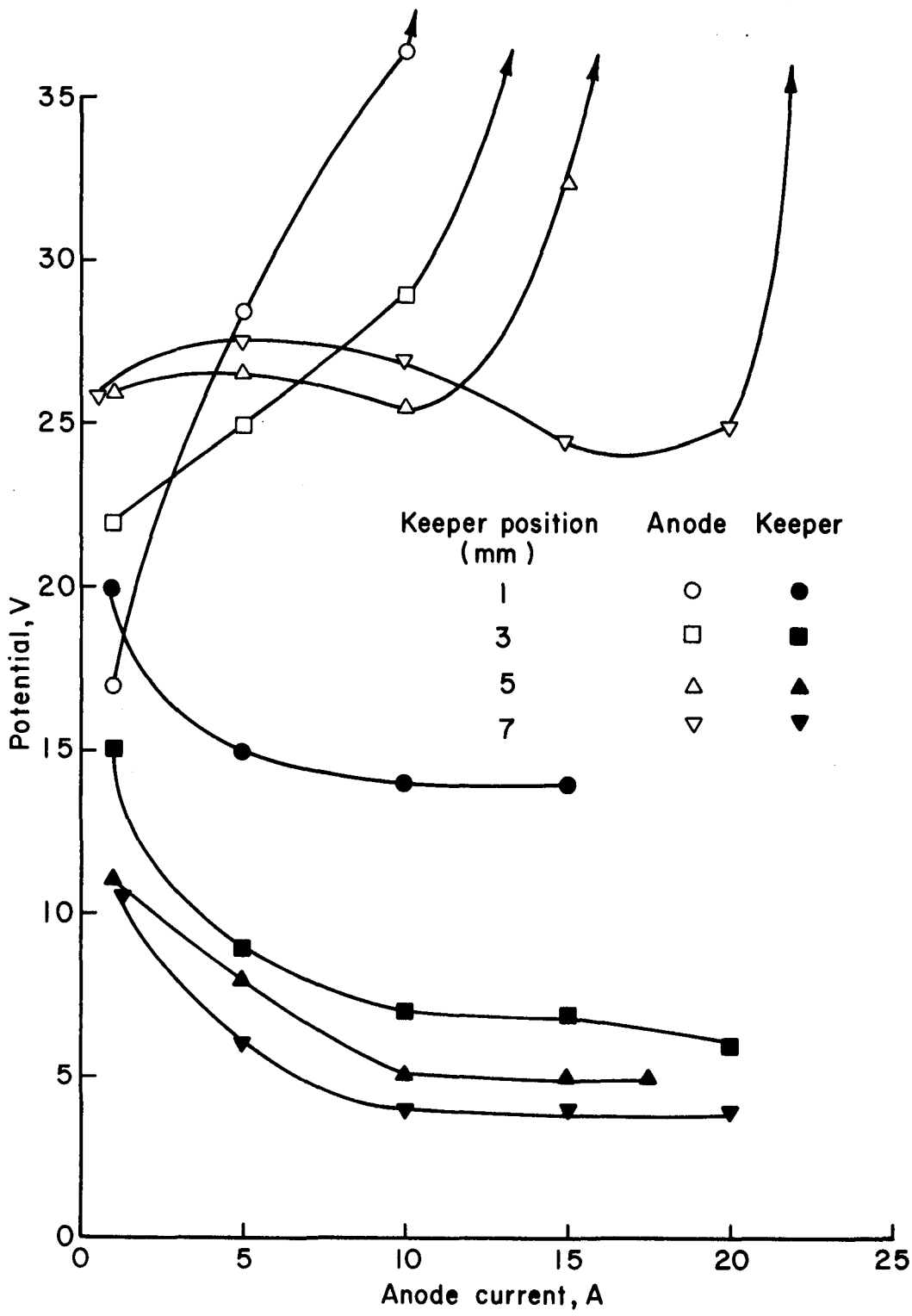

Fig. A-33. Hollow cathode/enclosed keeper performance. Configuration: see Fig. A-11. Keeper aperture: 6.35 mm. Ar flow: 600 mA. Cathode temperature: 975°C at 1 A, to 1050°C at 20 A.

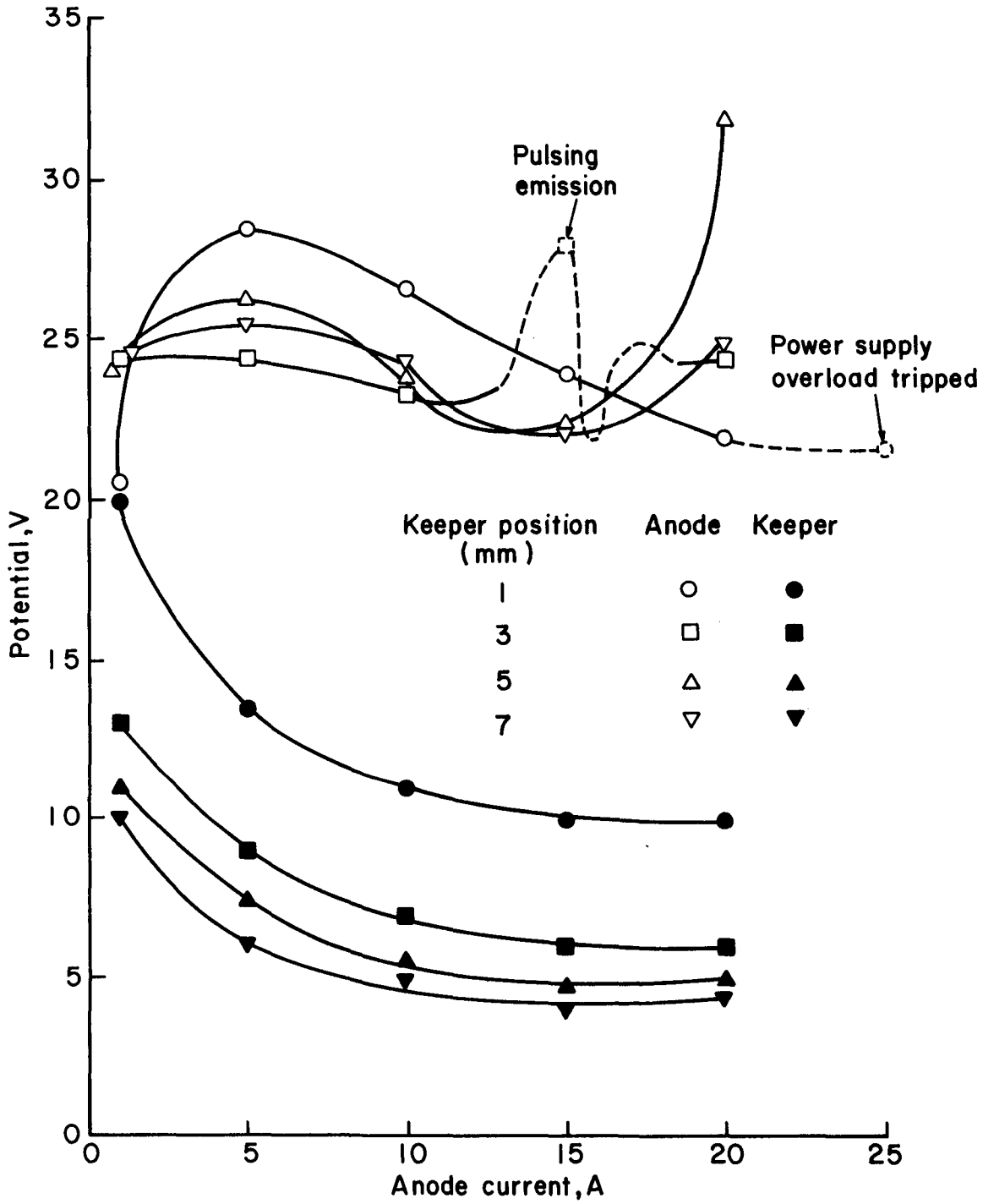

Fig. A-34. Hollow cathode/enclosed keeper performance. Configuration: see Fig. A-11. Keeper aperture: 6.35 mm. Ar flow: 800 mA. Cathode temperature: 965°C at 1 A, to 1050°C at 20 A.

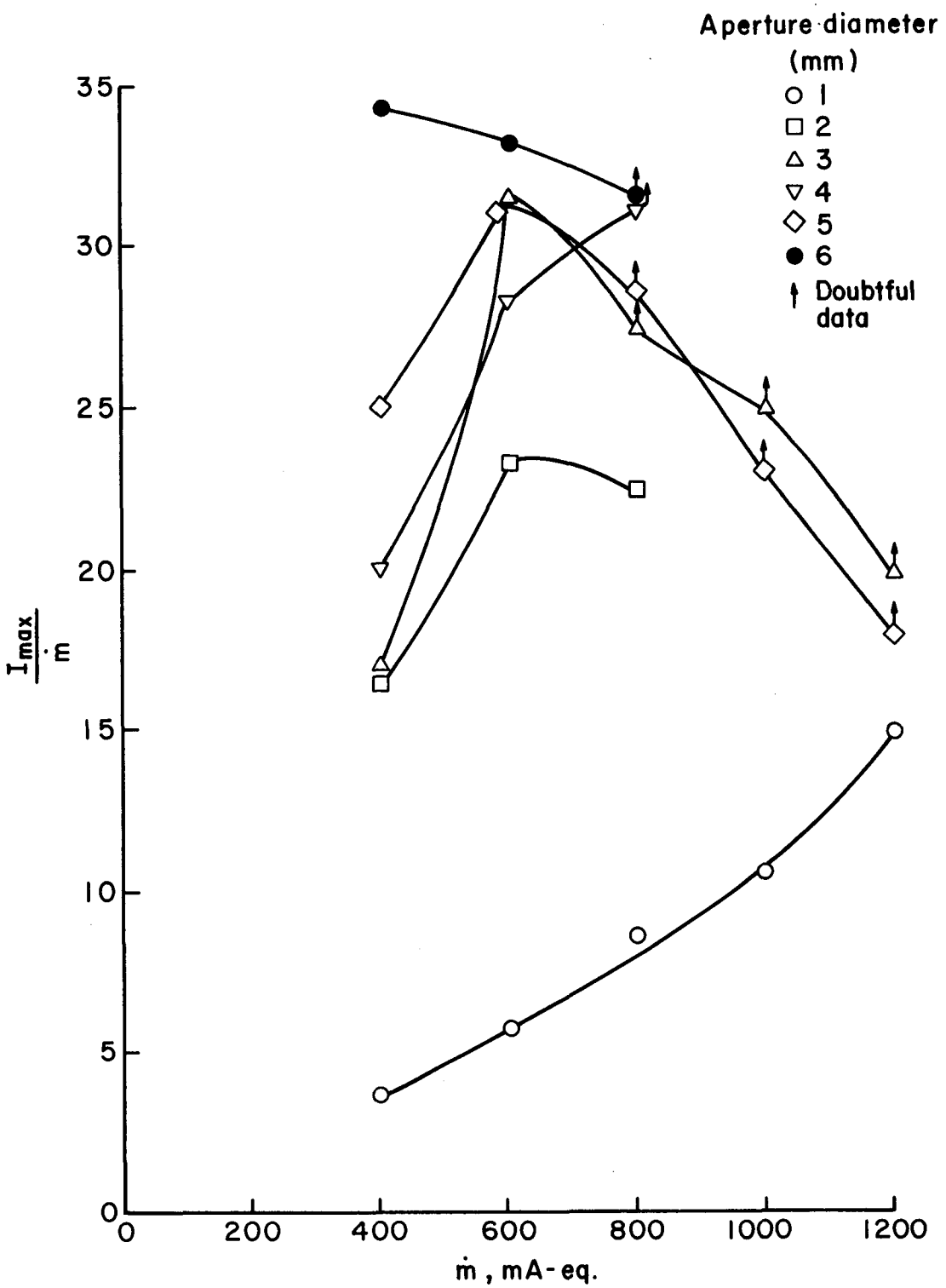

Fig. A-35. Hollow cathode/enclosed keeper performance in terms of emission ratio vs propellant flow for several keeper aperture sizes. For configuration see Fig. A-11. Data points with arrows were limited by the power supply current maximum and may have otherwise been higher.

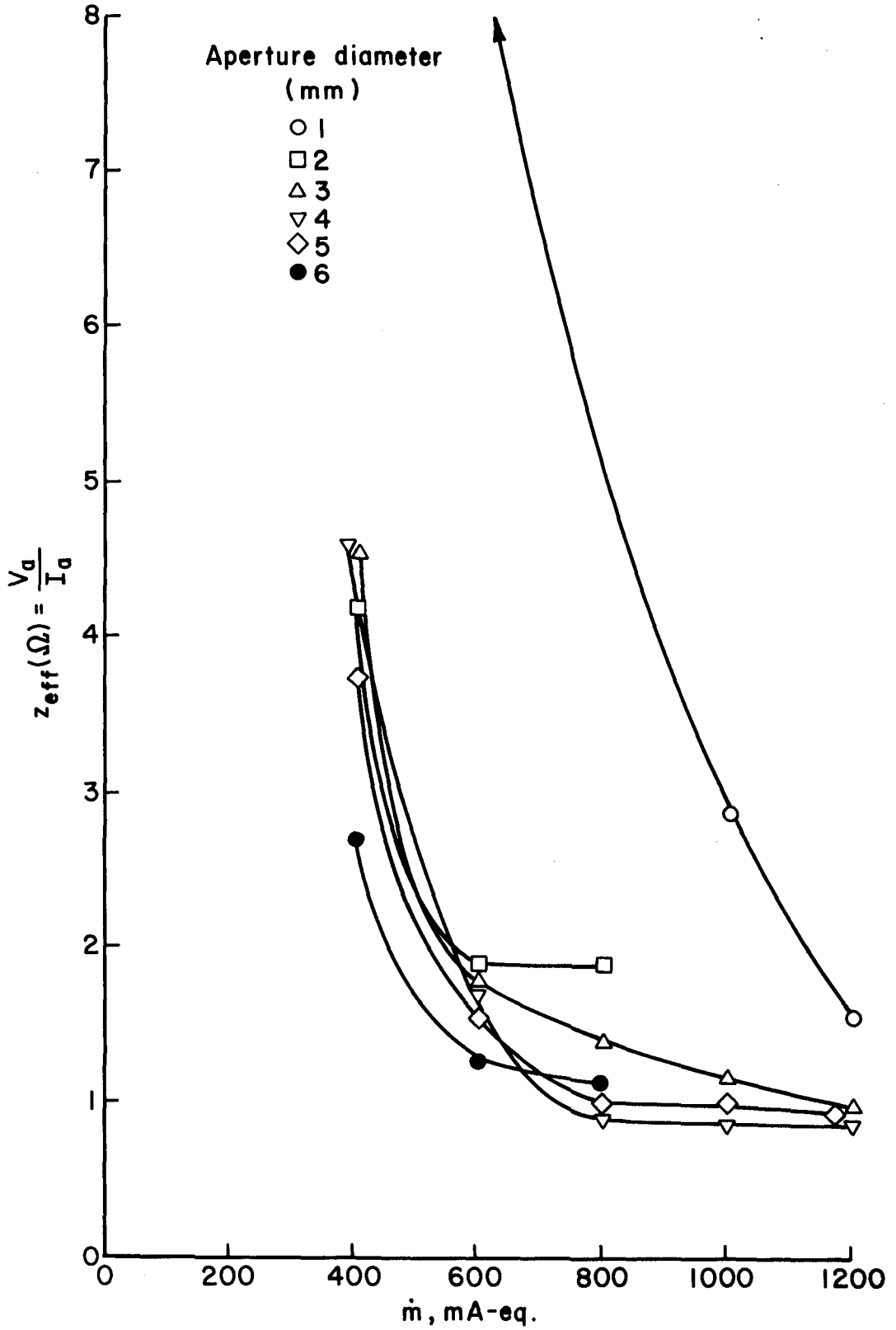

Fig. A-36. Hollow cathode/enclosed keeper performance presented as an effective impedance vs propellant flow for six keeper aperture sizes.

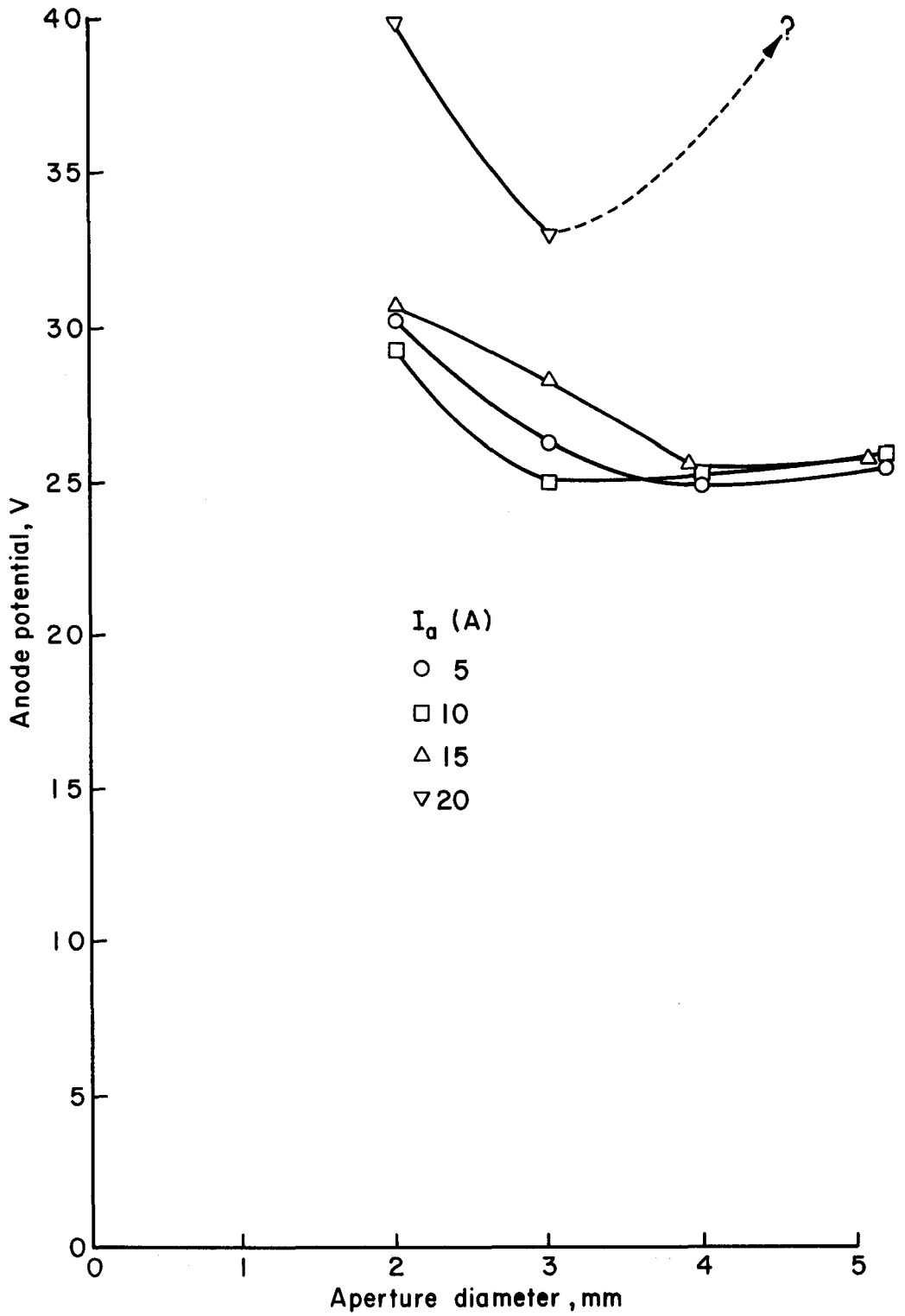

Fig. A-37. Hollow cathode/enclosed keeper performance defined as anode potential required to maintain a constant anode current as keeper aperture size is varied. Data taken at an Ar flow of 800 mA, and a keeper aperture position of 7 mm. For configuration see Fig. A-11. Dashed line indicates that 20 A could not be achieved under these conditions due to pulsing, erratic emission.

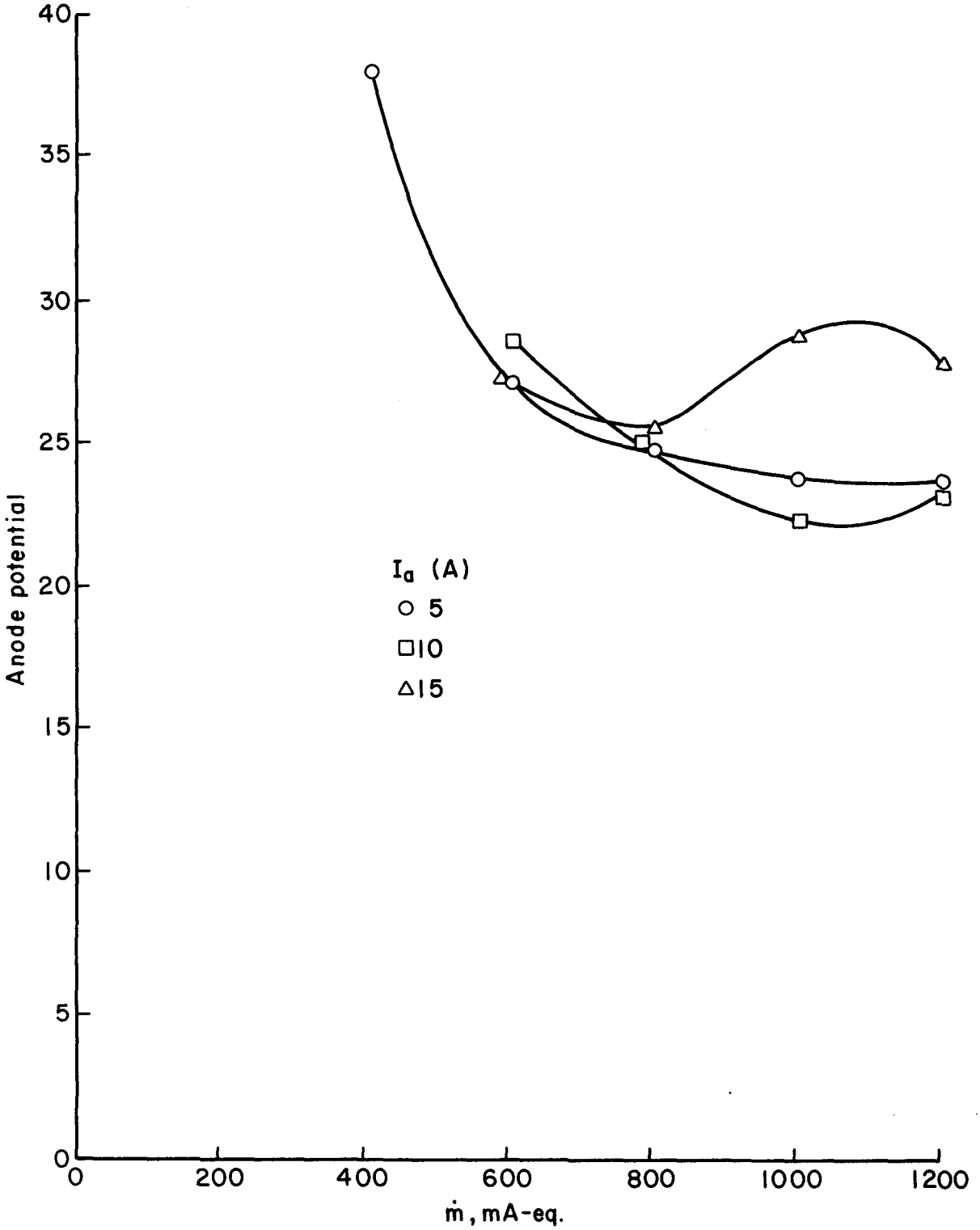

Fig. A-38. Hollow cathode/enclosed keeper performance defined as anode current required to maintain a constant anode current as Ar flow is varied. For test configuration see Fig. A-11. Keeper aperture: 4 mm. Keeper aperture position: 7 mm.

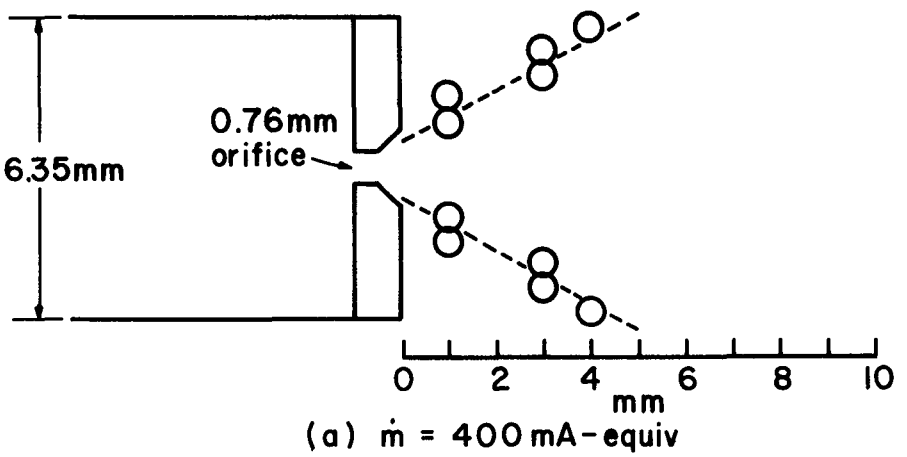

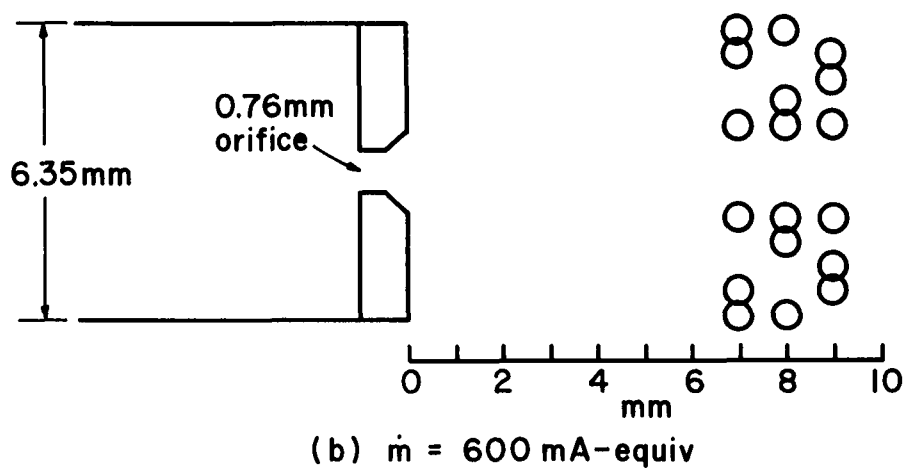

Fig. A-39. Plots of optimum enclosed keeper spacings for a range of keeper aperture diameters. Extracted from data presented on pages A-12 through A-34.

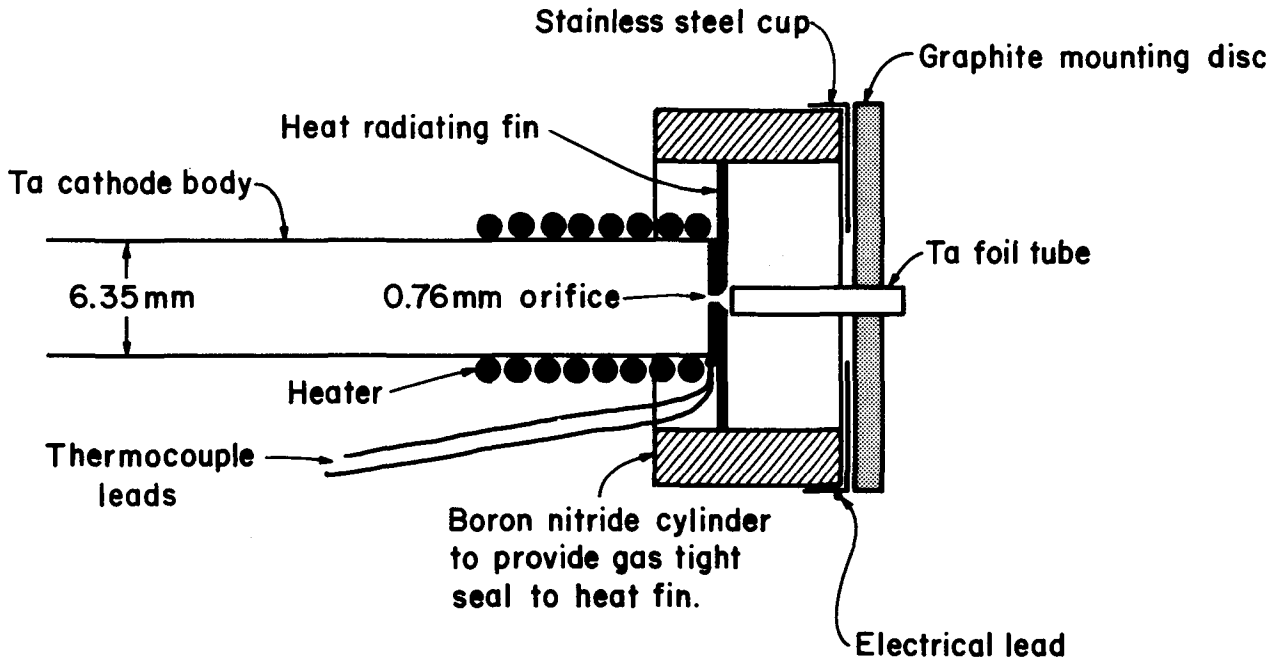

Fig. A-40. Hollow cathode with enclosed keeper. This is the same configuration as Fig. A-11 except that a Ta tube has replaced the Ta foil aperture. Data for various sized tubes are presented on pages following.

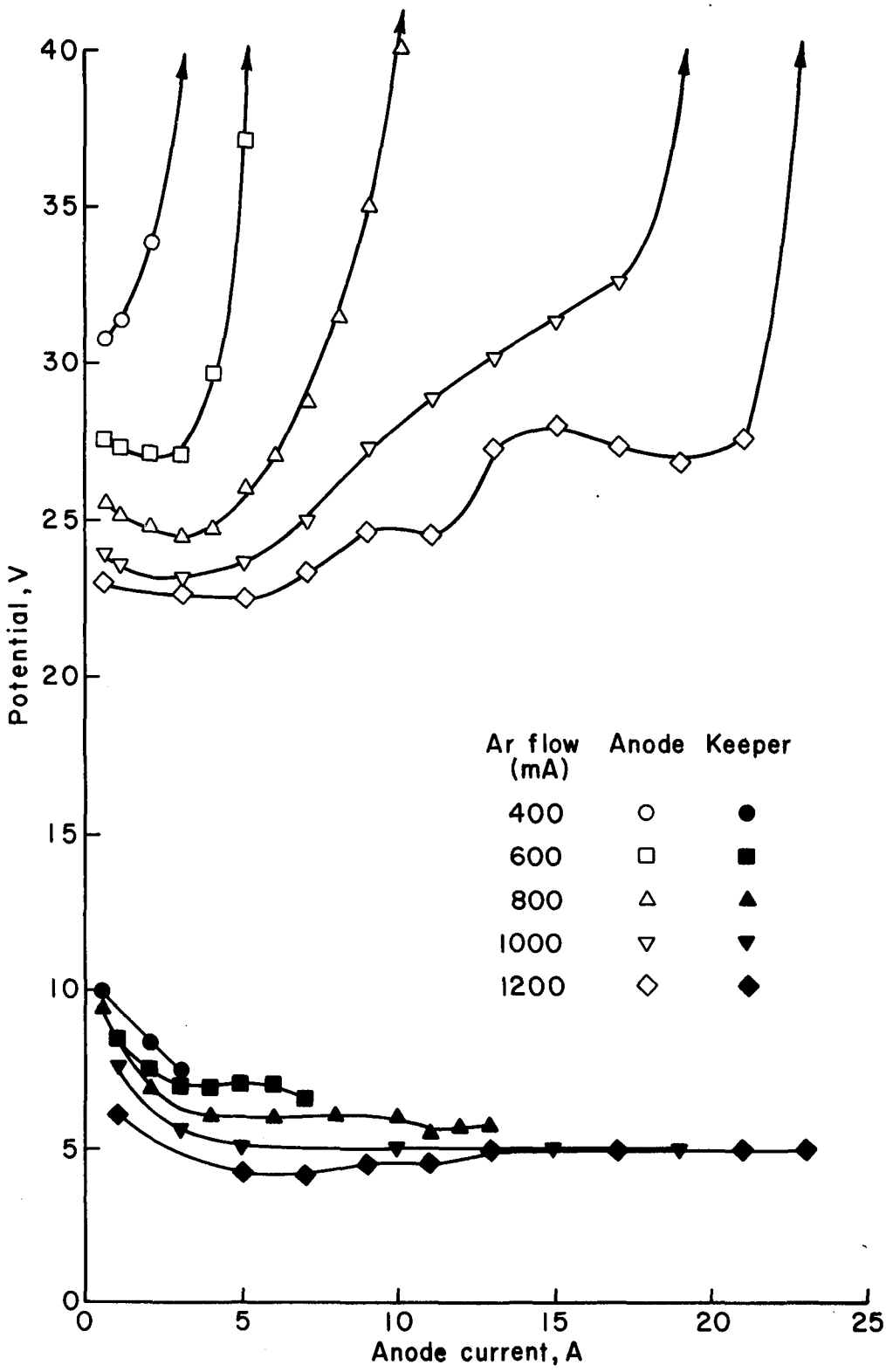

Fig. A-41. Hollow cathode/enclosed keeper with tubular aperture. Configuration: see Fig. A-40. Tubular aperture length: 10 mm. Tubular aperture diameter: 3 mm. Cathode temperature: 1000°C at 1 A, to 1130°C at 23 A.

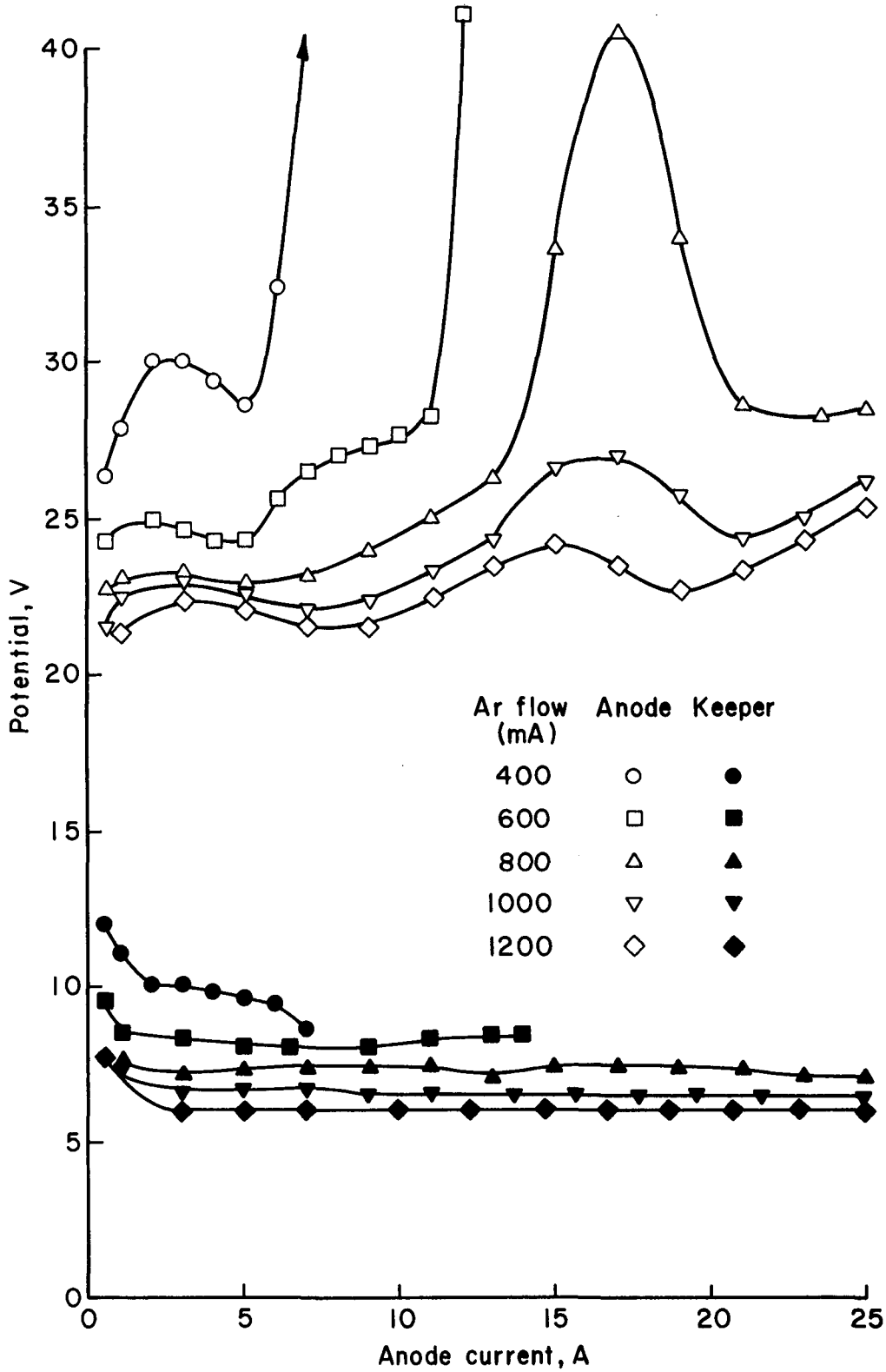

Fig. A-42. Hollow cathode/enclosed keeper with tubular aperture. Configuration: see Fig. A-40. Tubular aperture length: 10 mm. Tubular aperture diameter: 4 mm. Cathode temperature: 1000°C at 1 A, to 1150°C at 25 A.

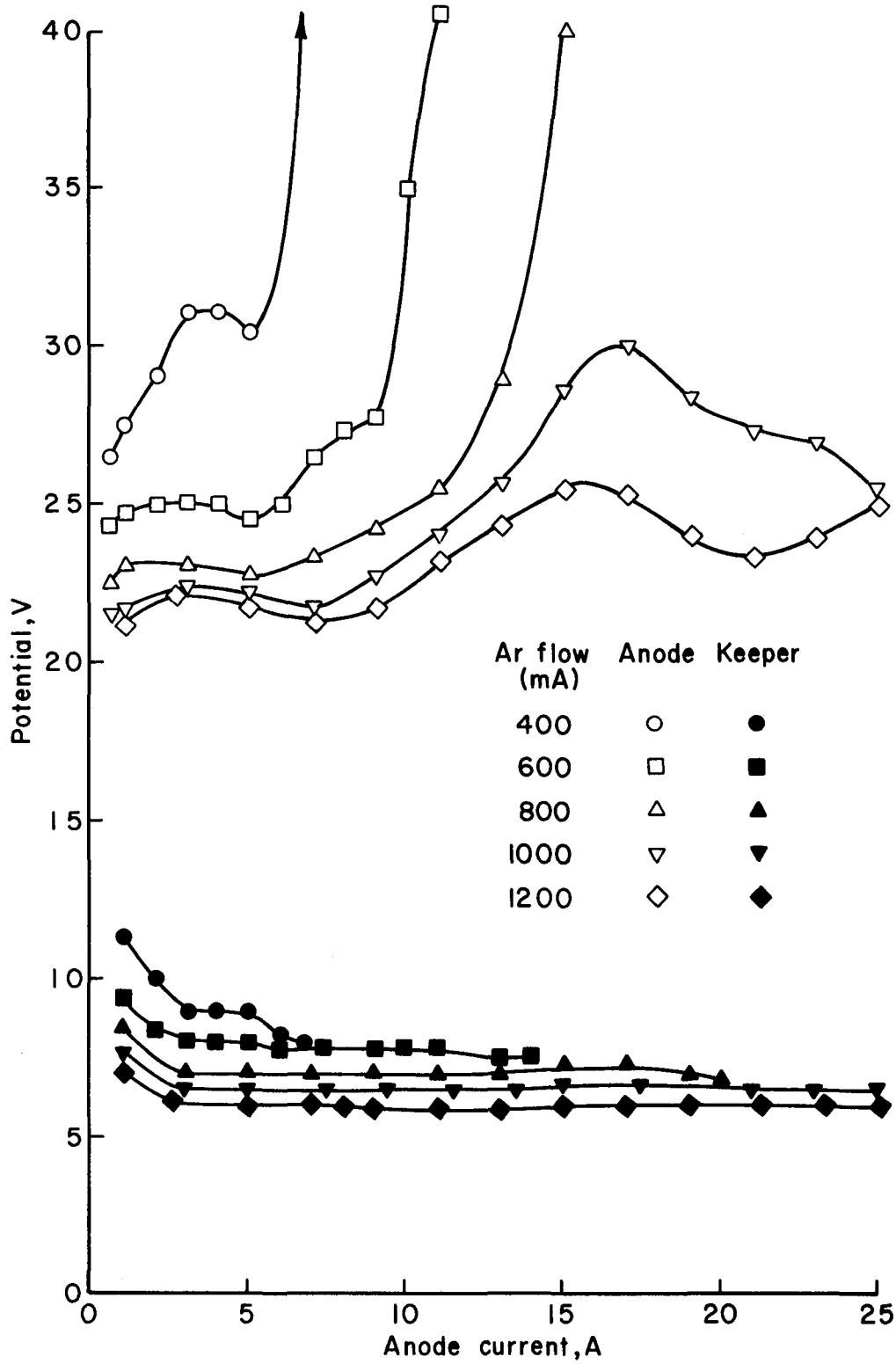

Fig. A-43. Hollow cathode/enclosed keeper with tubular aperture. Configuration: see Fig. A-40. Tubular aperture length: 10 mm. Tubular aperture diameter: 5 mm. Cathode temperature: 1000°C at 1 A, to 1130°C at 25 A.

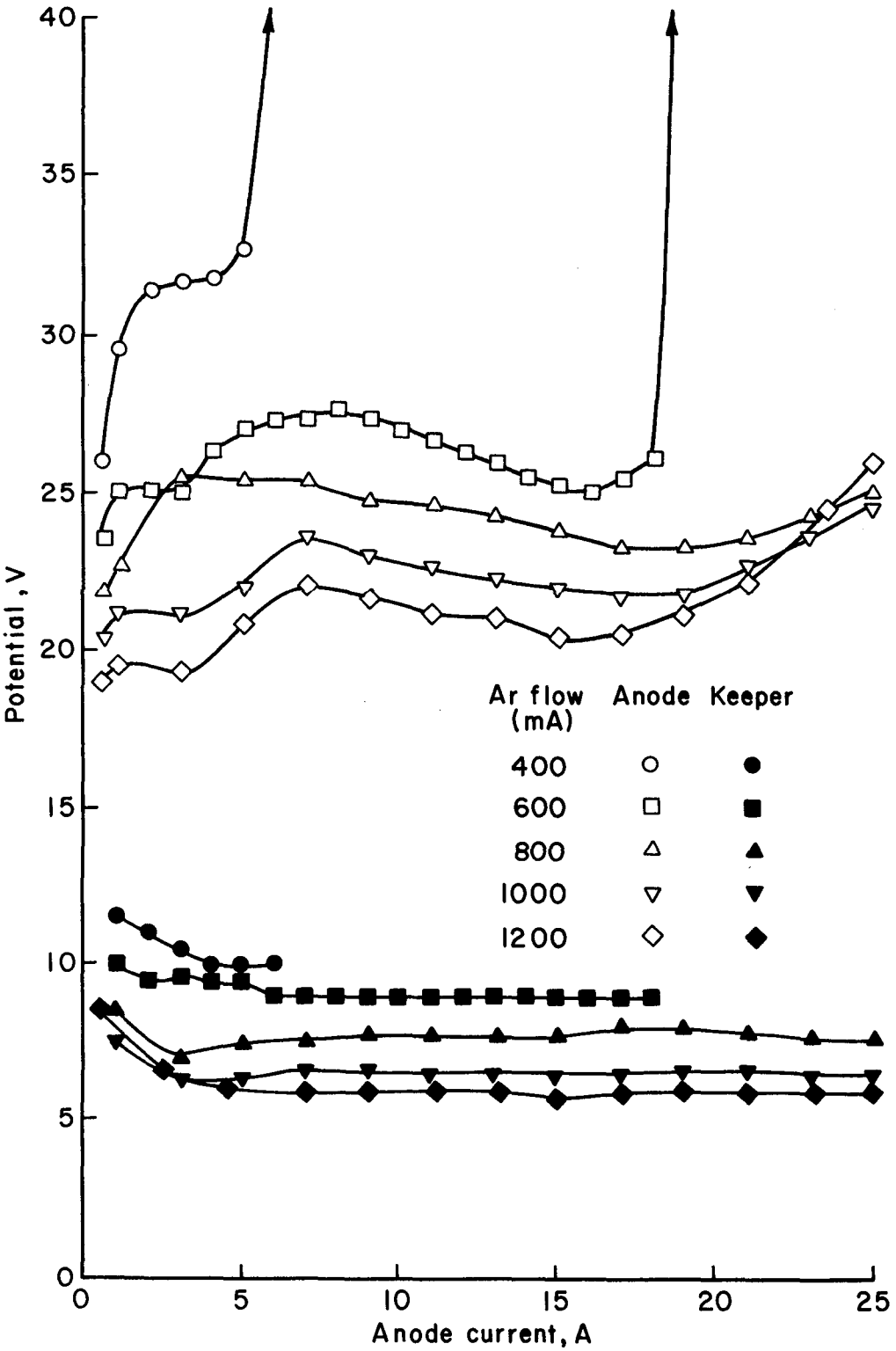

Fig. A-44. Hollow cathode/enclosed keeper with tubular aperture. Configuration: see Fig. A-40. Tubular aperture length: 7 mm. Tubular aperture diameter: 5 mm. Cathode temperature: 1000°C at 1 A, to 1080°C at 25 A.

APPENDIX B

PRODUCTION OF DOUBLY CHARGED IONS

by Gregory M. Plank

Under the proper conditions, the single step production of doubly charged ions can be significant. To aid in the evaluation of this single step contribution, a double ion parameter is derived herein. This parameter is similar to one derived earlier, but includes both single and double-step production of double ions from primary electrons. The earlier parameter included only the contribution due to double-step production.[B1] In both this and the earlier derivations, double ion production from Maxwellian electrons is assumed negligible. The basis for this assumption is the general tendency towards lower Maxwellian electron temperatures in larger thruster sizes, where prediction of large thruster performance is the primary motivation for this study.

The basic equation from which the derivation starts is[B1]

$$\frac{n_{++}}{n_+} = \frac{\Omega_p}{A_p} F_{++} \frac{n_p[P_+^{++}+(n_o/n_+)P_o^{++}] + n_m[Q_+^{++}+(n_o/n_+)Q_o^{++}]}{[2T_m(e/m_i)(1+n_p/n_m)]^{1/2}}, \qquad \text{(B1)}$$

where P_o^{++} and P_p^{++} are the rate factors for neutral atom to doubly charged ion and singly to doubly charged ion from primary electrons, Q_o^{++} and Q_+^{++} are the same rates from Maxwellian electrons, n_+ and n_{++} are the densities of singly and doubly charged ions, n_p and n_m are the densities of primary and Maxwellian electrons, n_o is the neutral atom density, e is the electronic charge, m_i is the ion mass, T_m is the Maxwellian electron temperature (in eV), Ω_p and A_p are the volume and

outside area of the primary electron region, and F_{++} is a geometrical factor for double ions.

Due to the assumed low value of Maxwellian electron temperature, the Q_o^{++} and Q_+^{++} processes can be ignored. Also, for normal operation, n_p is much smaller than n_m, so that n_p/n_m is negligible compared to unity. Dropping these terms, together with the substitution of

$$I^{++}/I^{+} = 2^{3/2} n_{++}/n_{+} \tag{B2}$$

gives

$$\frac{I^{++}}{I^{+}} = \frac{2\Omega_p F_{++}}{A_p} \frac{n_p [P_+^{++} + (n_o/n_+) P_o^{++}]}{(eT_m/m_i)^{1/2}} . \tag{B3}$$

From the production rate of singly charged ions and the free-molecular-flow of escaping neutrals, an expression for primary electron density can be obtained,[B1]

$$n_p = A_o A_p J_b \bar{v}_o / 4 A_s J_o P_o^{+} (1-\eta_u) \Omega_p , \tag{B4}$$

where A_o is the effective sharp-edged orifice escape area for neutrals, J_b is the beam current, $\bar{v}_o$ is the most probable neutral velocity, A_s is the screen extraction area for ions, J_o is the total neutral flow rate (in A-equiv), P_o^{+} is the rate factor for neutral to singly ionized, and η_u is the propellant utilization. With the substitution of Eq. (B4) into Eq. (B3),

$$\frac{I^{++}}{I_+} = \frac{A_o F_{++} J_b \bar{v}_o}{2A_s J_o P_o^{+}(1-\eta_u)} \frac{P_+^{++}+(n_o/n_+)P_o^{++}}{(eT_m/m_i)^{1/2}} \quad . \tag{B5}$$

Rearranging and multiplying by A_p/Ω_p,

$$\frac{(I^{++}/I^{+})A_p A_s}{J_b[P_+^{++}+(n_o/n_+)P_o^{++}]\Omega_p} = \frac{F_{++}\bar{v}_o}{2P_o^{+}(eT_m/m_i)^{1/2}} \frac{A_o A_p}{J_o(1-\eta_u)\Omega_p} \quad . \tag{B6}$$

The left side is the double ion parameter when single-step production of doubly charged ions is included. Note that the only difference between this parameter and the one shown in Fig. 8 is the replacement

$$(eV_d-\phi_2) \leftrightarrow [P_+^{++}+(n_o/n_+)P_o^{++}] \quad .$$

When only two-step production of doubly charged ions is considered, P_o^{++} is ignored and P_+^{++} is approximated as

$$P_+^{++} = K(eV_d-\phi_2) \quad . \tag{B7}$$

When both one-step and two-step production are included, such a simplification is not particularly advantageous. Values of P_o^{++} and P_+^{++} have been presented previously.[B2] For n_o, one can obtain from free molecular flow equations,

$$n_o = 4J_o(1-\eta_y)/eA_o\bar{v}_o \quad , \tag{B8}$$

while for n_+, using a Bohm directed velocity toward the ion extraction area of A_s, one finds

$$n_+ = F_+ J_b / (e^3 T_m / m_i)^{1/2} A_s \quad , \tag{B9}$$

where F_+ is a geometrical factor for single ions. Divising n_o by n_+,

$$\frac{n_o}{n_+} = \frac{4 A_s J_o (1-\eta_u) (e T_m / m_i)^{1/2}}{A_o J_b \bar{v}_o F_+} \quad . \tag{B10}$$

For $\bar{v}_o$ a typical discharge-chamber wall temperature of 600°K can be assumed. If T_m is known, it can be used directly. If it is not known, it can be estimated for large thrusters as $\phi_1/4$, where ϕ_1 is the first ionization potential.

For the right side of Eq. (B6), the part in brackets is the reciprocal of the neutral loss parameter. The rest of the parameters on the right side are nominally constants, but in fact do change somewhat with operating conditions.

To avoid the region of rapid variation, only data for neutral loss parameters greater than 1.5 were used to compare the correlation parameters shown in Fig. 8 and Eq. (B6). The ratio of P_+^{++} to $[P_+^{++} + (n_o/n_+) P_o^{++}]$ for previously correlated 15-cm data indicated that about 60% of the doubly charged ions were produced by a two-step process, while 40% were produced by a one-step process. The higher discharge voltages used for some of the 30-cm data would be expected to increase the significance of the one-step process, hence result in the departure from correlation indicated in Fig. 8.

Again limiting the comparison to neutral loss parameters greater than 1.5, the double ion current ratio I^{++}/I^+ was calculated using a correlation value of 1.3×10^{-3} m/(A-equiv)(eV) (2.1×10^{-3} from Fig. 8 times 0.6), then multiplying by the ratio of $[P_+^{++} + (n_o/n_+) P_o^{++}]$

divided by P_+^{++}. The correlation values obtained in this manner are compared to the experimental values in Fig. B1. The exact ratio of experimental to correlation value is, of course, dependent on the assumed 60% of double ions produced by a two-step process. What is more significant is the small $\sim\pm 20\%$ departure from mean values.

From the preceding, it is concluded that the single-step contribution should be included in an estimate of total doubly ionized production. To summarize the procedure, the mean correlation curve is reduced by 40%, then the predicted value of I^{++}/I^{+} is increased by the ratio of $[P_+^{++}+(n_o/n_+)P_o^{++}]$ divided by P_+^{++}.

If the double ion fraction is low enough to permit a long operating lifetime, then the fraction of double ions produced by a one-step process should be small. Conversely, if the fraction produced by the one-step process is large, then the thruster should be expected to have only a short lifetime. The most useful application of this procedure to thrusters should simply be to improve the understanding of double ion production for extreme operating conditions.

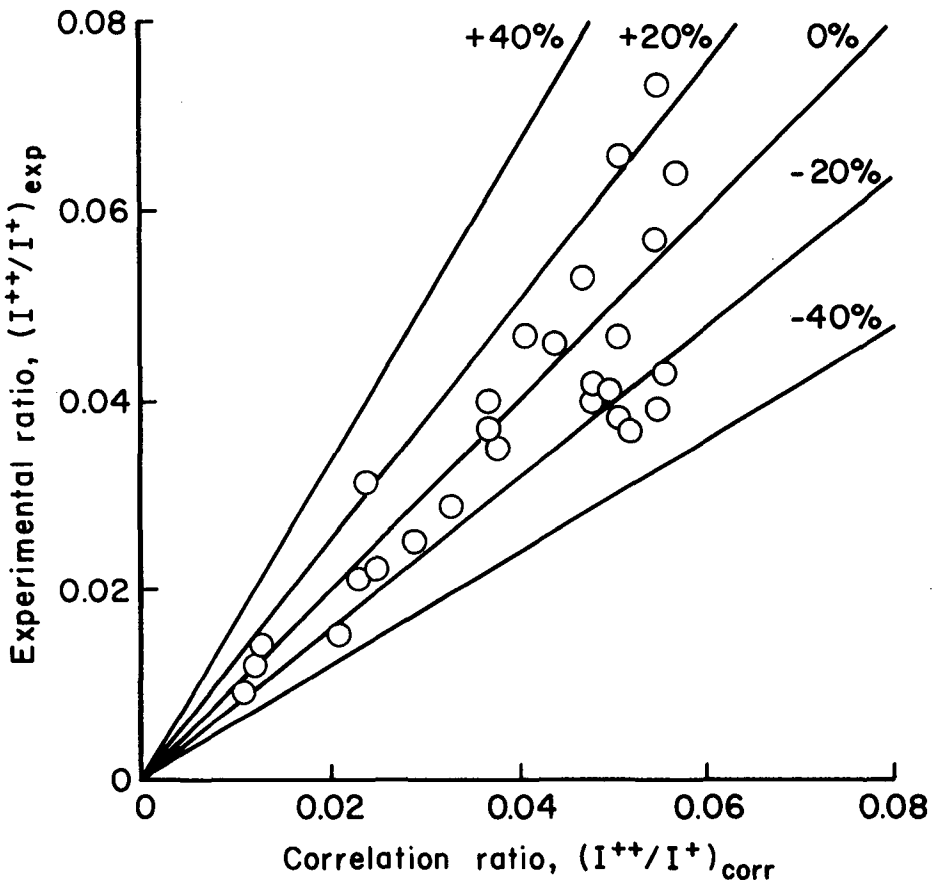

Fig. B1. Comparison of 30-cm double-ion ratios, with both one-step and two-step production of double ions from primary electrons included in the correlation predictions.

REFERENCES

B1. H. R. Kaufman and R. S. Robinson, "Inert Gas Thrusters," NASA Contr. Rep. CR-159813, Nov. 1979.

B2. H. R. Kaufman, "Inert Gas Thrusters," NASA Contr. Rep. CR-135226, July 1977.

DISTRIBUTION LIST

	Copies
National Aeronautics and Space Administration Washington, DC 20546	
Attn: RS/Mr. Dell Williams, III	1
RTS-6/Mr. Wayne Hudson	1
RTS-6/Mr. Jerome Mullin	1
MT/Mr. Ivan Bekey	1
National Aeronautics and Space Administration Lewis Research Center 21000 Brookpark Road Cleveland, OH 44135	
Attn: Research Support Procurement Section	
Mr. G. Golinski, MS 500-306	1
Technology Utilization Office, MS 3-19	1
Report Control Office, MS 5-5	1
Library, MS 60-3	2
Mr. N. Musial, MS 500-113	1
Dr. M. Goldstein, Chief Scientist, MS 5-3	1
Mr. T. Cochran, MS 501-8	1
Mr. D. Petrash, MS 501-5	1
Mr. N. Grier, MS 501-7	1
Mr. M. Mirtich, MS 501-7	1
Mr. R. Finke, MS 77-4	1
Mr. B. Banks, MS 501-7	1
Mr. D. Byers, MS 501-7	1
Mr. W. Kerslake, MS 501-7	30
National Aeronautics and Space Administration Lyndon B. Johnson Space Center Houston, TX 77058	
Attn: Mr. Hu Davis	1
National Aeronautics and Space Administration Marshall Space Flight Center Huntsville, AL 35812	
Attn: Mr. Jerry P. Hethcoate	1
Mr. John Harlow	1
Mr. John Brophy	1
Mr. Robert T. Bechtel	1
NASA Scientific and Technical Information Facility P.O. Box 8757 Baltimore, MD 21240	
Attn: Accessioning Department	1

Circuits Processing Apparatus, Inc.
725 Kifer Road
Sunnyvale, CA 94086
Attn: Spencer R. Wilder 1

Commonwealth Scientific Corporation
500 Pendleton Street
Alexandria, VA 22314
Attn: George R. Thompson 1

Computing Center of the USSR Academy of Sciences
Vavilova 40
117333 Moscow, B-333
USSR
Attn: Dr. V. V. Zhurin 1

Comsat Corporation
950 L'Enfant Plaza, S.W.
Washington, DC 20024
Attn: Mr. Sidney O. Metzger 1

COMSAT Laboratories
P.O. Box 115
Clarksburg, MD 20734
Attn: Mr. B. Free 1
Mr. O. Revesz 1

CVC Products
525 Lee Road
P.O. Box 1886
Rochester, NY 14603
Attn: Mr. Georg F. Garfield, Jr. 1

DFVLR - Institut fur Plasmadynamik
Technische Universitat Stuttgart
7 Stuttgart-Vaihingen
Allmandstr 124
WEST GERMANY
Attn: Dr. G. Krulle 1

DFVLR - Institut fur Plasmadynamik
33 Braunschweig
Bienroder Weg 53
WEST GERMANY
Attn: Mr. H. Bessling 1

EG & G Idaho
P.O. Box 1625
Idaho Falls, ID 83401
Attn: Dr. G. R. Longhurst, TSA-104 1

National Aeronautics and Space Administration
Goddard Space Flight Center
Greenbelt, MD 20771
Attn: Mr. W. Isley, Code 734 1
Mr. A. A. Vetman 1
Dr. David H. Suddeth 1

National Aeronautics and Space Administration
Ames Research Center
Moffett Field, CA 94035
Attn: Technical Library 1

National Aeronautics and Space Administration
Langley Research Center
Langley Field Station
Hampton, VA 23365
Attn: Technical Library 1
Mr. B. Z. Henry 1

The Aerospace Corporation
P.O. Box 95085
Los Angeles, CA 90045
Attn: Dr. B. A. Haatunion 1
Mr. A. H. Silva 1

The Aerospace Corporation
Space Sciences Laboratory
P.O. Box 92957
Los Angeles, CA 90009
Attn: Dr. Y. T. Chiu 1

Bell Laboratories
600 Mountain Avenue
Murray Hill, NJ 07974
Attn: Dr. Edward G. Spencer 1
Dr. Paul H. Schmidt 1

Boeing Aerospace Company
P.O. Box 3999
Seattle, WA 98124
Attn: Mr. Donald Grim, MS 8K31 1
Mr. Russell Dod 1

Case Western Reserve University
10900 Euclid Avenue
Cleveland, OH 44106
Attn: Dr. Eli Reshotko 1

C.E.N.-F.A.R.
Service Du Confinement Des Plasmas
BP6
92260 Fontenay-Aux-Roses,
FRANCE
Attn: J. F. Bonnal 1

Electro-Optical Systems, Inc.
300 North Halstead
Pasadena, CA 91107
Attn: Dr. R. Worlock 1
Mr. E. James 1
Mr. W. Ramsey 1

Electrotechnical Laboratory
1-1-4, Umezono, Sakura-Mura,
Niihari-Gun
Ibaraki,
JAPAN
Attn: Dr. Katsuya Nakayama 1

Fairchild Republic Company
Farmingdale, NY 11735
Attn: Dr. Domenic J. Palumbo 1

Ford Aerospace Corporation
3939 Fabian Way
Palo Alto, CA 94303
Attn: Mr. Robert C. Kelsa 1

General Dynamics
Kearney Mesa Plant
P.O. Box 1128
San Diego, CA 92112
Attn: Dr. Ketchum 1

Giessen University
1st Institute of Physics
Giessen,
WEST GERMANY
Attn: Professor H. W. Loeb 1

Hughes Aircraft Company
Space and Communication Group
P.O. Box 92919
Los Angeles, CA 90009
Attn: Dr. M. E. Ellison 1
Dr. B. G. Herron 1

Hughes Research Laboratories
3011 Malibu Canyon Road
Malibu, CA 90265
Attn: Mr. J. H. Molitor 1
Dr. R. L. Poeschel 1
Dr. Jay Hyman 1
Mr. R. Vahrenkamp 1
Dr. J. R. Beattie 1
Dr. W. S. Williamson 1

IBM Corporation
Thomas J. Watson Research Center
P.O. Box 218
Yorktown Heights, NY 10598
Attn: Dr. Jerome J. Cuomo 1
Dr. James M. E. Harper 1

IBM East Fishkill
D/42K, Bldg. 300-40F
Hopewell Junction, NY 12533
Attn: Mr. James Winnard 1

Ion Beam Equipment, Inc.
P.O. Box O
Norwood, NJ 07648
Attn: Dr. W. Laznovsky 1

Ion Tech, Inc.
P.O. Box 1388
1807 E. Mulberry
Fort Collins, CO 80522
Attn: Dr. Gerald C. Isaacson 1

Jet Propulsion Laboratory
4800 Oak Grove Drive
Pasadena, CA 91102
Attn: Dr. Kenneth Atkins 1
Technical Library 1
Mr. Eugene Pawlik 1
Mr. James Graf 1
Mr. Dennis Fitzgerald 1
Dr. Graeme Aston 1

Joint Institute for Laboratory Astrophysics
University of Colorado
Boulder, CO 80302
Attn: Dr. Gordon H. Dunn 1

Kirtland Air Force Base
Office of Assistant for Study Support
Albuquerque, NM 87117
Attn: Dr. Berhart Eber OAS Ge 1

Kyoto University
The Takagi Research Laboratory
Department of Electronics
Yoshidahonmachi Sakyo-ku
Kyoto 606,
JAPAN
Attn: Dr. Toshinori Takagi 1

Lawrence Livermore Laboratory
Mail Code L-437
P.O. Box 808
Livermore, CA 94550
Attn: Dr. Paul Drake 1

Lockheed Missiles and Space Company
Sunnyvale, CA 94088
Attn: Dr. William L. Owens
Propulsion Systems, Dept. 62-13 1
Mr. Carl Rudey 1

Marshall Spaceflight Center
Huntsville, AL 35812
Attn: M. Ralph Carruth, Jr., MS EC35 1

Massachusetts Institute of Technology
Room 13-3061
77 Massachusetts Avenue
Cambridge, MA 02139
Attn: Henry I. Smith 1

New Mexico State University
Department of Electrical and Computer Engr.
Las Cruces, NM 88003
Attn: Dr. Robert McNeil 1

Optic Electronics Corporation
11477 Pagemill Road
Dallas, TX 75243
Attn: Bill Hermann, Jr. 1

Physicon Corporation
221 Mt. Auburn Street
Cambridge, MA 02138
Attn: H. von Zweck 1

Princeton University
Princeton, NJ 08540
Attn: Mr. W. F. Von Jaskowsky 1
Dean R. G. Jahn 1
Dr. K. E. Clark 1

Research and Technology Division
Wright-Patterson AFB, OH 45433
Attn: (ADTN) Mr. Everett Bailey 1

Rocket Propulsion Laboratory
Edwards AFB, CA 93523
Attn: LKDA/Mr. Tom Waddell 1
LKDH/Dr. Robert Vondra 1

Royal Aircraft Establishment
Space Department
Farnborough, Hants
ENGLAND
Attn: Dr. D. G. Fearn 1

Sandia Laboratories
Mail Code 5743
Albuquerque, NM 87115
Attn: Mr. Ralph R. Peters 1

Tektronix, 50-324
P.O. Box 500
Beaverton, OR 97077
Attn: Curtis M. Haynes 1

Texas Instruments, Inc.
MS/34
P.O. 225012
Dallas, TX 75265
Attn: Larry Rehn 1

TRW Inc.
TRW Systems
One Space Park
Redondo Beach, CA 90278
Attn: Dr. M. Huberman 1
Mr. H. Ogawa 1
Mr. Sid Zafran 1

United Kingdom Atomic Energy Authority
Culham Laboratory
Abingdon, Berkshire
ENGLAND
Attn: Dr. P. J. Harbour 1
Dr. M. F. A. Harrison 1
Dr. T. S. Green 1

University of Tokyo
Department of Aeronautics
Faculty of Engineering
7-3-1, Hongo, Bunkyo-ku
Tokyo,
JAPAN
Attn: Prof. Itsuro Kimura 1

Veeco Instruments, Inc.
Terminal Drive
Plainview, NY 11803
Attn: Norman Williams 1